MACHINE LEARNING AND HIGH SPATIAL RESOLUTION MULTI-TEMPORAL SENTINEL-2 IMAGERY FOR CROP TYPE CLASSIFICATION

By
MMAMOKOMA GRACE MAPONYA

Thesis presented in partial fulfilment of the requirements for the degree of Master of Science in the Faculty of Science at Stellenbosch University

Supervisor: Prof A van Niekerk

Co-supervisor: Dr ZE Mashimbye

December 2019

DECLARATION

By submitting this thesis electronically, I declare that the entirety of the work contained therein is my own, original work, that I am the sole author thereof (save to the extent explicitly otherwise stated), that reproduction and publication thereof by Stellenbosch University will not infringe any third party rights and that I have not previously in its entirety or in part submitted it for obtaining any qualification.

With regard to Chapters 3 and 4, the nature and scope of my contribution were as follows:

Chapter	Nature of contribution	
Chapter 3	This chapter has been submitted for publication as a journal article in *Computers and Electronics in Agriculture*. It was co-authored by my supervisors who helped in the conceptualization and writing of the manuscript. I carried out the literature review, data collection, and analysis components.	MG Maponya 80% A van Niekerk 10% ZE Mashimbye 10%
Chapter 4	This chapter is being prepared for submission as a journal article and was co-authored by my supervisor who helped in the conceptualization and writing of the manuscript. I carried out the literature review, data collection, and analysis components.	MG Maponya 80% A van Niekerk 10% ZE Mashimbye 10%

Date: December 2019

Signature:

SUMMARY

Spatially-explicit crop type information is useful for estimating agricultural production areas. Such information is used for various monitoring and decision-making applications, including crop insurance, food supply-demand logistics, commodity market forecasting and environmental modelling. Traditional methods, such as ground surveys and agricultural censuses, involve high production costs and are often labour intensive, which limit their use for timely and accurate crop type data production. Remote sensing, however, offers a dependable, cost-effective and timely way of mapping crop types. Although remote sensing approaches – particularly using multi-temporal techniques – have been successfully employed for producing crop type information, this information is mostly available post-harvest. Thus, researchers and decision-makers have to wait several months after harvest to have such information, which is usually too late for many applications.

The availability and accessibility of imagery collected with optical sensors make such data preferable for mapping crop types. However, these sensors are subject to cloud-interference, which has been recognised as a source of error in the retrieval of surface parameters. It is therefore important to assess the strengths and weaknesses of using multi-temporal optical imagery for differentiating crop types. This study utilises Sentinel-2A and 2B imagery to perform several experiments in selected parts of the Western Cape, South Africa, to undertake this assessment.

The first three experiments assessed the significance of image selection on the accuracies of crop type classification. A recommended number of Sentinel-2 images was selected, using two different methods. The first of the three experiments was conducted with uni-temporal images. Based on the performance rankings of the uni-temporal images, five images with the highest ranks were used to set up Experiment 2. The third experiment was undertaken with a handpicked set of five images, based on crop developmental stages. The two image selection methods were compared to each other and subsequently to the entire time-series, to determine the significance of selecting images for crop type mapping. These classifications were undertaken with several supervised machine learning classifiers and one parametric classifier. Results showed no significant difference in classification accuracies between the two image selection methods and the entire time-series. Overall, the support vector machine (SVM) and random forest (RF) algorithms outperformed all the other classifiers.

The fourth experiment was undertaken by chronologically adding images to the classifiers. The progression of classification accuracies against time and the increase in the number of images were analysed to determine the earliest period (pre-harvest) when crops can be classified with sufficient

accuracies. The highest pre-harvest accuracy achieved was then compared to that obtained at the end of the season, including images acquired post-harvest, to assess the effectiveness of machine learning classifiers for classifying crop types when only pre-harvest images are used. The results of this experiment showed that machine learning classifiers can classify crops when only pre-harvest images are used, with accuracies similar to those obtained when the entire time-series is used. Satisfactory classification accuracies were attainable as early as Aug/Sept (eight weeks before harvest).

The fifth to tenth experiments were undertaken to assess the impact of cloud cover and image compositing on crop type classification accuracies. The fifth and sixth experiments were performed with non-composited images. Experiment Five (5) was undertaken with cloud-free images only, while the sixth experiment involved using all available images, including cloud-contaminated observations. The seventh to tenth experiments were undertaken with monthly image composites computed using four different image compositing approaches. All these experiments were undertaken using several machine learning classifiers. The results showed that machine learning classifiers performed best when all images – including cloud-contaminated images – are used as input to the classifiers. Image compositing had a detrimental effect on classification accuracies.

Generally, multi-temporal Sentinel-2 data hold great potential for operational crop type map production early in the season. However, more work is needed to develop simple workflows for eliminating cloud cover, particularly for crop type mapping in areas characterised by frequent overcast conditions.

KEYWORDS

Crop type classification, remote sensing, machine learning, pre-harvest, image selection, image compositing, operational, Sentinel-2.

OPSOMMING

Ruimtelik-eksplisiete gewastipe-inligting is nuttig vir die beraming van areas vir landbouproduksie. Hierdie inligting word gebruik vir verskeie moniterings- en besluitnemingstoepassings, insluitend gewasversekering, logistieke aangaande voedsel-vraag-en-aanbod, die voorspelling van kommoditeitsmarkte en omgewingsmodellering. Tradisionele metodes soos grondopnames en landbousensusse betrek hoë produksiekostes en is dikwels arbeidsintensief, wat hul gebruik vir tydige en akkurate dataproduksie per gewastipe beperk. Afstandswaarneming, daarteenoor, bied ’n betroubare, koste-effektiewe en tydige manier om gewastipes te karteer. Hoewel afstandswaarnemingsbenaderings – veral deur middel van multitemporale tegnieke – al suksesvol ingespan is om gewastipe-inligting te produseer, is hierdie inligting meestal na die oes eers beskikbaar. Navorsers en besluitnemers moet dus tot etlike maande ná die oes wag om hierdie inligting te ontvang, wat gewoonlik te laat is vir baie toepassings.

Die beskikbaarheid en toeganklikheid van beeldmateriaal wat deur middel van optiese sensors ingesamel is, maak hierdie data verkieslik vir die kartering van gewastipes. Hierdie sensors is egter onderhewig aan wolkinterferensie, wat erken is as ’n foutbron by die verkryging van oppervlakparameters. Dit is daarom belangrik om te assesseer wat die kragte en remminge is van die gebruik van multitemporale optiese beelde vir die differensiëring van gewastipes. Hierdie studie gebruik Sentinel-2A- en 2B-beelde om verskeie eksperimente uit te voer in gekose dele van die Wes-Kaap, Suid-Afrika, om hierdie assessering te onderneem.

Die eerste drie eksperimente het die belangrikheid van beeldseleksie vir die akkuraathede van gewastipe-klassifikasie geassesseer. ’n Aanbevole aantal Sentinel-2-beelde is gekies deur twee verskillende metodes te gebruik. Die eerste van die drie eksperimente is uitgevoer met unitemporale beelde. Op grond van die prestasiegraderings van die unitemporale beelde is vyf beelde met die hoogste graderings gebruik om Eksperiment 2 op te stel. Die derde eksperiment is gedoen met ’n uitgesoekte stel van vyf beelde, gebaseer op stadiums van gewasontwikkeling. Die twee beeldseleksiemetodes is met mekaar vergelyk en gevolglik met die hele tydreeks, om te bepaal wat die betekenis daarvan is om beelde te kies vir gewastipe-kartering. Hierdie klassifikasies is onderneem met verskeie masjienlerende klassifiseerders en een parametriese klassifiseerder, onder toesig. Resultate het geen beduidende verskil in klassifikasie-akkuraathede gewys tussen die twee beeldseleksiemetodes en die algehele tydreeks nie. In die geheel het die steunvektormasjien- (SVM) en lukrake-woud- (“random forest”, RF) -algoritmes beter presteer as al die ander klassifiseerders.

Die vierde eksperiment is onderneem deur beelde chronologies by die klassifiseerders te voeg. Die progressie van klassifikasie-akkuraathede teenoor tyd en die toename in die aantal beelde is geanaliseer om die vroegste periode (voor-oes) te bepaal wanneer gewasse met voldoende akkuraathede geklassifiseer kan word. Die hoogste voor-oes-akkuraatheid is toe vergelyk met dit wat teen die end van die seisoen behaal is, insluitend beelde wat na-oes ingesamel is, om die doeltreffendheid van masjienlerende klassifiseerders te bepaal by die klassifisering van gewastipes wanneer slegs voor-oes-beelde gebruik is. Die resultate van hierdie eksperiment het gewys dat masjienlerende klassifiseerders gewasse kan klassifiseer wanneer slegs voor-oes-beelde gebruik is, met akkuraathede wat soortgelyk is aan dit wat behaal is wanneer die hele tydreeks gebruik is. Bevredigende klassifikasie-akkuraathede is so vroeg as Aug/Sep behaal (agt weke voor oes).

Die vyfde tot tiende eksperimente is onderneem om die impak van wolkbedekking en beeldsamestelling op klassifikasie-akkuraathede van gewastipes te bepaal. Die vyfde en sesde eksperimente is met nie-saamgestelde beelde uitgevoer. Eksperiment Vyf (5) is slegs met wolkvrye beelde gedoen, terwyl die sesde eksperiment die gebruik van alle beskikbare beelde, insluitend wolkgekontamineerde observasies, betrek het. Die sewende tot tiende eksperimente is onderneem met maandelikse beeldsamestellings wat bereken is deur middel van die gebruik van vier verskillende benaderings tot beeldsamestelling. Al hierdie eksperimente is met behulp van verskeie masjienlerende klassifiseerders uitgevoer. Die resultate het gewys dat masjienlerende klassifiseerders die beste presteer het wanneer alle beelde – insluitend wolkgekontamineerde beelde – as invoer aan die klassifiseerders gebruik word. Beeldsamestelling het ’n nadelige uitwerking op klassifikasie-akkuraathede gehad.

Oor die algemeen het multitemporale Sentinel-2-data vroeg in die seisoen goeie potensiaal vir operasionele gewastipe-kaartproduksie. Meer werk is nietemin nodig om eenvoudige werkvloei te ontwikkel om wolkbedekking te elimineer, veral vir gewastipe-kartering in areas wat gereeld gekenmerk word deur oortrokke toestande.

TREFWOORDE

Gewastipe-klassifikasie, afstandswaarneming, masjienlerende, voor-oes, beeldseleksie, beeldsamestelling, operasionele, Sentinel-2.

ACKNOWLEDGEMENTS

I sincerely thank:

- The Father in heaven for the constant supply of strength and motivation despite all odds throughout the period of this research;
- My late parents Mrs Sinah and Mr Theophilus Maponya, for planting the seed of persistence and resilience in me, for the love and nurture until their time of death. I would not have done it without the principles they raised me with;
- My supervisors, Prof Adriaan van Niekerk and Dr Eric Mashimbye, for their continued support, advice, patience and understanding;
- Divan, Christian and the CGA for their advice and support throughout the study;
- The Agricultural Research Council for funding this research;
- The Water Research Commission (WRC) for funding the project titled "Wide-scale modelling of water and water availability with Earth observation/satellite imagery" (contract number K5/2401//4) of which this work forms part. More information about this project is at www.wrc.org.za in WRC Report TT 745 (ISBN: 978-1-4312-0964-4).
- www.linguafix.net (Helene van Niekerk) for the language checking and editing services provided;
- My siblings for being the best anyone can ask for;
- My friends, Ms Thendo Netshidzivhe, Dr Faith Mupfumira, Mrs Elsie Musango, Ms Rudzani Thangambi and Ms Perpetua Okoye for their love, support, prayers and being there always;
- My fellow students in the Department of Geography and Environmental Studies, for the chats and words of encouragement;
- The RFM family, particularly my pastor (Pastor Russel Mupfumira), for providing me with spiritual nourishment, prayers and their constant love and support through the varying seasons of life and
- Everyone who played a role in making this work a success, although I might have not mentioned their names.

CONTENTS

TABLES

FIGURES

APPENDICES

ACRONYMS AND ABBREVIATIONS

ASTER	Advanced spaceborne thermal emission and reflection radiometer
AVHRR	Advanced very high-resolution radiometer
AFRI	Aerosol free vegetation index
ARVI	Atmospherically resistant vegetation index
ANN	Artificial neural networks
BRDF	Bidirectional reflectance distribution function
CGA	Centre for Geographical Analysis
DT	Decision trees
DAFF	Department of Agriculture, Forestry and Fisheries
ERTS MSS	Earth resources technology satellite multispectral scanner
EM	Electromagnetic
EVI	Enhanced vegetation index
ESA	European Space Agency
GIS	Geographical information systems
GDAL	Geospatial data abstraction library
GLCM	Grey-level co-occurrence matrix
GNDVI	Green normalised difference vegetation index
GVI	Green vegetation index
GDP	Gross domestic product
IPVI	Infrared percentage vegetation index
IFOV	Instantaneous field of view
Ks	Kappa coefficients
K-NN	k-Nearest neighbour
MAT	Maximum apparent temperature
ML	Maximum likelihood

MaxRatio	Maximum ratio
MVC	Maximum value composite
MaxNDVI	Maximum value normalised difference vegetation index
MC	Mean compositing
MC-FUME	Median composite of fuzzy multispectral estimate
MSA	Minimum scan angle
MinRed	Minimum red value
MODIS	Moderate-resolution imaging spectroradiometer
MEDOID	Multidimensional analogue of the median
MSI	Multispectral instrument
NIR	Near-infrared
NN	Nearest neighbour
NDMI	Normalised difference moisture index
NDVI	Normalised difference vegetation index
NDWI	Normalised difference water index
OA	Overall accuracy
PCA	Principal component analysis
PVI	Perpendicular vegetation index
QLFS	Quarterly labour force survey
RADAR	Radio detection and ranging
RF	Random forest
RVI	Ratio vegetation index
SPOT	Satellite Pour l'Observation de la Terre
SWIR	Shortwave infrared
SAVI	Soil-adjusted vegetation index
SLICE	Supervised learning and image classification environment
SVM	Support vector machine

TOC	Top-of-canopy
TIR	Thermal infrared
VI	Vegetation index
VZA	View zenith angle
VIS	Visible region
WELD	Web-enabled Landsat data

CHAPTER 1: MULTI-TEMPORAL REMOTE SENSING OF CROP TYPES

1.1 INTRODUCTION

The agricultural industry plays a dominant role in the economies of many developing countries. According to the Department of Agriculture, Forestry and Fisheries (DAFF 2018), the South African agricultural industry provides more jobs per Rand than any other productive industry in the country. It accounts for about 3% of the gross domestic product and is responsible for ensuring food security. The role of agriculture in the South African economy and the need for sustainable management of natural resources call for the development of operational mapping and monitoring of agricultural areas (Matton et al. 2015). Crop type maps in particular provide baseline information for the effective management and monitoring of agricultural production and resources. These crop type maps are also used for agro-environmental measurements, as well as for monitoring crop water use (Peña-Barragán et al. 2011). The accurate and timely classification of crop types is, therefore, of axiomatic importance for agricultural management and monitoring (Branca et al. 2011).

Traditional methods for updating crop type maps include qualitative interviews with farmers or in situ visits to selected fields (Peña-Barragán et al. 2008). These traditional methods are laborious, time-consuming and often limited to a few accessible fields (Gilbertson, Kemp & Van Niekerk 2017). Remote sensing techniques have been used for mapping crop types, but as yet there is no publicly available method for producing spatially-explicit, within-season crop type maps at regional scales (Castillejo-González et al. 2009; Hao et al. 2015; Sun et al. 2016). Researchers and decision-makers often have to wait for four to six months after harvest to gain access to crop type data of a particular season. Crop type classification techniques have, however, advanced from the conventional remote sensing methods, which relied only on spectral features and low spatial and high temporal resolution imagery, to a combination of spectral, spatial and textural information derived from high spatial and temporal resolution multi-temporal imagery (Peña-Barragán et al. 2011).

1.1.1 Multispectral imagery for crop type mapping

Several studies have been undertaken for mapping crop types using different types of remotely sensed imagery. This data includes hyperspectral, multispectral and synthetic aperture radar (Sun et al. 2016). Each of the aforementioned data types has distinguishing characteristics and specific limitations and advantages. For most multi-temporal crop type mapping applications, the choice of image data is governed by the availability of imagery for the chosen site, the environmental

conditions at the site, the temporal characteristics of crops and the cost of imagery (Balasubramanian 2017). Multispectral imagery has been found to be affordable and readily available and as such, have frequently been used for crop type mapping (Castillejo-González et al. 2009; Löw & Duveiller 2014; Hao et al. 2015). Commonly used multispectral instruments in agricultural applications include the moderate-resolution imaging spectroradiometer (MODIS), the advanced very high-resolution radiometer (AVHRR) and Landsat 1-8 (Flood 2013; Kussul et al. 2017; Shelestov et al. 2017).

The European Space Agency (ESA) recently embarked on the Sentinel-2 mission through which high spatial and temporal resolution imagery is easily accessible and freely available. Sentinel-2 is a European earth polar satellite constellation based on the concurrent operation of two identical satellites orbiting in a single plane (Pahlevan et al. 2017). Each of the twin satellites hosts a multispectral instrument (MSI), covering a spectral range from visible to near- and shortwave infrared. The MSI measures reflected radiance in thirteen (13) spectral bands, including: blue, green, red and near-infrared (measured at 10 m spatial resolution); four (4) 20 m resolution vegetation red-edge bands for vegetation characterisation; two (2) wider shortwave infrared (SWIR) for vegetation moisture stress assessment and 60 m resolution coastal aerosol, shortwave infrared (cirrus) and water vapour bands, mainly for cloud screening and atmospheric corrections (Galoppo, Castellani & Carriero 2018). The 13 bands, their respective wavelengths and spatial resolutions are illustrated in Figure 1.1

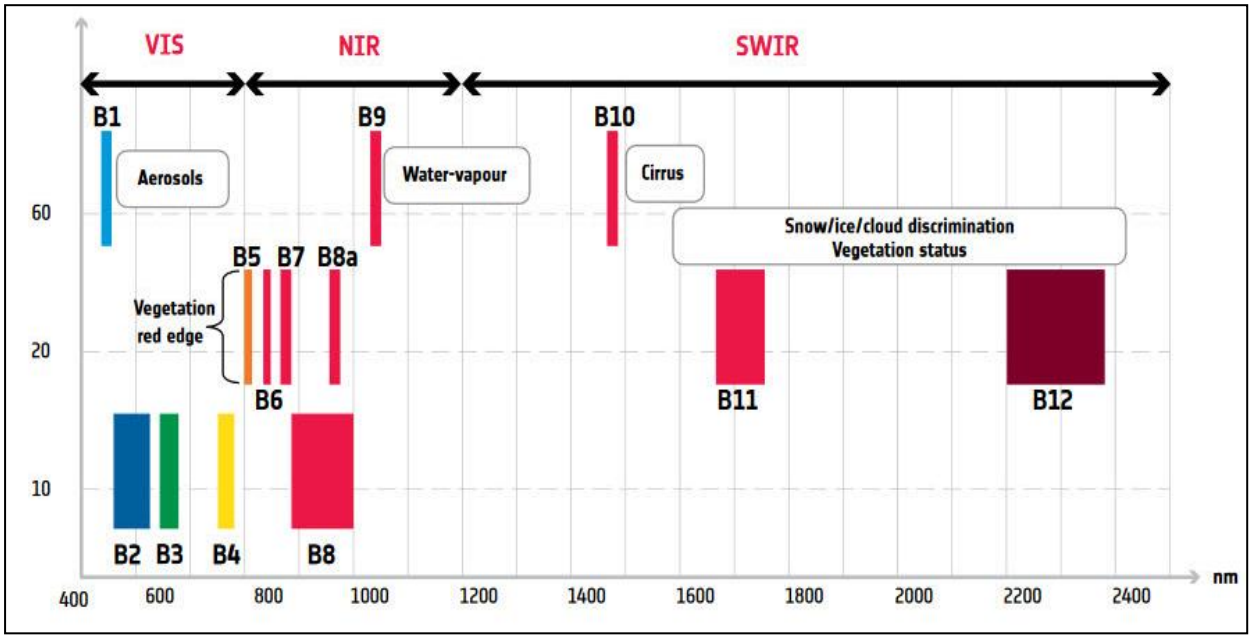

Adapted from Gatti et al. (2018)

Figure 1.1 Sentinel-2 bands grouped according to their intended use, respective spatial resolutions and wavelength regions

Several studies have shown the importance of phenological features, derived from optical sensors, for crop type identification (Nigam et al. 2015; Zhang et al. 2017). The red-edge and SWIR bands provided by satellites such as RapidEye (Eitel et al. 2007) have proven to be particularly useful (Sonobe et al. 2017). The four vegetation red-edge bands (Band 5 – vegetation red-edge, Band 6 – vegetation red-edge, Band 7 – vegetation red-edge and Band 8a – narrow near-infrared) and two SWIR bands (Band 11 – SWIR and Band 12 – SWIR) with which Sentinel-2 imagery is collected, were specifically designed for the differentiation of vegetation (including crops) types and conditions and have been shown to be beneficial in applications such as urban green species mapping (Rosina & Kopecká 2016), for separating burned and unburned areas (Roteta et al. 2019) and for cropland mapping (Belgiu & Csillik 2018). These authors attributed the success of Sentinel-2 imagery to the sensitivity of the infrared, shortwave infrared, and red-edge bands to vegetation and soil moisture changes. The unprecedented combination of high spatial and temporal resolution and spectral range in a single satellite programme is considered a major step forward, compared to previous multispectral missions (Drusch et al. 2012).

1.1.2 Image classification

Since the emergence of remote sensing, different approaches involving supervised and unsupervised image classification methods have been developed (Nitze, Schulthess & Asche 2012). Literature indicates that supervised classification methods are most commonly used for crop type mapping (Kussul et al. 2017; Ma et al. 2017; Massey et al. 2017; Sonobe et al. 2017 Palchowdhuri et al. 2018). While many supervised classification methods have been developed and applied, Gilbertson, Kemp & Van Niekerk (2017) found non-parametric machine learning algorithms' ability to use known data for classifying large sets of imagery – while incorporating ancillary spatial data – to be advantageous for crop type classification. Widely used machine learning algorithms include support vector machine (SVM), decision trees (DTs), k-nearest neighbour (k-NN) and random forest (RF).

Recent studies (Zheng et al. 2015; Gilbertson, Kemp & Van Niekerk 2017; Cai et al. 2018; Teluguntla et al. 2018) highlighted the superiority of non-parametric machine learning algorithms over parametric classifiers such as maximum likelihood (ML). SVM's ability to handle high input variable dimensionality and to generalise well, even with few training samples, affords it an advantage for crop type identification over many other classifiers (Myburgh & Van Niekerk 2013; Peña et al. 2014; Ozdarici-Ok, Ok & Schindler 2015). RF's ability to perform well even with highly homogeneous, high-dimensional and redundant data, has led to its use in many agricultural mapping applications (Long et al. 2013). DTs, k-NN and ML have also been used successfully for land cover classification and vegetation studies (Myint et al. 2011).

Several studies have compared supervised classifiers for crop type mapping. For example, Peña et al. (2014) made a comparison between C4.5 decision tree, logistic regression, multilayer perception and SVM to classify nine crops with advanced spaceborne thermal emission and reflection radiometer (ASTER) imagery and reported SVM to outperform the other classifiers. Ozdarici-Ok, Ok & Schindler (2015) compared SVM, RF, ML and the Gaussian mixture model to classify six crops, using single-date multispectral imagery collected with three different sensors, and found SVM to be superior.

1.1.3 Image selection

Since multispectral imagery is affected by cloud cover, crop type mapping can be negatively affected by cloud-contamination even at a five-day revisit frequency (Inglada et al. 2016). One way of dealing with this limitation of multispectral imagery is to identify cloud-free images covering key periods in the crop growing cycle (Hao et al. 2015). Several authors found key periods, such as the initial green-up and late senescence phases, to be important for accurate crop classification (Brown et al. 2013; Hao et al. 2015). Hao et al. (2015) compared eight time-series lengths, ranging from one month to eight months, to determine the impact of time-series length on crop classification accuracies. They found that adding features beyond five months had no significant impact on classification accuracies. Peña-Barragán et al. (2011) selected three dates based on the pre-study of crop calendars to identify key growth stages (mid-spring, early-summer and late-summer), which were used to classify 13 summer crops. An overall accuracy of 79% was reported. Gilbertson, Kemp & Van Niekerk (2017) selected five images based on a crop calendar to classify seven crops and reported accuracies as high as 95%.

1.1.4 Image compositing

Despite the successes of image selection, Inglada et al. (2015) highlighted the need for using all available images for operational crop type mapping. They argued that, although the success of hand-selecting images is undeniable, it is not always feasible, especially in fully-automated workflows. Image compositing has been proposed as an alternative to image selection. The objective of compositing remotely sensed images is primarily to minimise contamination of the pure top-of-canopy signal (such as clouds and cloud shadow), as well as to reduce data volumes (White et al. 2014; Roberts, Mueller & Mcintyre 2017). Image compositing is achieved by aggregating image observations and replacing poor and cloud-contaminated data with good observations from imagery acquired within the stipulated compositing period (Lück & Van Niekerk 2016).

From the vast range of image compositing approaches developed, Vancutsem et al. (2007) compared the mean compositing (MC) approach with the maximum value normalised difference vegetation index (MaxNDVI) image compositing technique. They found the MC technique to retain more spatial consistency than the contending technique. The MC technique, initially proposed by Meyer, Verstraete & Pinty (1995), averages all reflectance values acquired during the compositing period. Conversely, Flood (2013) compared multidimensional median (MEDOID) and MaxNDVI's abilities to produce seasonal composites and found the resulting composites of MEDOID to be more representative of the time-series than those produced with the MaxNDVI. The MEDOID approach was reported to be advantageous for cloud reduction because of its robustness against extreme values. Consequently, the resulting composites are more representative of the time-series (Flood 2013). Another widely employed compositing approach is the minimum red value (MinRed), proposed by D'Iorio (1991) and used by De Wasseige, Vancutsem & Defourny (2000) and Cabral et al. (2003). Luo, Trishchenko & Khlopenkov (2008) compared this approach to the MaxNDVI and MaxRatio approaches and reported that, although the MinRed was successful in eliminating clouds, it tends to retain shadow-contaminated pixels in the final composite. With the growing interest in operational crop type data production, it is necessary to identify simple image compositing approaches that are fully automatic and effective for crop type classification.

1.2 PROBLEM STATEMENT

Timely and accurate crop type maps are critical for crop production forecasts, which informs decisions about food security (e.g. commodity trading and imports planning). The value of crop type maps depends on how early in the growing season they can be produced. For its value to be enhanced, crop type data needs to be available as early as possible, ideally before harvest. Most crop type mapping procedures have, however, been focussing on producing crop type maps post-harvest and users often have to wait four to six months after harvests for access to such data. With the shortening of crop rotations, multiple cropping and phenological patterns related to different crops, multi-temporal remote sensing offers a feasible and effective approach for producing pre-harvest crop type maps (Atzberger 2013).

The recent launches of two Sentinel-2 satellites provide a great opportunity for multi-temporal crop type mapping. But even with the improvements in spatial and temporal resolutions offered by this constellation, the presence of clouds remains a recognised challenge for crop type mapping **(**Ogunbadewa 2012**)**. Image selection based on critical crop developmental stages and image compositing have been proposed as the two approaches for addressing cloud-contaminated images. However, even though image selection has proven effective for crop type mapping, it is not always

viable, especially when the objective is to develop an operational crop type data production system. In such systems, the use of all available images is often more feasible. This is because the selection of appropriate images requires a pre-study of crop calendars, and crop calendars vary from region to region. Seasonal variations caused by unusual weather conditions can also reduce their usefulness for image selection. Image compositing is an attractive alternative as it can be used to filter out poor-quality data (by combining images from different dates) but most compositing techniques involve elaborate pre-processing steps. The establishment of simple and easily-automated image selection or compositing techniques suitable for crop type mapping is thus a priority.

From the preceding discussion, it should be clear that Sentinel-2 imagery offers many opportunities for automated crop type mapping, but several knowledge gaps exist. The following research questions about the use of Sentinel-2 imagery for crop type mapping were specifically selected for consideration in this study:

1) What is the influence of image (date) selection on crop classification accuracies?
2) What levels of accuracy can machine learning classifiers achieve when only pre-harvest images are used as input for crop type classification?
3) To what extent does image compositing affect crop classification accuracies?

1.3 RESEARCH AIM AND OBJECTIVES

The aim of the study was to determine the value of machine learning classifiers based on multi-temporal Sentinel-2 data for discriminating crops grown in a Mediterranean climate in the Western Cape Province of South Africa. The significance of image selection and the value of multi-temporal pre-harvest imagery based on machine learning classifiers will be determined and the impact of cloud cover and image compositing for crop type differentiation will be evaluated.

To achieve the research aim, the following objectives have been set:

1) conduct a review of literature on crop type mapping based on remote sensing techniques;
2) determine the significance of image (date) selection for crop type classification;
3) assess classifier performance when only pre-harvest images are used as input; and
4) overview the impact of cloud cover and image compositing on crop type classification.

1.4 STUDY AREAS

This study was conducted in two areas covered by Sentinel-2 tiles T34HJB and T34HEH in the Western Cape Province of South Africa. For the purpose of this study, T34HJB and T34HEH will

be referred to as Study Sites A and B respectively (Figure 1.2). Site A is located about 50 km north of Cape Town, while Site B is located east of the Langeberg Mountain range and south of the Swartberg Mountain range. Both sites have a Mediterranean climate and are as such characterised by warm, dry summers and cool, wet winters (Malan 2016). Site A has an average annual rainfall of 550 mm, with an average minimum temperature of 11°C and an average maximum temperature of 22° C (Tererai et al. 2015). Site B has an average rainfall of 800 mm, with an average minimum temperature of 7ºC and an average maximum temperature of 22ºC (Malan 2016). These sites were chosen owing to the diversity of crops cultivated and the availability of crop census data.

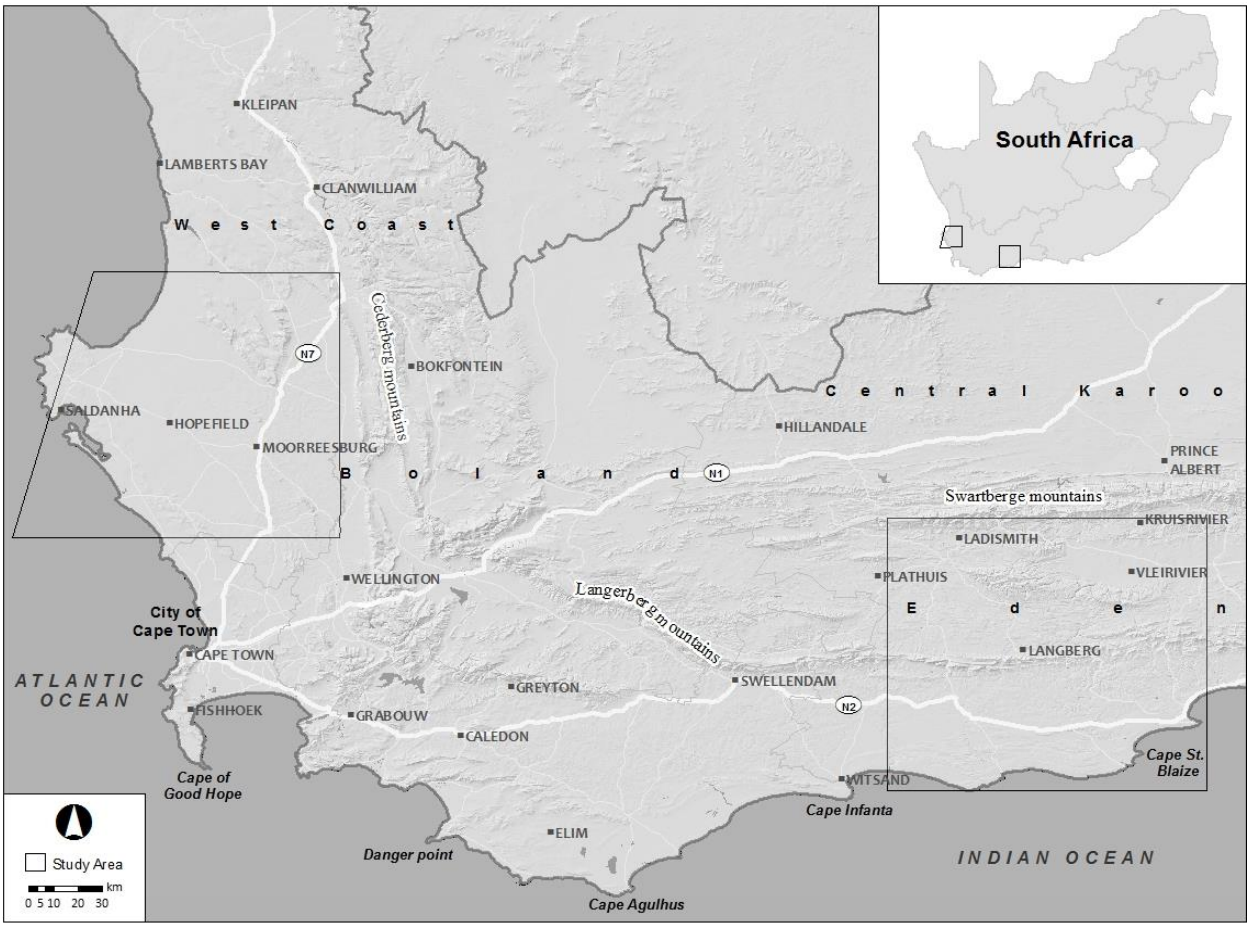

Figure 1.2 Location of the study sites in the Western Cape, South Africa

1.5 METHODOLGY AND RESEARCH AGENDA

This study is quantitative in nature. Ten experiments were undertaken, using empirically derived datasets with non-parametric classifiers to investigate the value of various techniques and methods for discriminating crops within a Mediterranean climatic region. In some cases, qualitative methods were used to aid data editing, manipulation and interpretation. The outputs of the experiments were assessed using empirical in situ data, or the visual interpretation of satellite imagery. Statistical methods were used to assess the accuracy of classifications and to determine the significance of observed differences.

The dissertation is structured into five (5) chapters. Figure 1.3 shows the research design and structure of the thesis. This chapter (Chapter 1) lays the foundation for the rest of the thesis by outlining the research problem which led to the development of the aforementioned aim and objectives. The next chapter (Chapter 2) presents the literature review and provides an overview of remote sensing approaches used for crop type classification, with specific focus on the application of multispectral (optical) remote sensing approaches. This is followed by a description of image pre-processing and interpretation approaches, which precedes an overview of multi-temporal remote sensing for crop type mapping. Chapter 3 and 4 respond to the objectives of the study and are presented as independent investigations to be submitted for publications in peer-reviewed journals. Chapter 3 investigates the significance of image selection and the value of multi-temporal pre-harvest imagery based on machine learning classifiers for crop type mapping. Objectives 2 and 3 are addressed in Chapter 3 based on Experiments 1 – 4.

The first experiment focused on uni-temporal (single image) classifications, which contributed towards answering Research Question 1. The main aim of Experiment 1 was to identify the five images (dates) within a particular growing season that produces the highest classification accuracies. The findings of this experiment were subsequently used to set up Experiment 2.

Experiments 2 and 3 focused on classifying crops, using selected images. While Experiment 2 used five images selected on the basis of the performance rankings determined in Experiment 1, the execution of Experiment 3 was based on the selection of five images representing significant developmental stages of crops (using crop calendars). Along with Experiment 1, both Experiments 2 and 3 aimed to address research Question 1. The aim of these experiments was to compare the two approaches and assess their efficacy in differentiating crops.

The fourth experiment was carried out with all available images collected during the growing season and thus addresses Research Question 2 (Objective 3). The experiment was set up by chronologically adding images collected from the beginning to the end of the season as input to the classifiers. The aim of the experiment was to assess the performance of machine learning classifiers when only images collected pre-harvest are used as input for crop differentiation, while monitoring the variations in classification accuracies as a function of time and the number of images. The design and results of these four experiments are given in Chapter 3.

Chapter 4 responds to Objective 4, which assesses the influence of image compositing and cloud cover on crop type classification accuracies by carrying out Experiments 5, 6, 7, 8, 9 and 10. The fifth experiment was undertaken with cloud-free images only, while the sixth experiment was undertaken with all available images, whether they are contaminated by clouds or not. The seventh, eighth, ninth and tenth experiments were undertaken with composited images. In combination,

these six experiments addressed Research Question 3. In both Chapter 3 and 4, a brief overview of the pertinent concepts, as well as a description of the sites within which this study was conducted, are provided. Due to the intention to submit these two chapters as articles to respective scientific journals, some figures, tables and text are duplicated. The overall findings of the study are summarised in Chapter 5. The chapter also critically reflects on the study's strengths and weaknesses and concludes with suggestions for future research.

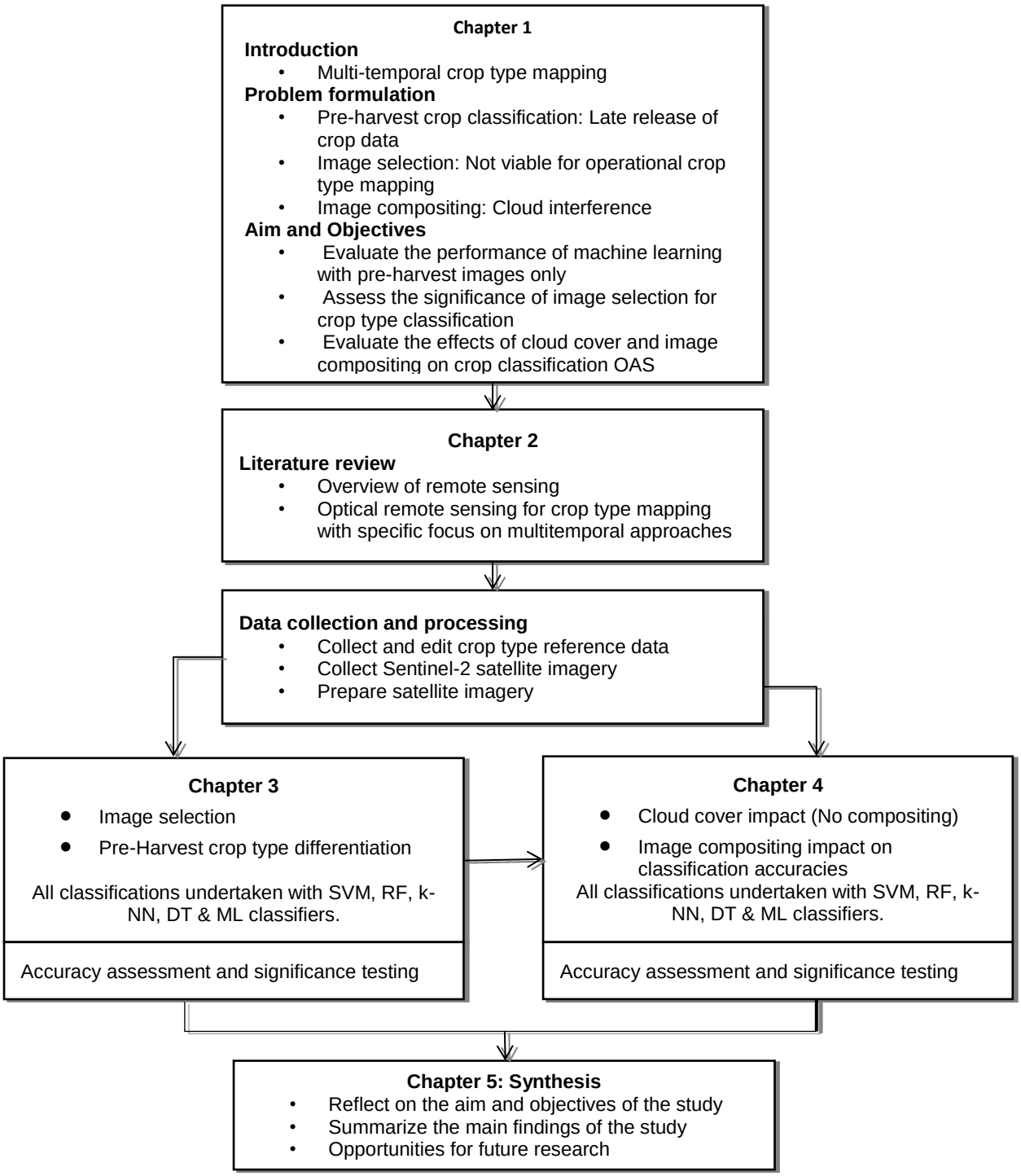

Figure 1.3 Research design for evaluating the performances of machine learning and multi-temporal Sentinel-2 imagery for crop type mapping.

CHAPTER 2: LITERATURE REVIEW

Understanding remote sensing concepts related to crop type identification is vital for achieving the set aim and objectives of this study. This chapter presents a review of literature on the remote sensing of crop types, with an overview, followed by a brief outline of optical vs microwave remote sensing. The optical remote sensing of crop types is investigated, with specific focus on multi-temporal remote sensing. The chapter concludes by providing a synthesis of the most pertinent findings of the literature review.

2.1 OVERVIEW OF REMOTE SENSING FOR CROP TYPE MAPPING

Remote sensing is the acquisition of information about objects on the earth's surface without direct contact, using aircraft and satellite sensors to record electromagnetic radiation (light) through one or more regions of the electromagnetic spectrum (ES) emitted and reflected from the earth's surface (Campbell 2007; Muller 2017). Electromagnetic (EM) energy consists of two oscillating components, which are electric and magnetic fields, and is measured by its wavelength or frequency unit (Tempfli et al. 2009). While this energy is generated by all matter with a temperature above absolute zero (Tempfli et al. 2009), the sun is the primary source of energy and produces a full spectrum of electromagnetic radiation, known as the ES. The behaviour of EM energy changes as it passes through the atmosphere to interact with objects on the earth's surface (Muller 2017). As each object on the earth's surface uniquely interacts with EM energy, the levels of reflection and absorption of each object on the earth's surface vary. Using remotely sensed data, changes in the behaviour of surface objects under different EM energy spectra can be recorded to provide an opportunity to extract knowledge on the varying characteristics of surface objects (Campbell 2007). The most relevant regions of the ES for remote sensing applications are described by Chuvieco & Huete (2010) as the visible (VIS), near-infrared (NIR), shortwave infrared (SWIR) and thermal infrared (TIR) regions, depending on the specifications of each task.

The VIS region includes the blue, green and red regions of the spectrum with wavelengths ranging from 0.4 to 0.7 micrometres (μm), and is named after the energy that can be sensed by the human eye (Neinavaz et al. 2016). The NIR region is commonly known for its sensitivity to green vegetation and includes wavelengths between 0.7 and 1.2 μm (Tempfli et al. 2009). The SWIR region is delimited by 1.2 and 3 μm wavelengths and is known for its sensitivity to vegetation and soil moisture (Neinavaz et al. 2016). Wavelengths longer than 3 μm, such as TIR, are mostly associated with emissive electromagnetic radiation from the earth's surface (Tempfli et al. 2009; Neinavaz et al. 2016). The microwave region (shortest wavelength) has properties similar to the thermal region. The longest wavelengths merge into radio wavelengths and are commonly used

for commercial broadcasts (Campbell 2007). The practicality of remote sensing depends on the ability of sensors to record energy in any of the wavelength regions of the electromagnetic spectrum where detectable differences in reflected and emitted radiation for specific objects are large enough to permit individual identification (Barrett 2013). Generally, remote sensors are classified as passive (optical) and active (microwave) sensors (De Jong & Van der Meer 2007). Common examples of optical sensors include MODIS, AVHRR LANDSAT and SPOT, while widely used microwave sensors include radio detection and ranging (RADAR) and light detection and ranging (LIDAR). The following section provides a brief overview of these two types of sensors.

2.1.1 Optical (passive) vs. microwave (active) remotely sensed data

Crop type mapping studies have been conducted using different types of remote sensors such as optical, microwave and, in some cases, a combination of optical and microwave remote sensors (Lohmann et al. 2009; Keifer 2014; Sonobe et al. 2014; Beyer, Jarmer & Siegmann 2015; Inglada et al. 2016). Optical sensors do not have their own source of radiation; they depend on radiation from natural sources such as the sun or energy emitted by earthly objects (De Jong & Van der Meer 2007). Therefore, optical sensors measure radiation that reaches a detector without the sensor first transmitting any energy (Turner et al. 2003). This dependence of optical sensors on natural energy limits their operation to daytime when there is a natural supply of energy (sun) (Gilbertson, Kemp & Van Niekerk 2017). Although data from optical sensors is affected by weather conditions, it is often cheaper and more readily available (Ozdarici-Ok, Ok & Schindler 2015; Inglada et al. 2016). Examples of optical sensors include multispectral scanners and thermal scanners. Microwave sensors, on the other hand, have a built-in source of radiation (De Jong & Van der Meer 2007). Thus, microwave sensors emit their own energy and later measure the energy returned or bounced back to a detector (Muller 2017). The independence of microwave sensors from natural energy sources enable them to operate both during the day and at night. Although these sensors are able to acquire data at any time and are less affected by weather conditions, large amounts of energy are necessary to illuminate targets and they are susceptible to speckle noise (LaDue, Heinselman & Newman 2010; Grandoni 2018; Forkuor et al. 2014; Jiao et al. 2014; Joshi et al. 2016; You, Jianjuan & Xin 2016). Consequently, optical sensors are often preferred for crop type mapping. The following section describes the different characteristics of optical remote sensing.

2.1.2 Characteristics of optical imagery

Each optical sensor is defined by a unique set of characteristics relative to its satellite system, which influences its value for specific remote sensing problems. These characteristics include

radiometric, spectral, spatial, and temporal resolution. Radiometric resolution relates to the satellite sensor's sensitivity and its ability to differentiate the variations recorded in the spectrum (Chuvieco & Huete 2010). Radiometric resolution directly relates to the number of grey levels within one band and is limited by the images' bit number (Gibson 2000). Therefore, an increase in radiometric resolution will result in a higher number of grey levels within a band (Muller 2017). Spectral resolution relates to the number (and width) of sensor bands provided. This resolution directly relates to the sensor's coverage of the electromagnetic spectrum. A larger spectral resolution results in a greater coverage of the electromagnetic spectrum, which enables a better recording of surface objects' spectral characteristics. Spatial resolution refers to detail visibility in an image. For satellites, it is primarily determined by its instantaneous field of view (IFOV) and measured by metres on the ground (Chuvieco & Huete 2010; Gibson 2000). The spatial resolution of satellite images can range from a few centimetres to kilometres, depending on the satellite system. Temporal resolution measures the frequency at which a satellite system revisits a specific area. This resolution is determined by the satellite system's orbital characteristics and its swath overlap (Chuvieco & Huete 2010).

The different resolutions described above are usually interconnected, thus an increase in one may lead to a decrease in another (Chuvieco & Huete 2010). For example, satellite sensors that capture imagery at a high spatial resolution generally have low temporal and spectral resolutions. This is due to the combined effect of factors, inclusive of the IFOV, the satellite's scan speed, the optics of the satellite, the sensor itself and download link speeds. The choice of a remote sensing data type depends on the requirements of a specific application and the budget available for the project. Both multispectral and hyperspectral sensors have been applied for crop type mapping (Bauer & Cipra 1973; Sabour, Lohmann & Soergel 2008; Liu, Ozdogan & Zhu 2013; Hao et al. 2015). While multispectral images only have a couple of spectral bands, hyperspectral images have hundreds of narrow bands in the visible, through the near-infrared to the shortwave infrared portions of the ES (Adam, Mutanga & Rugege 2010). Although hyperspectral data have been successfully applied for mapping crop types (Bannari et al. 2006; Govender, Chetty & Bulcock 2007; Pacheco & McNairn 2010), the data are not as readily available as multispectral imagery. Consequently, multispectral imagery has been extensively used for mapping crop types. A brief overview of the application of multispectral remote sensing for crop type mapping is provided in the following section.

2.1.3 Multispectral imagery

The ability to identify crop types makes it possible to estimate the area used for crop production which is necessary for computing crop statistics in turn needed to provide essential information

relevant for various applications (Shewalkar, Khobragade & Jajulwar 2014). Timely and accurate information about the spatial distribution of crops plays an important role in assessing the environmental impacts associated with the emergence of cropping practices (Shao et al. 2010). Changes in crop types, shortening of crop rotations, increased multiple cropping and strong seasonal patterns related to different crops make remote sensing a feasible and effective technology for mapping crop types (Heller et al. 2012; Atzberger 2013). Since the earliest stages of crop classification with remote sensing, various approaches based on supervised and unsupervised classification techniques have been used to map the spatial distribution of crops using data collected with optical remote sensors (Nellis, Price & Rundquist 2009).

Multispectral remote sensing data can be acquired using two main platforms, namely airplanes and satellite-based sensors (Muller 2017). Multispectral sensors have a long history of application in crop monitoring (Hoffer, Johannsen & Baumgardner 1966; Bauer & Cipra 1973; Wardlow, Egbert & Kastens 2007; Zheng et al. 2015). Images acquired with multispectral remote sensing systems have the capability to represent various crop properties – the retrieval of these surface properties are used for crop classification. Multispectral remote sensing data, particularly those covering the VIS and NIR bandwidths have been used in vegetation studies, mainly because the energy reflected in these regions directly relates to plant structure, plant pigmentation, as well as leaf and canopy moisture (McNairn et al. 2009).

Different band ratios, image transformations and texture information derived from various remote sensing datasets have been applied to crop type mapping with different image classification approaches, depending on the cropping patterns, geographical regions and field sizes (Nellis, Price & Rundquist 2009; Yang et al. 2015; Sun et al. 2016). For example, Peña-Barragán et al. (2011) used a set of vegetation indices and textural features derived from ASTER-imagery in combination with crop calendars to differentiate crop types, and found that vegetation indices contributed 90% to their models, while texture features were mainly useful for differentiating non-perennial crops when the optical data in question was used. Gilbertson & Van Niekerk (2017) compared the performance of several machine learning classifiers for classifying crop types using different datasets such as spectral bands, vegetation indices, image transformations (principal component analysis), textural features and a combination of all the features derived from Landsat-8 imagery. They found that, although principal component analysis outperformed all the scenarios, the difference in OA was only marginal when compared to what was achieved with combining all the features.

It is clear from the abovementioned studies that multispectral sensors provide the most cost-effective way of classifying crop types from a wide range of freely available sources (Wardlow,

Egbert & Kastens 2007; Sonobe et al. 2017; Sonobe et al. 2018). Common multispectral instruments used in agricultural applications include MODIS, Satellite Pour l'Observation de la Terre (SPOT), and Landsat. ESA recently embarked on a high spatial and temporal resolution Sentinel-2 mission, which is easily accessible and freely available. Sentinel-2 satellites provide improved spatial, spectral, radiometric, and temporal resolution imagery in comparison to the conventionally used satellite sensors (Galoppo, Castellani & Carriero 2018). With the undeniable significance of phenological features extracted from multispectral remote sensing imagery for crop type mapping, the high temporal resolution (5-day revisit frequency) offered by Sentinel-2 data provides a great opportunity for multi-temporal crop classification approaches, particularly given the sensor's high spatial resolution (10 m). Sentinel-2 sensors record data in 13 spectral bands, which includes two shortwave infrared bands and four red-edge bands, increasing the potential of these sensors for crop type mapping (Sonobe et al. 2017).

2.2 IMAGE PROCESSING

Sensor characteristics (e.g. spatial, spectral, temporal and radiometric resolutions) affect a system's ability to provide useful information about the subject of interest. In addition, satellite images are often negatively affected by radiometric, geometric and atmospheric distortions and consequently have to undergo a thorough pre-processing phase before it can be used for interpretation and analysis. To improve classification accuracies, the spectral information captured in an image can be modified to emphasize specific features through a procedure called image transformation (Campbell & Wynne 2011; Gilbertson 2017). Image transformations applied to pre-processed imagery have shown to improve the accuracy of remote sensing classifications (Lu & Weng 2007). Therefore, in addition to spectral bands, several image transformations such as spectral indices, image texture, principal component analysis (PCA) and tasselled cap transformation (TCT) are often used to classify remotely sensed imagery.

2.2.1 Pre-processing

Pre-processing refers to operations/processes undertaken to correct distorted or degraded data (Campbell 2007). Geometric correction is undertaken to correct errors caused by factors such as oblique viewing, relief displacement and displacement effects resulting from the rotation of the earth, as well as the satellite's scanning speed (Chuvieco & Huete 2010; Muller 2017). These errors can be corrected through the manipulation of digital numbers to adjust the image's projection until it matches a specific surface projection or shape (Barrett 2013). Due to variations in scene illumination and viewing geometry, atmospheric conditions and sensor noise and response, radiometric corrections may be necessary (De Jong & Van der Meer 2006). Radiometric

effects can be compensated for by sensor-specific calibration coefficient values, which are applied in a mathematical model for rectification (Muller 2017). In cases where images from different seasons are compared, the seasonal earth-sun elevation differences need to be accounted for. This rectification process normalises the pixel brightness values, assuming the sun was at the zenith on each date of image sensing (Lillesand, Kiefer & Chipman 2004).

When EM energy moves through the atmosphere, it interacts with particles and molecules, which may degrade the quality of the signal measured by the sensor and reduce the contrast of the image (Tempfli et al. 2009). For quantitative analyses, it is important to reduce these atmospheric effects and convert the digital numbers in the raw image to units such as absolute radiance or percentage surface reflectance. This conversion is essential when image data needs to be compared to ground measurements, or when imagery of different sensors acquired at different times needs to be compared to one another (Muller 2017). Each of these corrections varies, depending on the specific sensor and platform used to acquire the data, as well as the conditions under which the data are acquired (De Jong & Van der Meer 2006). In some cases, image providers apply some pre-processing operations and provide the data in a ready-to-use format (De Jong & Van der Meer 2006).

2.2.2 Transformations

Image transformation is the process where spectral information in an image is transformed or modified to emphasize specific features (Campbell & Wynne 2011). This is usually done with local or neighbourhood raster operators with the intention to visually enhance images and improve image classification (Campbell 2007). Image transformations improve image classification by reducing data dimensionality, emphasizing the variation between features, and reducing noise. Popular image transformations include indices, principal component analysis and texture measures (Heinl et al. 2009). These image transformations are used in addition to spectral bands to improve classification results (Myburgh 2012). The following section outlines some of the image transformations reported in the literature as being useful for crop type mapping.

2.2.2.1 Textural features

Texture is one of the most important features used in crop type mapping (Balasubramanian 2017). Texture features provide information about the spatial distribution of the intensity values within an image, the contrast, uniformity, rugosity, as well as regularity (Ruiz et al. 2011). A variety of quantitative texture measures have been developed and evaluated for crop type classification (Akar & Güngör 2015; Aguilar et al. 2015). Customarily, texture features are computed based on a pixel neighbourhood within an image. The most commonly used set of texture features was proposed

by Haralick & Shanmugam (1973). This includes 14 Gray-Level Co-Occurrence Matrix (GLCM) features (angular second moment, contrast, correlation, variance, inverse difference moment, sum average, sum variance, sum entropy, entropy, difference variance, difference entropy, information measures of correlation, maximal correlation coefficient dissimilarity). While Akar & Güngör (2015) used all 14 GLCM features to classify tea and hazelnut plantations, only a few of the GLCM texture features are commonly used for vegetation studies (Balaguer et al. 2010; Peña-Barragán et al. 2011; Schmedtmann & Campagnolo 2015).

Schmedtmann & Campagnolo (2015) used eight GLCM features for crop type classification (homogeneity, contrast, dissimilarity, entropy, angular 2nd moment, matrix mean, matrix SD and correlation), while Balaguer et al. (2010) used seven GLCM features, excluding the matrix mean. Peña-Barragán et al. (2011) also assessed the eight GLCM features for crop type classification and reported that only three (homogeneity, dissimilarity and entropy) are useful. The three texture features identified as optimal for crop type classification was later used by Peña et al. (2014) and Aguilar et al. (2015) for the classification of horticultural crops using multi-temporal Landsat-8 and Worldview-2 data, and they were found to be effective for crop type classification.

2.2.2.2 Vegetation indices

Solar irradiance varies with time and atmospheric conditions. This makes the simple measuring of light reflected from a surface insufficient for characterising that surface in a repeatable manner. One way of dealing with this limitation is combining data from several spectral bands to form what is widely known as a vegetation index (VI) (Jackson & Huete 1991). A vegetation index is defined as an algebraic construction based on the relationship between spectral bands (Crippen 1990). The most commonly used VIs are derivatives of data from discrete green, red and NIR bands recorded by most earth observation satellite sensors (Elvidge & Chen 1995). They can be calculated by ratioing, differencing, ratioing differences and sums, as well as through the formation of linear combinations of spectral band data. For example, red EM energy is strongly absorbed and the near-infrared EM energy strongly reflected by growing vegetation. The ratio of the red and near-infrared bands is thus expected to provide a useful indication of the growth vigour of a vegetation scene.

Generally, vegetation indices are generated to minimise solar irradiance and soil background effects while enhancing the vegetation signal (Jackson & Huete 1991; Basso, Cammarano & De Vita 2004); they are designed in a way that enables them to find a functional relationship between crop characteristics and remote sensing observations (Balasubramanian 2017). Their sensitivity to vegetation parameters makes them critical for vegetation studies (Basso, Cammarano & De Vita 2004). While a host of VIs have been developed and applied in vegetation studies, the most popular VIs include the aerosol free vegetation index (AFRI), atmospherically resistant vegetation index

(ARVI), enhanced vegetation index (EVI), green normalised difference vegetation index (GNDVI), infrared percentage vegetation index (IPVI), normalised difference vegetation index (NDVI), normalised difference moisture index (NDMI), ratio vegetation index (RVI) and soil-adjusted vegetation index (SAVI).

Most of the abovementioned VIs have been tested for crop type classification. Wardlow, Egbert & Kastens (2007) investigated the applicability of EVI and NDVI time-series data for crop-related land use and land cover classification. They found both indices to demonstrate similar seasonal responses to the crops considered, with the ability to separate most of the crop types. Satir & Berberoglu (2016) used NDVI, SAVI, perpendicular vegetation index (PVI), normalised difference water index (NDWI) and green vegetation index (GVI) for crop growth dynamics. NDVI was selected for its sensitivity to chlorophyll content, SAVI for its sensitivity to plant green cover and chlorophyll content, PVI for plant chlorophyll content, NDWI for water content and GVI for plant green structure. Although most VIs focus on the red and NIR regions of the spectrum where there is a strong increase in the reflectance of most plants, a few sensors, such as RapidEye and Sentinel-2, have additional red-edge bands between the red and near-infrared parts of the spectrum. Several studies demonstrated the potential of information extracted from these bands for vegetation studies (Ramoelo et al. 2012; Schuster, Förster & Kleinschmit 2012; Eitel et al. 2011). The next section gives an overview of the various VIs commonly applied to crop type mapping.

NDVI

It is clear that green plants absorb and reflect energy differentially in the visible and near-infrared regions of the spectrum. Rouse (1974) used the difference in the near-infrared and red reflectance values normalised over the sum of these values to develop the NDVI. The NDVI is expressed as:

$$NDVI = \frac{NIR - RED}{NIR + RED} \qquad \text{Equation 2.1}$$

Where *NDVI* is the normalised difference vegetation index;
NIR is the near-infrared image band; and
RED is the red image band.

The correlation of the NDVI with vegetation parameters such as biomass, green leaf area, photosynthetic activity, amongst others, makes it popular in vegetation studies (Peña-Barragán et al. 2011; Zheng et al. 2015; Massey et al. 2017). Although NDVI has been successfully used (Singh et al. 2017; Skakun et al. 2017), its sensitivity to light reflected from the soil background

exposed in-between crops and the loss of sensitivity in densely vegetated areas limit its applicability (Wardlow & Egbert 2008).

SAVI

SAVI was developed in an attempt to account for the limitations encountered with NDVI (Huete 1988). This includes minimising soil brightness influences, which are mostly prevalent in partially vegetated canopies (Huete, Liu & Van Leeuwen 1997). In plants that are photosynthetically active, the red extinction through the canopy will be higher than that of the NIR, resulting in more energy being reflected off the canopy background relative to the red. This secondary signal cannot be resolved with simple ratioing, necessitating a background correction L (Huete, Liu & Van Leeuwen 1997). Huete (1988) developed SAVI by adjusting the NIR-red wavelength space origin to various isoline convergence points, which is equivalent to adding a constant L to the NIR-red reflectance data. To maintain the bounded conditions of the NDVI which must remain between -1 and 1, a multiplication factor (1+L) is needed. This is expressed in the formula presented in Equation 2.2.

$$SAVI = \frac{NIR - RED}{NIR + RED + L} \times (1 + L)$$ Equation 2.2

Where *SAVI* is soil-adjusted vegetation index;
NIR is the near-infrared image band;
RED is the red image band; and
L is the relative soil constant.

According to Huete, Justice & Liu (1994), an L factor of 0 is sufficient for use when the soil brightness is minimal in the area of interest, thus in areas with less exposed soil backgrounds. With an L factor of 0.5, able to reduce soil brightness variation while eliminating the need for further calibrations, SAVI has been used in conjunction with other vegetation indices for crop type classification (Foerster et al. 2012).

ARVI

Following the limitation of NDVI under atmospheric influences, Kaufman & Tanre (1992) developed the ARVI to minimise atmospheric-induced variations. This index is based on the fact that red radiance is more affected by atmospheric influences than NIR radiance and thus utilises the difference in radiance between the blue and red bands to modify the radiation value of the red band. ARVI is expressed as:

$$ARVI = \frac{NIR - RED}{NIR + RED} - \frac{y(RED - BLUE)}{y(RED + BLUE)}$$ Equation 2.3

Where *ARVI* is the atmospherically resistant vegetation index;
NIR is the near-infrared image band;
RED is the maximum score;
BLUE is the blue image band; and
Y is the weighting function.

The y is a weighting function for the difference in reflectance between the two bands, serving as an indicator of the atmospheric conditions. While different values can be chosen for γ, depending on the type and size of the aerosol, Kaufman & Tanre (1992) suggested 1 as the most appropriate value, especially when the type of aerosol is unknown.

EVI

Another widely used vegetation index is EVI, which is an optimised index for the enhancement of the vegetation signal. EVI provides improved sensitivity especially in high biomass regions, while reducing soil and atmospheric influences (Jiang et al. 2008). EVI also improves the linearity with vegetation biophysical parameters (Houborg, Soegaard & Boegh 2007). Furthermore, it has strong linear relations and synchronizes well with seasonal photosynthesis measurements in terms of phase and amplitude, without any saturation even in densely vegetated regions (Xiao et al. 2005). Wardlow, Egbert & Kastens (2007) noted that while NDVI saturates at the peak of the growing season over cropland, EVI exhibited more sensitivity during this development stage. EVI is given by the formula below:

$$EVI = G\frac{NIR - RED}{NIR + C_1 RED - C_2 BLUE + L}$$ Equation 2.4

Where *EVI* is the enhanced vegetation index;
G is the gain factor;
NIR is the near-infrared image band;
RED is the red image band;
BLUE is the blue image band;
C_1 is the first aerosol resistant coefficient;
C_2 is the second aerosol resistant coefficient; and
L is a canopy background adjustment factor.

Both C1 and C2 coefficients use the blue band to correct for aerosol influences in the red band. L serves as the soil-adjustment factor as in SAVI (Equation 2.2), but its value varies from the L in

SAVI. This is attributed to the interaction and feedback between the soil-adjustment factor and the aerosol resistance term (Liu & Huete 1995). Jiang et al. (2008) suggested L=1, C1=6, C2=7.5, and G=2.5 to be the most appropriate for the MODIS EVI algorithm. EVI has been used in many different applications, including land use/land cover change detection, vegetation biophysical parameter estimation and crop type identification (Wardlow, Egbert & Kastens 2007; Houborg, Soegaard & Boegh 2007; Sims et al. 2008; Zhong et al. 2016; Gilbertson, Kemp & Van Niekerk 2017).

AFRI

The resilience of the shortwave infrared wavelength to aerosol effects and atmospheric gasses, coupled with its sensitivity to vegetation, is the basis upon which the AFRI was developed. This is due to the wavelength of shortwave infrared being much larger than the radius of most aerosols, giving it the ability to bypass suspended particles in the atmosphere. Consequently, AFRI is able to produce a realistic vegetation condition image (Karnieli et al. 2001). AFRI is given by:

$$AFRI = NIR - 0.66\frac{SWIR}{NIR + 0.66(SWIR)} \qquad \text{Equation 2.5}$$

Where $AFRI$ is the aerosol free vegetation index;
NIR is the near-infrared image band;
0.66 is the empirical linear relationship factor; and
$SWIR$ is the shortwave infrared image band.

The 0.66 value is based on the empirical linear relationship between the red and shortwave infrared bands. Thus, AFRI uses the shortwave infrared band to replace the red band based on the empirical linear relationship (0.66), taking full advantage of the shortwave infrared band's ability to penetrate atmospheric aerosol influences, while remaining sensitive to vegetation (Zhong et al. 2016).

GNDVI

The NDVI is sensitive to low chlorophyll concentrations, thus the absorbed photosynthetically active solar radiation (Yoder & Waring 1994) is not sensitive to higher chlorophyll concentrations or large vegetation coverage photosynthesis rates (Gitelson, Kaufman & Merzlyak 1996). The GNDVI was developed to account for this limitation. Because the green band has a near-linear relationship with chlorophyll content, this band was used instead of the red band of the NDVI in the development of the GNDVI. GNDVI is given by:

$$GNDVI = \frac{NIR - GREEN}{NIR + GREEN} \qquad \text{Equation 2.6}$$

Where *GNDVI* is the green normalised difference vegetation index;
NIR is the near-infrared image band; and
GREEN is the green image band.

This index has been reported to be more sensitive to the concentration of chlorophyll than NDVI and has been used in several vegetation studies (Hunt et al. 2011; Ghosh & Behera 2018; Muhd-Ekhzarizal et al. 2018; Ranjan et al. 2019).

IPVI

The IPVI measures the percentage of near-infrared radiance in relation to the combined radiance of both the near-infrared and red bands. IPVI differs from NDVI in that it eliminates the subtraction of the red radiance and, as such, it ranges between 0 and 1 (Crippen 1990). IPVI is expressed as:

$$IPVI = \frac{NIR}{NIR + RED}$$ Equation 2.7

Where *IPVI* is the infrared percentage vegetation index;
NIR is the near-infrared image band; and
RED is the red image band.

Although IPVI is similar to NDVI, it is less complex. Considering the strengths and limitations of the various indices explained above, most researchers use multiple VIs together for improved results (Palchowdhuri et al. 2018; Sonobe et al. 2018; Sun et al. 2019). Many other VIs have been developed and used for crop type mapping – for an incisive description of more VIs, the reader is referred to Gilbertson (2017).

2.2.2.3 Statistical manipulations

With the increasing dimensionality (e.g. number of bands and transformations) in remote sensing datasets, there is a need to devise methods for dimensionality reduction in an interpretable manner, while preserving the quality of the dataset as much as possible (Jolliffe & Cadima 2016). While various methods have been developed for this purpose, principal component analysis (PCA) decorrelates redundant information by concentrating the information of interest into specific principal components. PCA is a multivariate statistical method that selects uncorrelated linear combinations of variables in an n-dimensional space. This is done in a way that each successively extracted linear combination (principal component) has a smaller variance (Almeida & Filho 2004). This makes PCA one of the most commonly used data reduction and feature extraction methods (Cruz-Cárdenas et al. 2014). The approximate contribution of each variable to each

principal component calculated can be roughly estimated by examining the eigenvectors of the original variables (Loughlin 1991).

Cruz-Cárdenas et al. (2014) used PCA for agricultural crop classification and found that it handles sparse data well, while generating fewer and improved association rules. By deriving the uncorrelated linearly transformed components from the original data, the first principal component has been found to account for most of the variance of the original data set. The subsequent components account for the maximum proportion of the unexplained residual variance. Stellacci et al. (2012) applied PCA to hyperspectral data for investigating plant responses and status. They found that the first principal component of the visible region explained over 95% of the total variance, while in the red-edge and infrared regions, the first two principal components together explained about 81% of the total variance. It is clear from these findings that the first few principal components are the most useful for vegetation studies. Based on a scree test, Gilbertson, Kemp & Van Niekerk (2017) found that the first four principal components computed from ten Landsat-8 image bands explained most of the total variance and were the most useful for crop type mapping. This corresponds to findings by Stellacci et al. (2012).

Similar to PCA, tassel cap transformation (TCT) is a method used to compress spectral data from an optical sensor into a few bands related to a scene's physical characteristics with minimal information loss (Huang et al. 2002). TCT was originally developed by Kauth & Thomas (1976) for Landsat MSS but has been adapted to other sensors, such as MODIS (Lobser & Cohen 2007), owing to its value for discovering vegetation patterns using different combinations of bands. Therefore, since TCT was originally developed for Landsat MSS, the coefficients used need to be adjusted to befit the later sensors, such as Sentinel-2.

2.2.3 Classification

Image classification is defined as the process of assigning and grouping image pixels or objects with specific characteristics into specified informational classes (Campbell 2007). There are three commonly used image classification approaches, namely: unsupervised, supervised and knowledge-based (Gilbertson, Kemp & Van Niekerk 2017).

2.2.3.1 Unsupervised image classification

Unsupervised image classification is the identification of natural groupings of pixels within multidimensional feature space (Campbell 2007). The natural groupings are commonly known as spectral classes (Campbell 2007). Once these spectral classes have been determined, the user assigns each class to a more meaningful or appropriate informational class (Mather 2004). Although unsupervised classifiers require no prior knowledge of the objects to be classified, the

interpreter is responsible for specifying the number of expected spectral classes and assigning informational classes to each spectral cluster (Oyekola & Adewuyi 2018). Examples of unsupervised classifiers include Euclidean and Mahalanobis distance (Mather & Magaly 2011), with the most common being the iterative self-organizing data algorithm (ISODATA) classifier (Muller 2017). Thanks to its limited user involvement requirements, unsupervised image classification is quick and relatively easy to implement (Gao 2009) and is consequently frequently employed for land cover classifications (Nolin & Payne 2007; Lang et al. 2008; Rozenstein & Karnieli 2011; Oyekola & Adewuyi 2018).

2.2.3.2 Supervised image classification

Supervised classification involves the labelling of pixels/objects with unknown identity using pixels/objects with known identity, called training data (Campbell 2007). The success of supervised classification depends on the user's prior knowledge of the study area. This classification approach grants the user more control over the informational classes, compared to unsupervised classification. Supervised classifiers can be categorized into two groups, namely: parametric (statistical) and non-parametric (machine learning) algorithms. Parametric classifiers require training data to be normally distributed, as they depend on statistical measures such as mean, standard deviation, and probability to perform properly (Mather 2004). Non-parametric classifiers often incorporate artificial intelligence into the learning process, and iteratively learn how to classify images (Campbell & Wynne 2011). Consequently, non-parametric classifiers are considered to be more robust and tend to perform better than traditional classifiers (Myburgh 2012; Gilbertson, Kemp & Van Niekerk 2017). This section thus focuses on the latter type of classifiers.

Non-parametric machine learning algorithms use known data to classify large sets of unknown data, while incorporating ancillary and spatial data (Breiman 2001). In contrast to statistical approaches such as minimum distance (MD), ML and parallel-piped, the ability of these algorithms to handle input variables that are not normally distributed (Al-Doski, Mansorl & Shafri 2013), makes them effective for combining nominal, ordinal, ratio, and interval data into classification tasks (Gilbertson, Kemp & Van Niekerk 2017). They have also been reported to be robust under conditions of high dimensionality (Zheng et al. 2015). The most common machine learning image classification algorithms are RF, decision trees (DTs), SVM, and k-NN.

DTs recursively split training data into homogeneous subdivisions based on a statistical test (Chuvieco & Huete 2010). With every split, logical rules with the capacity to mimic the statistical divisions are inferred, resulting in a hierarchical ruleset capable of classifying an image. The developed set of rules allows for easy interpretation and flexibility (De Colstoun et al. 2003; Myburgh & Van Niekerk 2013). Pal & Mather (2003) reported DT to be computationally fast and

able to handle datasets represented on different measurement scales. The pruning of DTs makes them smaller and easier to interpret. However, this classifier has been reported to perform poorly under conditions of high dimensionality (Pal & Mather 2003). According to Prasad, Iverson & Liaw (2006), DTs are also sensitive to minor changes in training data and have been reported to be unstable, which could lead to overfitting. Duro, Franklin & Dubé (2012) compared DT, RF and SVM for agricultural landscape classification using SPOT-5 imagery with both pixel- and object-based approaches and found that DT produced satisfactory results, although its performance was inferior to SVM and RF with both approaches. When compared with ML and artificial neural networks (ANN), Pal & Mather (2003) reported DT to be superior when high-dimensional data was used.

RF is an ensemble DT classification method (Rodriguez-Galiano et al. 2012). It uses bootstrapping with replacement to enhance the diversity of DTs, which allocates each pixel to a class, based on the maximum number of votes from the collection of trees (Rodriguez-Galiano et al. 2012). RF can be viewed as an advanced version of the bagging algorithm (Breiman 2001), although the former differs from RF in that it splits each tree node using the best split among all variables. In contrast, RF splits each tree node using the best among a subset of predictors randomly chosen at that tree node, thereby creating a new dataset from the original dataset. A tree is then grown using random feature selection without pruning the grown trees (Breiman 2001; Archer & Kimes, 2008). RF has some advantages over other classifiers in that it is faster compared to statistical classifiers, robust against overfitting compared to classifiers such as DT, and permits the formation of as many trees as the user wants (Breiman et al. 1984). Watts & Lawrence (2008) applied RF to Landsat imagery within the object-based image analysis paradigm to map agricultural areas and found it to be very effective, with OAs exceeding 82%. Jay et al. (2009) used RF to classify complex and homogeneous plant groups, with overall accuracies exceeding 85%. Akar & Güngör (2012) compared RF with ML to classify six different crop types with SPOT-5 images and found RF to be superior, with an overall accuracy difference of 8%.

Another popular non-parametric classifier is SVM (Vapnik 1995), which is based on statistical learning theory and risk reduction (Zheng et al. 2015). This classifier relies on the identification of the optimal separating hyperplane, which ensures a maximum margin between the hyperplane and the nearest training samples (support vectors) for each class in feature space (Myburg & Van Niekerk 2013). SVM uses a kernel function to resolve optimisation problems in high-dimensional spaces and accounts for data that cannot be linearly separated (Mountrakis, Im & Ogole 2011). The selection of an appropriate kernel function and kernel parameters is, however, application-specific and may have a significant impact on classification results. Some of the advantages of

SVM include performing well with limited training data (Shao & Lunetta 2012), robustness to high dimensionality, and overall superior classification accuracies compared to other non-parametric classifiers (Gilbertson, Kemp & Van Niekerk 2017). Nitze, Schulthess & Asche (2012) compared SVM, RF, ANN and ML for crop type classification and found SVM to be superior in terms of overall classification accuracies and robustness. Mathur & Foody (2008) applied SVM to SPOT HVR data to classify agricultural crops. They used data with mixed spectral responses to assess the difference in the performance of SVM and found that it was able to perform equally well with the unconventional data (92%) as it did with the conventional data (90.7%).

K-NN uses the k-NN rule to assign an unknown sample to the class that occurs most frequently among its k-nearest neighbours in feature space (Myburgh & Van Niekerk 2013). Nearest neighbour (NN) is an implementation of k-NN, with the variable k being set to 1. Both k-NN and NN classifiers offer simplicity over other more complex classifiers (Campbell 2007). One of the shortcomings of k-NN is its dependence on the selection of k; which has been reported to be difficult to set (Prasad, Iverson & Liaw 2006). Furthermore, pooling nearest neighbours from training data that might contain overlapping classes may in some cases be unsuitable. K-NN is also susceptible to the curse of dimensionality as the distance metric plays a major role in the performance of the classifier (Samaniego & Schulz 2009). Thanh Noi & Kappas (2018) compared k-NN, SVM and RF, using Sentinel-2 for land use/cover classification and reported overall accuracies between 90–95% across all classification results. Gilbertson, Kemp & Van Niekerk (2017) compared k-NN, DT, SVM and RF with Landsat imagery for crop type identification and recorded overall accuracies between 77–94%.

Although non-parametric classifiers have proven to perform better than statistical classifiers, ML remains one of the most employed statistical classifiers in remote sensing (Waske et al. 2010; Stephenson 2010). The ML classifier has been the algorithm of choice for many applications (Pal & Mather 2003; Chen et al. 2018; Esetlili et al. 2018; Nigam et al. 2019). ML is dependent on estimates of the mean vector and the variance-covariance matrix, which are used to determine class probabilities for unknown samples and for assigning samples to classes with the highest probability (Myburgh & Van Niekerk 2013). ML is often used as a benchmark when evaluating classifiers (Stephenson 2010; Szuster, Chen & Borger 2011). Some of the recorded shortcomings of ML include its sensitivity to the quality of training data (Campbell 2007) and the assumption that the data is normally distributed.

2.2.3.3 Knowledge-based image classification

Knowledge-based image classification uses the expert systems approach to classify data. Expert systems are in essence computer systems that emulate human decision-making by taking a

predefined set of rules into consideration (Campbell & Wynne 2011). This approach is becoming increasingly attractive due to its ability to accommodate multiple sources of data. For example, ancillary data such as elevation, slope, and aspect can be used to develop rules in relation to vegetation distribution in mountainous regions (Hodgson et al. 2003). Thus, expert systems use relationships between variables in a classification procedure to improve classification accuracies. Nangendo, Skidmore & Van Oosten (2007) illustrated how incorporating expert rules significantly increased classification accuracy for mapping East African tropical forests in Uganda. Cohen & Shoshany (2002) compared a knowledge-based approach to unsupervised classification for crop recognition in central Israel and found that the former approach returned superior results. Although knowledge-based approaches have been found effective for vegetation mapping, Gumbricht, McCarthy & Mahlander (1996) demonstrated that creating a usable ruleset is time-consuming (Liu, Skidmore & Van Oosten 2002).

2.2.4 Accuracy assessment

Although accuracy assessment was important even with traditional remote sensing techniques, the complexity of digital classification increases the need to assess the reliability of the results (Congalton 1991). An error matrix, which is a square array of numbers set out in columns and rows, expressing the number of sample units assigned to a specific class relative to the actual class as corroborated on the ground, has been the most common method of assessing the accuracy of remote sensing results (Janssen & Vanderwel 1994; Congalton & Green 2002; Gilbertson 2017). In the error matrix, the rows represent the classification generated from remote sensing data, while the columns represent the reference data (Story & Congalton 1986).

The error matrix is used as a starting point for a series of descriptive and analytical statistical techniques. The two most commonly used statistics are overall accuracy (OA) and Kappa coefficient (K). OA is generated by dividing the total correct instances (pixels or objects) by the total number of instances. OA is easy to interpret because the percentage of classified pixels/objects corresponds to errors of commission and omission (Congalton & Green 2008). K, on the other hand, measures how well a classifier performed compared to how well a random classification would have performed and is therefore used to assess the statistical difference between classifications (Foody 2002).

Accuracies of individual classes can be generated in a similar manner by computing the producer's accuracy (PA) and user's accuracy (UA). PA is achieved by dividing the number of correct pixels/objects in that class by either the total number of pixels/objects in the corresponding row or the corresponding column. This measure indicates the probability of a reference pixel being correctly classified and is also called the error of omission. On the other hand, if the total number

of correct pixels/objects in a class is divided by the total number of pixels/objects that were classified in that class, the result is known as the UA, or error of commission. UA indicates the probability of a pixel/object classified on the map/image actually representing that class on the ground (Story & Congalton 1986).

2.3 MULTI-TEMPORAL IMAGERY FOR CROP TYPE MAPPING

The success of optical imagery for crop type mapping has been coupled with multi-temporal techniques (Salehi, Daneshfar & Davidson 2017). As early as the 1970's, Bauer & Cipra (1973) used single-date Earth resources technology satellite (ERTS MSS) data to identify major crop types and suggested that the use of multi-temporal data can improve classification performance as the spectral characteristics of vegetation change over time, depending on phenology, atmospheric conditions and illumination conditions (De Carvalho et al. 2004). The ability to acquire images throughout the growing season enables the recording of subtle differences and changes in absorption and reflectance spectra, making the temporal dimension of remotely sensed data the most useful for identifying crop types (Liu, Ozdogan & Zhu 2013). The varying surface properties and growth process (phenology) of crops directly influence the reflected signal and it is on this basis that the multi-temporal classification techniques are used to identify crop types (Del Frate, Ferrazzoli & Schiavon 2003; Karjalainen, Kaartinen & Hyyppä 2008; Sabour, Lohmann & Soergel 2008).

Multi-temporal approaches for crop type classification include creating a time-series profile of vegetation indices, texture measures, image transformations, etc. (Murakami et al. 2001; Ippoliti-Ramilo, Epiphanio & Shimabukuro 2003; Hao et al. 2015; Gilbertson, Kemp & Van Niekerk 2017) or analysing imagery as a multi-date stack (Oetter et al. 2001; Murthy, Raju & Badrinath 2003; Xiao et al. 2005; Biggs et al. 2006; Xavier et al. 2006). The success of multi-temporal approaches for crop type classification has been reported to be greatly dependent on the availability of multi-temporal imagery (cloud-free) with high spatial resolution (Broge & Mortensen 2002; Doraiswamy et al. 2005). However, with most existing satellite sensors, high spatial resolution comes at the expense of reduced temporal resolution. For example, readily available satellite sensors such as MODIS collect data at a coarse spatial resolution of 250 m to 1 km with a daily revisit time (Maccherone & Frazier, 2010). Liu, Ozdogan & Zhu (2013) used images with varying resolutions to assess the contribution of both temporal and spatial resolutions to crop type classification accuracies and reported that the incorporation of high temporal frequency and low spatial resolution images into the classification process improved accuracies by up to 20%, even if few or no high-resolution images are available. They further found this boost in accuracy to be comparable to what can be achieved when an additional high spatial resolution image is added to

a low spatial resolution temporal stack. To investigate the significance of both temporal and spatial resolutions, Keifer (2014) used multi-temporal MODIS imagery to classify agricultural crops and found that, while the use of high temporal frequency and coarse spatial resolution data was successful in separating croplands from non-croplands, it was not as successful in identifying individual crops. According to Ozdogan & Woodcock (2006), the limited success of high temporal and coarse spatial resolution data for crop type identification is because medium to high spatial resolutions are required to resolve individual fields (Inglada et al. 2015).

The launch of satellite constellations such as Sentinel-2 bridged the gap between temporal and spatial resolution by providing data with relatively high spatial and temporal resolution when compared to traditional sources of imagery (e.g. Landsat). But even with the unprecedented improvement in both the spatial and temporal resolution of Sentinel-2, data availability is still negatively affected by cloud cover (Kussul et al. 2015). While it may sometimes be possible to acquire cloud-free images covering critical crop development stages in a growing cycle (Hao et al. 2015; Gilbertson, Kemp & Van Niekerk 2017), it is not always a viable option, particularly when the intention is to develop an automated crop type mapping system (Inglada et al. 2016). Image compositing is one of the most prominent and common approaches to dealing with cloud-contamination. The next section provides an overview of image compositing and commonly used techniques, as well as image selection approaches for reducing the effects of clouds, with specific focus on crop type mapping.

2.3.1 Image compositing

The presence of clouds in imagery has been recognised as a source of error in the retrieval of many surface parameters using multispectral data (Kussul et al. 2015; Sun et al. 2017). One solution is to filter out cloud-contamination by combining images from different dates, using image compositing (Athick & Naqvi 2016). Image compositing is basically the aggregation of image observations within a stipulated time-frame and the replacement of poor quality observations with good-quality observations (Lück & Van Niekerk 2016). The objective of compositing is to minimise all factors (clouds and cloud shadow, atmospheric variations, view angle effects, and soil background variations) disturbing the pure top-of-canopy (TOC) signal at a certain observation geometry (Sun et al. 2016). It is further applied to reduce the size of large datasets of satellite imagery, with often redundant or contaminated observations, into single datasets of uncontaminated and valid data (Hagolle et al. 2004). Such techniques have traditionally been used with low spatial and high temporal resolution images such as those captured by MODIS and AVHRR (Qi 1993), but it has recently gained popularity with higher spatial resolution imagery, mainly due to the rich archive of historical imagery that has been made available by space agencies.

For example, Roy, Kucukural & Zhang (2010) applied image compositing on Landsat imagery to produce cloud-free images. Lück & Van Niekerk (2016) noted that, due to spectral differences among the different compositing periods, the consideration of phenological characteristics between different compositing periods in the time-series is crucial for the accurate classification of vegetation. Although there is no consensus on the best image compositing techniques for crop type mapping, a number of compositing techniques have been developed with the aim of retaining as much information as possible (Dennison, Roberts & Peterson 2007). The following section evaluates some of the common compositing techniques.

Based on the literature, the maximum value composite (MVC) – also known as the MaxNDVI – seems to be the most popular multi-temporal image compositing method. MaxNDVI is computed by selecting the observations in an image with the maximum NDVI value in the time-series (Holben 1986). This approach is based on the assumption that a higher NDVI value indicates a lower cloud fraction (Fraser, Massom & Michael 2009). Although MaxNDVI has been reported successful for vegetation monitoring (Kasischke et al. 1993; Diwakar et al. 1989; Potter & Brooks 2000; Du et al. 2001; Peters et al. 2002), there are some defects associated with this technique. Holben (1986) reported that MaxNDVI does not completely solve the problem of cloud-contamination and can be unstable in areas with medium- to low-density vegetation cover. Qi (1993) found that the dependence of MaxNDVI on NDVI may result in discrepancies in the final composite, due to the vulnerability of the NDVI to soil background variations and atmospheric effects (Roy, Kucukural & Zhang 2010). Attempts to resolve these issues included, amongst others, using SAVI (Huete 1988) and ARVI (Kaufman & Tanre 1992), instead of the NDVI. However, both modifications failed due to the coupled effects of soil background and atmospheric effects. Thus, while MaxNDVI may be useful for applications such as forestry (Kross et al. 2011; Maxwell & Sylvester 2012), it is not always a viable option in areas with low vegetation cover.

An alternative to MaxNDVI is the MinRed compositing procedure, proposed by D'Iorio (1991) and used by De Wasseige et al. (2000) and Cabral et al. (2003). MinRed was compared with MaxNDVI and maximum ratio (MaxRatio) by Luo, Trishchenko & Khlopenkov (2008), who found that, although the MinRed was successful in eliminating clouds, it is biased towards cloud shadows and retained the shadow-contaminated pixels in the final composite. Their findings agreed with those of Holben (1986) and Qi (1993), who observed that MaxNDVI was able to eliminate both clouds and shadows when the targeted areas are completely vegetated, but suffered from soil interferences when surfaces are partially vegetated. Cihlar, Manak & Voisin (1994) evaluated five image compositing approaches, including MaxNDVI, maximum apparent temperature (MAT), maximum difference of different channels (MDC), maximum temperature

(MaxT) and minimum scan angle (MSA) for producing image composites from AVHRR imagery, with the intention to obtain image composites that approximated a single-date image with a constant, near-nadir geometry. The authors concluded that none of the five methods yielded composites that consistently resembled the nadir image, even for reasonably long compositing periods. They attributed the failure of these methods to insufficient correction for bidirectional effects. Lück & Van Niekerk (2016) compared several compositing techniques on high-resolution Landsat-5 thematic mapper (TM) and Landsat-7 enhanced thematic mapper plus (ETM+) imagery. They found that MaxRatio performed better than the MinRed and MaxNDVI, while the MinRed produced the least accurate results.

According to Vancutsem et al. (2007), although the aforementioned approaches minimise the artefacts encountered with the MaxNDVI method, selecting a single extreme value, such as a minimum or maximum, often favours specific atmospheric and geometric conditions, which may cause spatial inconsistencies in the composites. Moreover, single value selection criteria use a small part of the available information, even when several observations are cloud-free. To account for some of these shortcomings, Vancutsem et al. (2007) proposed the MC approach, which was later used by Hüttich et al. (2011). This approach was proposed as an alternative to the single extreme value approaches, such as the minimum or maximum values. The MC approach averages all the reflectance values acquired within a stipulated compositing period to create a new image.

Another alternative to the extreme value compositing is the use of a median value. Brems, Lissens & Veroustraete (2000) developed and used the median composite of fuzzy multispectral estimate (MC-FUME) method to create ten-day composites of SPOT vegetation imagery. MC-FUME involves two steps (Brems, Lissens & Veroustraete 2000). The first step involves an approximate bidirectional reflectance distribution function correction, while the median of the estimated TOC reflectance values is calculated in the second step. This approach was reported by Brems, Lissens & Veroustraete (2000) and Lissens, Veroustraete & Van Rensbergen (2000) to be superior to the classic MaxNDVI approach. The success of using the median value of several spectral reflectance values was validated by Flood (2013), who employed a multidimensional analogue of the median (MEDOID) method for selecting representative observations. They defined the MEDOID as a "measure of centre" of a multivariate set of points, similar in nature to the median of a univariate dataset. This method requires the images to be corrected for atmospheric and bidirectional reflectance distribution function (BRDF) effects. They reported the insensitivity of this approach to outliers to be an advantage, especially when the purpose of the compositing is to reduce the impact of clouds, given that outliers still occur even after atmospheric and BRDF corrections and

cloud/shadow masking. The authors argued that using the mean of all observations is more sensitive to outliers and is thus less effective for image compositing.

In addition to the image compositing approach employed, the compositing period plays an important role in the outcome of the final composite (Loveland et al. 2000). According to Pouliot et al. (2011), the appropriate compositing period for imagery with a 24-hours temporal resolution is 6–8 days. The compositing period, however, depends on the intended application. For detecting plant developmental stages, 10–14 day averaged composites are more suitable. Loveland et al. (2000) consolidated 10–day image composites into monthly composites to reduce data volume and improve data quality. They showed that data quality can be increased by using longer compositing periods (monthly) because this increases both the likelihood of cloud-free coverage and overall data completeness. This is particularly important when using data with longer revisit frequencies in areas affected by frequent cloud cover. Hüttich et al. (2011) used MODIS time-series data to assess the effects of temporal compositing lengths by testing varying compositing lengths for land cover mapping. They found that monthly composites created by re-compositing 10-day composites produced the most accurate results. Most compositing periods range between 16 days and three months, but Friedl et al. (2010) reported that monthly composites are generally more effective. This observation corresponds with those of Townshend & Justice (1986) and Tucker et al. (1985). The next section looks into image selection as an alternative approach to image compositing for reducing the effects of clouds on remotely sensed data.

2.3.2 Image selection

Another way of dealing with cloud-contaminated observations is to select cloud-free images covering key periods in the growing cycles of crops (Hao et al. 2015). Several authors found selecting images at key periods, such as the initial green-up and late senescence phases of crop types, to be sufficient for accurate crop type classification (Brown et al. 2013; Hao et al. 2015). Sabour, Lohmann & Soergel (2008) suggested that image selection based on a crop calendar is beneficial and generally gives more accurate results than using all images covering a growing season. This is because some fields are covered by different types of crops during the year (Lohmann et al. 2009). Simonneaux et al. (2008) found that eight selected Landsat TM images representative of crop developmental stages were effective in identifying four main crop types using a decision tree classifier. Peña-Barragán et al. (2011) selected three images corresponding to major phases in the growing season to differentiate crop types and achieved classification accuracies exceeding 75%.

Hao et al. (2015) assessed the impact of time-series length on crop type classification accuracies. They compared eight time-series lengths, ranging from one month to eight months, and found that

adding features past five months had no significant impact on classification accuracies. They suggested that five months of images are most effective for classifying crop types. This agrees with Gilbertson, Kemp & Van Niekerk (2017), who used five images representing different key periods in the growing season and reported high accuracies (> 90%) in mapping selected crop types. Schmedtmann & Campagnolo (2015) also selected five images and reported accuracies exceeding 80%.

Although most studies agree on the benefits of selecting optimal dates for crop type classification, it is not always possible or practical to do so. For example, Inglada et al. (2016) proposed an automated crop type map production system and used all available images to circumvent cumbersome manual image selection procedures.

2.4 SUMMARY

The literature review revealed that, although remote sensing has been successfully employed for crop type classification, more research is necessary to transition from experimental work to operational crop type classification systems. The selection and use of images representing optimal stages in the growing circle was identified as an effective way of utilising multi-temporal data for crop type classification, while minimising the impact of clouds. While this approach has been successful in classifying crops, it is not viable for operational crop type production, since it requires a thorough analysis of relevant crop calendars, which can vary considerably from one region to another. For operational crop type mapping production systems it would, therefore, be beneficial to determine the value of selecting optimal dates against using all available images. The latter approach would be much easier to automate. An alternative to image selection is image compositing, which can minimise the effect of clouds. Although several compositing approaches have been developed, it is not clear to what extent their use will improve classification accuracies.

Early crop type detection is critical for yield forecasting, food security predictions and commodity trading. However, crop acreage estimations are usually carried out very late in the season – in many cases during or after harvesting has been completed. The recent improvements in the spatio-temporal resolutions offered by imagery such as Sentinel-2 provide new opportunities for generating crop type maps earlier in the season. There is thus a need for the development of accurate and cost-effective methods for operational crop type map production.

The next chapter (Chapter 3) focuses on the pre-harvest classification of crop types; while the following chapter (Chapter 4) investigates the value of image compositing. In both cases, machine learning and Sentinel-2 imagery are employed. Chapter 3 was submitted as a scientific article to

Computers and Electronics in Agriculture and is currently in review, while Chapter 4 is in preparation for submission.

CHAPTER 3: PRE-HARVEST CLASSIFICATION OF CROP TYPES USING A SENTINEL-2 TIME-SERIES AND MACHINE LEARNING

3.1 ABSTRACT

Timely crop type information (preferably before harvest) is useful for predicting food surpluses or shortages. This study assesses the performance of several machine learning classifiers, namely: support vector machine (SVM), decision tree (DT), k-nearest neighbour (k-NN), random forest (RF) and maximum likelihood (ML) for crop type mapping based on a series of Sentinel-2 images. Four experiments with different combinations of image sets were carried out. The first three experiments were undertaken with 1) single-date (uni-temporal) images; 2) combinations of five images selected from the best-performing single-date images and 3) five images manually selected, based on crop developmental stages. The fourth experiment involved the chronologic addition of images to assess the performance of the classifiers when only pre-harvest images are used, with the purpose of investigating how early in the season reasonable accuracies can be achieved. The experiments were carried out in two different sites in the Western Cape Province of South Africa to provide a good representation of the grain-producing areas in the region, which has a Mediterranean climate. The significance of image selection on classification accuracies was evaluated, as well as the performance of machine learning classifiers when only pre-harvest images are used. The classification results were analysed by comparing overall accuracies and kappa coefficients, while McNemar's test and analysis of variance (ANOVA) were used to assess the statistical significance of the differences in accuracies among experiments. The results show that by selecting images based on individual performance, a viable alternative to selecting images based on crop developmental stages is offered, and that the classification of crops with an entire time-series can be just as accurate as when they are classified with a subset of hand-selected images. We also found that good classification accuracies (77.2%) can be obtained with the use of SVM and RF as early as eight weeks before harvest. This result shows that pre-harvest images have the potential to identify crops accurately, which holds much potential for operational within-season crop type mapping.

3.2 INTRODUCTION

The need to produce more food for the growing global population, as well as increasing biofuel production put continuing pressure on limited agricultural resources (Inglada et al. 2016). Consequently, most agricultural systems around the world are being intensified, which makes agricultural practices highly dynamic as new technologies are implemented to ensure that food supply meets demand. Intensive and dynamic agricultural systems require innovative, timely,

objective and cost-effective methods for effective monitoring and management. Crop type information is particularly useful for monitoring and managing the sustainability of agricultural resources. Such information is also useful for generating crop statistics, which aid decision-making regarding subsidy payments and the calibration of crop models (Peña-Barragán et al. 2011). Crop type information further provides a basis from which to make economic forecasts, such as the estimated contribution (and impact) of agricultural activities to the gross domestic product (GDP) (McNairn et al. 2014; Siachalou, Mallinis & Tsakiri-Strati 2015; Immitzer, Vuolo & Atzberger 2016). Also, major food security programmes such as food aid, strategic food reserves, import and export licensing for private firms and distribution through social security programmes depend on crop production forecasts derived from crop type information (Jayne & Rashid 2010; Foley et al. 2011).

According to Peña et al. (2014), traditional methods for producing crop type maps require multiple sources of information, for example, ground and aerial surveys. These methods are tedious, laborious and costly and are reported to produce inconsistent results (Gilbertson, Kemp & Van Niekerk 2017). In addition, they can be biased as they may often rely on a small number of observations made at easily accessible sampling sites (Peña-Barragán et al. 2008). The use of remote sensing and freely available satellite imagery is a viable alternative as it enables cost-effective mapping and continuous monitoring of crop fields across large areas (Peña et al. 2014). During the past two decades, remote sensing methods have been developed for discriminating crop types using different types of remotely sensed data (Mingwei et al. 2008). This includes radio detection and ranging (RADAR) data, which is beneficial because of its ability to penetrate clouds, thus eliminating the problem of cloud-contamination (Forkuor et al. 2014; Jiao et al. 2014; Joshi et al. 2016). However, RADAR data has been shown to have issues with low-resolutions and high levels of noise and is expensive (LaDue, Heinselman & Newman 2010; Grandoni 2018; You, Jianjuan & Xin 2016). Hyperspectral imagery has also been used for crop discrimination but is often unavailable or prohibitively expensive to acquire (Delegido et al. 2010; Thenkabail et al. 2013). Limitations associated with RADAR and hyperspectral data led to the adoption of low spatial but high temporal resolution multispectral data, with MODIS and AVHRR being the most exploited datasets for crop type classifications (Mingwei et al. 2008; Liu, Ozdogan & Zhu 2013; Hao et al. 2015; Zheng et al. 2015).

Liu, Ozdogan & Zhu (2013) argued that the ability of remote sensors to acquire multiple images during a growing season is the main reason data provided by optical sensors has become the most popular data for crop type differentiation (Conrad et al. 2010; Foerster et al. 2012; Long et al. 2013; Siachalou, Mallinis & Tsakiri-Strati 2015). For many years, multi-temporal methods for

crop type mapping relied on satellite sensors with high temporal but low spatial resolutions (Mingwei et al. 2008; Lunetta et al. 2010; Gumma et al. 2011; Bolton & Friedl 2013). For example, Wu et al. (2014) used multisensory data with medium to low spatial resolutions to monitor crop production globally (known as the CropWatch system) and reported such data to be effective for monitoring global crop production. Using MODIS-NDVI data, Mingwei et al. (2008) used the Fourier analysis method to discriminate between crops on a regional scale and reported the multi-temporal approach useful for this application. However, low-resolution satellite sensors such as MODIS have limited ability to provide detailed (i.e. field-level) crop type information. According to Gilbertson, Kemp & Van Niekerk (2017), imagery with medium to high spatial resolutions is needed for the successful discrimination of different crops grown on neighbouring fields, and recent studies have shown that high spatial and temporal resolution data is critical for producing timely and accurate crop type maps (Inglada et al. 2016).

The recent launch of the Sentinel-2 satellite, which offers 10 m resolution imagery at five-day intervals, represents a substantial technological advancement and provides many opportunities for generating more accurate, up-to-date and detailed crop type maps. Immitzer, Vuolo & Atzberger (2016) investigated the appropriateness of pre-operational single-date Sentinel-2 data for mapping crop types and tree species. They recorded cross-validated accuracies ranging between 65% and 76% for tree species and crop types respectively but concluded that the full potential of Sentinel-2 data could not be assessed with a single-date acquisition. They postulated that multi-temporal Sentinel-2 data would likely significantly improve classification accuracies. The combination of high spatial resolution, novel spectral capabilities (including three bands in the red-edge and two bands in the shortwave infrared regions) and high temporal resolution provides a dataset of unprecedented richness from which crop type differentiations can be made.

Using simulated Sentinel-2 data, Inglada et al. (2016) reviewed a range of methods for crop type mapping and concluded that the imagery closes the gap between the availability of timely and accurate crop type maps and users' needs. Lebourgeois et al. (2017) used the same data for mapping smallholder agriculture in a tropical region characterised by high intra- and inter-field spatial variability. They found that it is effective for mapping crops on smallholder farms and attributed its success to the imagery's relatively high spatial resolution. In addition, Sentinel-2 imagery's novel spectral bands, as well as its temporal, textural and contextual features for capturing the variations in crop growth stages, crop patterns and field sizes, make it an ideal resource for crop type classifications (Peña et al. 2014).

There is general agreement that multi-temporal data is important for crop type classification. Sabour, Lohmann & Soergel (2008) argued that the selection of the most useful images from a

time-series is beneficial and generally gives more accurate results than when using all available images. This is supported by several studies which demonstrated that images acquired during peak growth stages are more useful than those acquired during low growth periods (Sabour, Lohmann & Soergel 2008; Long et al. 2013; Peña et al. 2014). This was attributed to the observation that some crops might be spectrally similar or constitute high levels of soil interference due to a lack of growth during certain stages in the growing season (Sabour, Lohmann & Soergel 2008; Veloso et al. 2017). According to Inglada et al. (2015), the selection of optimal dates for mapping crop types is axiomatically important but not always possible, especially in operational crop type data production workflows in which the hand-selection of images is not feasible. Hao et al. (2015) found that five images selected from a crop calendar are sufficient for effective crop classification. However, the selection of images based on crop calendars is greatly dependent on the availability of images and is prone to fail when images are not available during the key developmental stages of the target crops. According to Blaes, Vanhalle & Defourny (2005), temporal gaps in the growing season result in significant drops in classification accuracies when even a single image is missing at a key period.

Classification algorithms can also influence the success of crop type mapping (Myburgh & Van Niekerk 2013). Gilbertson, Kemp & Van Niekerk (2017) found the ability of non-parametric machine learning algorithms to use known data for classifying large sets of imagery, while incorporating ancillary spatial data, to be ideal for crop type classifications. Popular machine learning algorithms include SVM, DT, k-NN and RF. SVM is a good choice for vegetation classification applications, since it can handle high-dimensional data and perform well, even with few training samples (Myburgh & Van Niekerk 2013; Peña et al. 2014; Ozdarici-Ok, Ok & Schindler 2015; Gilbertson, Kemp & Van Niekerk 2017). One of the advantages of RF is its ability to perform well even with incomplete (noisy) data or when data with high levels of redundancy is used as input. DTs, k-NN and ML have been highly successful in a range of remote sensing applications, including land cover mapping and crop type mapping (Myint et al. 2011; Myburgh & Van Niekerk 2013).

The availability of crop type information early in the growing season (before harvest) is critical for many applications, but in most cases such data only becomes available post-harvest. This study assesses the performance of several machine learning classifiers when applied to pre-harvest images. Sentinel-2 imagery was used to generate a large set of features (predictor variables) – inclusive of spectral bands, vegetation indices, principal components and texture measures – which was used as input for five different classifiers. The classifiers were trained and validated using in situ data. The experiments were carried out in two sites, located approximately 310 km from each

other, to assess the consistency of the results. The results were interpreted in the context of finding an operational solution for classifying crop types at regional scales.

3.3 MATERIALS AND METHODS

3.3.1 Study sites

This study was conducted in two sites (covered by Sentinel-2 tiles T34HJB and T34HEH) in the Western Cape Province of South Africa. For the purpose of this study, T34HJB and T34HEH will be referred to as Study Sites A and B respectively (Figure 3.1). Site A is located about 50 km north of Cape Town, while Site B is located east of the Langeberg mountain range and south of the Swartberg mountain range. Both sites have a Mediterranean climate and are as such characterised by warm, dry summers and cool, wet winters (Malan 2016). Site A has an average annual rainfall of 550 mm, with an average minimum temperature of 11°C and an average maximum temperature of 22º C (Tererai et al. 2015). Site B has an average rainfall of 800 mm, with an average minimum temperature of 7ºC and an average maximum temperature of 22ºC (Malan 2016). These sites were chosen owing to the diversity of annual winter crops cultivated and the availability of crop census data. The most common crops cultivated in both sites are wheat, lucerne, planted pasture and canola. Canola, wheat and planted pastures are grown during winter, while lucerne is harvested throughout the year.

3.3.2 Satellite imagery acquisition and preparation

A selection of cloud-free Sentinel-2 images, pre-processed at Level 1C and captured between April 2016 and January 2017, was sourced from the Sentinel Hub (https://www.sentinel-hub.com/). The temporal period was chosen to represent a typical winter growing season. Data preparation involved resampling and stacking the 20 m spectral bands to 10 m (Immitzer, Vuolo & Atzberger 2016). Table 3.1 and Table 3.2 presents the images used in both sites, the respective crop stages, and the number of weeks before harvest that each image represents.

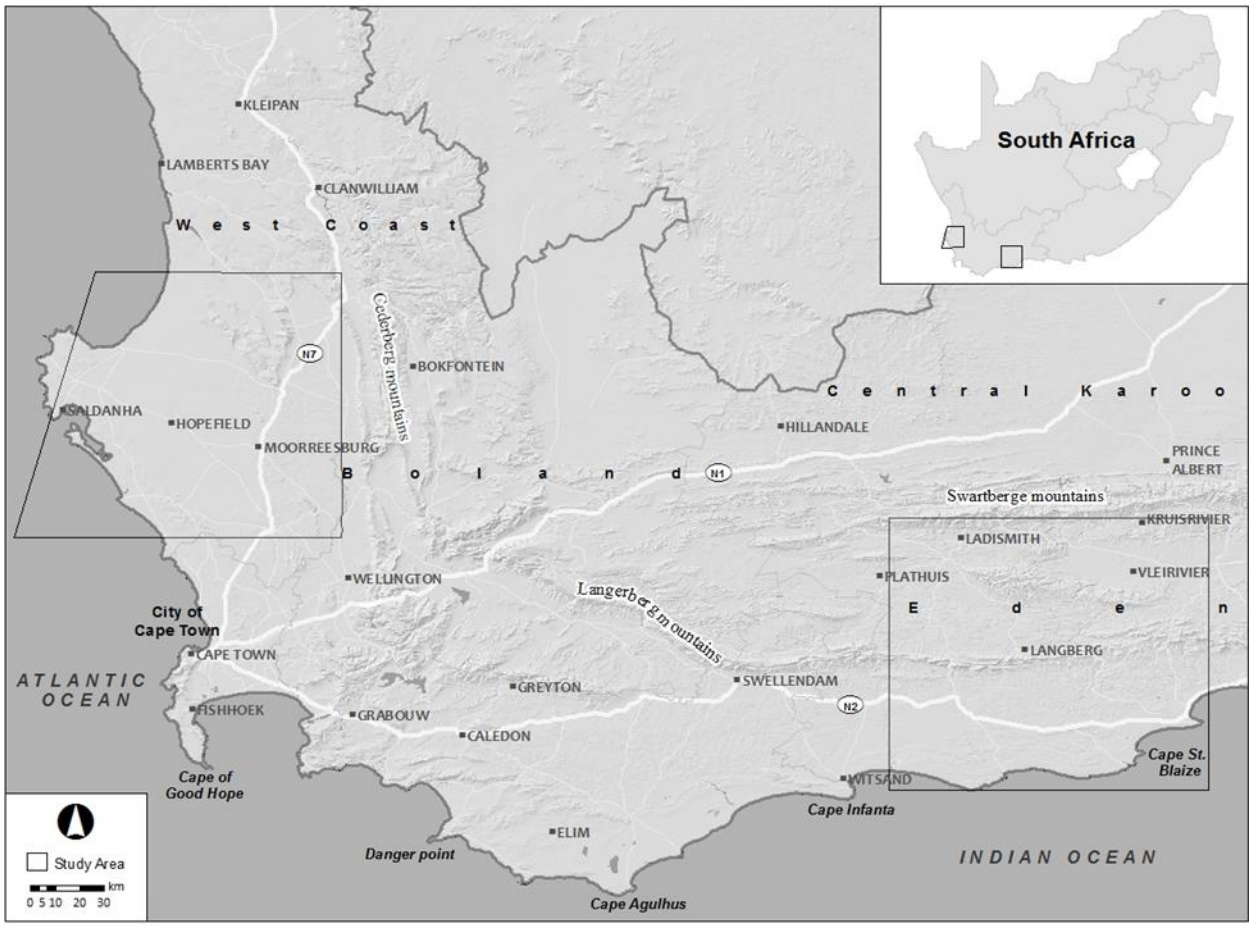

Figure 3.1 Location of the study sites in the Western Cape, South Africa

Table 3.1 Images collected, crop calendars and the approximate number of days before harvest in Study Site A

#	Acquisition date	Canola		Lucerne		Pasture		Wheat	
		Calendar	Weeks before harvest	Calendar	Days before harvest	Calendar	Days before harvest	Calendar	Weeks before harvest
1	6 Apr 2016	Sowing	25	Multiple cutting options Stages may vary		Sowing			14
2	26 Apr 2016	Sowing	22			Sowing		Sowing	11
3	16 May 2016	Sowing	19			Sowing		Sowing	8
4	6 June 2016	Sowing	16			Possible summer senescence			5
5	4 Aug 2016		8					Harvest	0
6	3 Sept 2016		3					Harvest	0
7	3 Oct 2016	Harvest	0					Harvest	0
8	13 Oct 2016	Harvest	0					Harvest	0
9	23 Oct 2016	Harvest	0					Harvest	0
10	31 Jan 2017	Post-harvest	Post-harvest					Post-harvest	Post-harvest

Table 3.2 Images collected, crop calendars and the approximate number of days before harvest in Study Site B

#	Acquisition Date	Canola		Lucerne		Pasture		Wheat	
		Calendar	Weeks before harvest	Calendar	Days before harvest	Calendar	Days before harvest	Calendar	Weeks before harvest
1	3 Apr 2016	Sowing	25	Multiple cutting options Stages may vary		Sowing		Sowing	19
2	22 June 2016	Sowing	14			Sowing			12
3	2 July 2016		12			Sowing			11
4	1 Aug 2016		8			Possible summer senescence			7
5	11 Aug 2016		7						5
6	21 Aug 2016		5						4
7	20 Oct 2016	Harvest	0					Harvest	0
8	29 Dec 2016	Post-harvest	Post-harvest					Post-harvest	Post-harvest
9	8 Jan 2017	Post-harvest	Post-harvest					Post-harvest	Post-harvest
10	18 Jan 2017	Post-harvest	Post-harvest					Post-harvest	Post-harvest

3.3.3 In situ data collection and field delimitation

A crop type and field boundary dataset containing polygons of agricultural fields was obtained from the Western Cape Department of Agriculture. These field boundaries were used as basic units for classification. Due to an insufficient number of samples for some classes, additional samples were collected by the visual interpretation of Sentinel-2 and high-resolution satellite imagery. The total number of samples for Site A and B was 640 and 418, respectively. The crop types and number of samples per class for the two study sites are given in Table 3.3.

Table 3.3 The number of samples per class in Study Sites A and B

Crop type	Number of samples	
	Study Site A	Study Site B
Canola	66	93
Lucerne	98	98
Pasture	167	87
Wheat	96	97
Fallow	213	43
Total	640	418

3.3.4 Feature set development

41 features (per image date) were generated from the Sentinel-2 bands (Table 3.4). For this study, only the blue (Band 2), green (Band 3), red (Band 4), vegetation red-edge (Band 5), vegetation red-edge (Band 6), vegetation red-edge (Band 7), NIR (Band 8), narrow NIR (Band 8A), SWIR (Band 11) and SWIR (Band 12) were used. The coastal aerosol (Band 1), water vapour (Band 9) and SWIR cirrus (Band 10) bands were deliberately excluded, as they were deemed unsuitable for crop type classification, as reported by Immitzer, Vuolo & Atzberger (2016) and Inglada et al. (2016). The generated features included 24 variations (Table A-1) of vegetation indices (VIs) derived from the equations in Table 3.4 (Immitzer, Vuolo & Atzberger 2016). Mean values for all spectral features were calculated for each agricultural field. Homogeneity, dissimilarity and entropy texture features, measuring pixel uniformity and disorder, were also calculated and included in the classifications (Peña-Barragán et al. 2011; Schmedtmann & Campagnolo 2015). A principal component analysis (PCA) was performed on all spectral bands per image date, and the first four principal components (PCs) were retained, as recommended by Gilbertson, Kemp & Van Niekerk (2017).

Table 3.4 Features used as input for classifications (refer to Table A-1 for the full names, formulae and bands used to compute each feature)

Variable source	Features
Spectral bands	blue, green, red, vegetation red-edge1, vegetation red-edge2, vegetation red-edge3, NIR, Narrow NIR, SWIR1, SWIR2
Vegetation indices	AFRI, EVI2, NDMI, NDVI, NDVI red-edge, AFRI red-edge, EVI2 red-edge
Textural features	dissimilarity, entropy, homogeneity
Image transformations	PC1, PC2, PC3, PC4

3.3.5 Experimental design

Four experiments were undertaken (Figure 3.2). The first experiment (Experiment 1) involved classification using available cloud-free images collected throughout the winter growing season, i.e. each classification was based on a single image (henceforth called uni-temporal). In the second experiment (Experiment 2), four different combinations of five uni-temporal images were used as input to the classifiers. The images were selected based on the overall accuracy (OA) rankings obtained from Experiment 1 (i.e. the five individual images that provided the highest uni-temporal OAs).

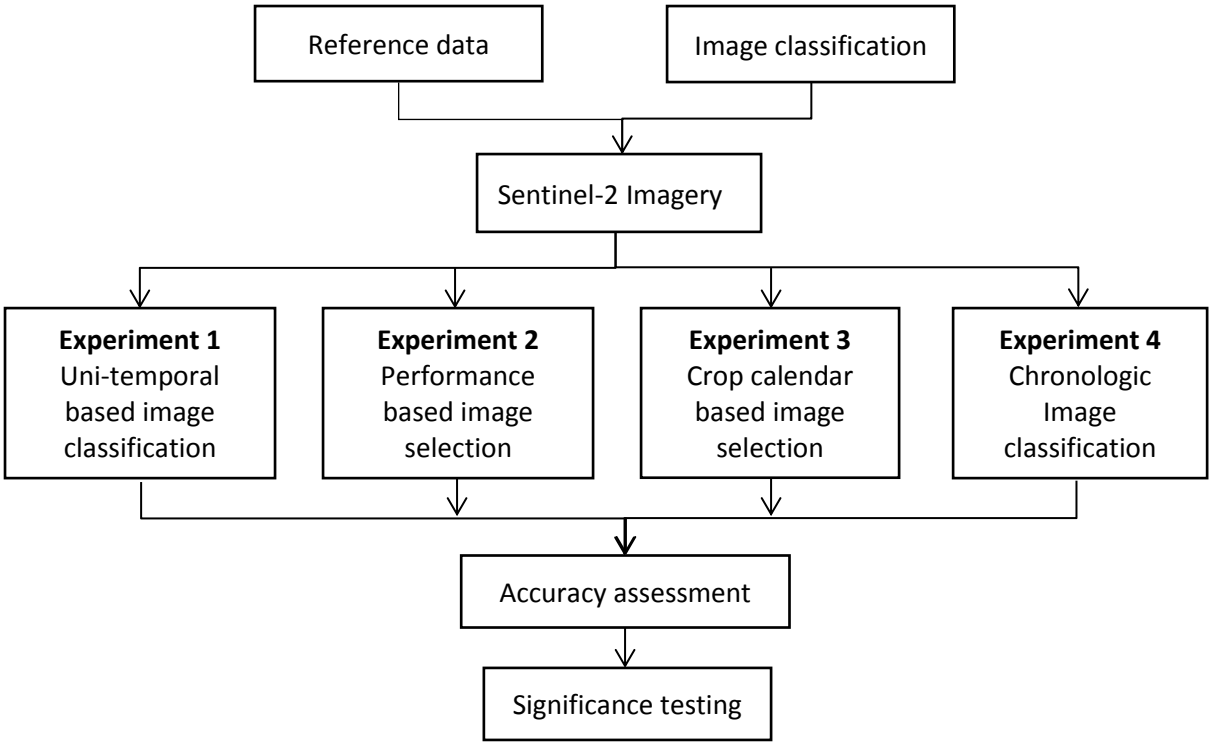

Figure 3.2 Experimental design

For Experiment 3, the following five image dates were handpicked and used for classification: 26 April, 6 June, 4 August, 3 September and 23 October for Site A; and 3 April, 22 June, 2 July, 11 August and 20 October for Site B. Figure 3.3 and Figure 3.4 show how these dates relate to the crop calendars for each site. The number of images chosen was based on findings by Hao et al. (2015) and Gilbertson, Kemp & Van Niekerk (2017).

The fourth experiment involved classification using all the available cloud-free images captured throughout the growing season. This experiment was executed by the chronological addition of images to the classifiers to assess how early in the season reasonable accuracies can be achieved.

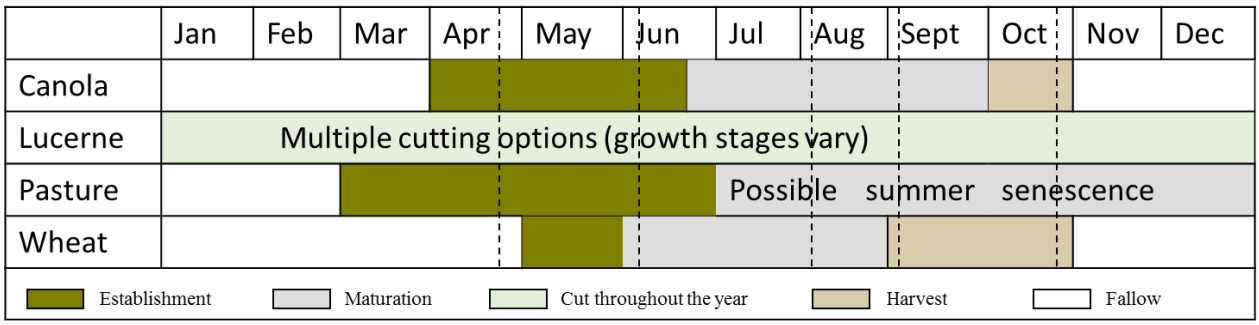

Figure 3.3 Phenological stages of targeted crops in Study Site A (the dotted lines represent the selected images)

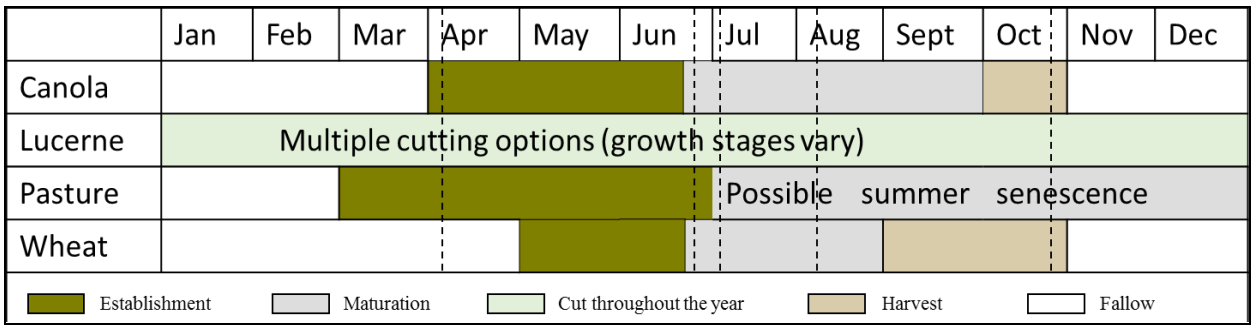

Figure 3.4 Phenological stages of targeted crops in Study Site B (the dotted lines represent selected images)

3.3.6 Classification and accuracy assessment

The supervised learning and image classification environment (SLICE) software, developed by the Centre for Geographical Analysis (CGA) at Stellenbosch University, was used for classification and accuracy assessment (Myburgh & Van Niekerk 2013). SLICE includes several classification algorithms, namely: SVM, k-NN, DT, RF and ML. The ML and k-NN classifiers were implemented using the Open CV 2.2 libraries (Bradski 2000), with k = 1. Libsvm 3.0 was used to implement the SVM classifier (Chang 2011). The parameters for DT and RF were based on the guidelines provided in the Open CV library documentation. The geospatial data abstraction library (GDAL) was used to manipulate the raster files and shapefiles. (See Myburgh & Van Niekerk (2013) for an incisive description of how the various classifiers were configured.)

A 3:2 sample split ratio was employed for accuracy assessment. Forty percent of the samples was randomly selected and reserved for independent validation of the classifications. The same set of training and validation samples were maintained for all the experiments. SLICE automatically generates confusion matrices and calculates OAs and Kappa coefficients (Ks) for every classification (Gilbertson, Kemp & Van Niekerk 2017). OA is interpreted as the percentage of fields corresponding to the errors of omission and commission (Campbell & Wynne 2011), while K assesses the statistical differences between classifications (Foody & Atkinson 2002). McNemar's test, ANOVA and t-tests (as implemented in Microsoft Excel) were used for assessing the statistical significance of the accuracies obtained from the experiments, as recommended by Foody & Mathur (2004) and applied by Duro, Franklin & Dubé (2012) and Gilbertson, Kemp & Van Niekerk (2017). The alpha values for ANOVA and t-tests were set to 0.05, while the alpha value for McNemar's test was set to 1.96.

3.4 RESULTS

3.4.1 Experiment 1: Uni-temporal, individual images

Experiment 1 was undertaken with uni-temporal images collected between April 2016 and January 2017, thus covering a full winter growing season. Results for Experiment 1 are listed in Table 3.5. At Site A, the highest individual OA (80%) was achieved using SVM with an image acquired early in September (Image 6, approximately four weeks before harvest). This OA is only marginally higher than the second-highest OA (79.6%), also achieved with SVM ($p = -0.40$) using an image acquired in early August (Image 5, about eight weeks before harvest). The highest OAs achieved with SVM and RF (77.2%) are significantly different ($p > 3.10$) from those achieved with k-NN and DT. It is important to note that the number of weeks before harvest greatly depends on individual crop planting and harvest dates. For the sake of simplicity, the first harvest date is henceforth used as reference.

At Site A, the five images with the highest mean OAs were collected between June and October, with the image collected early in August (4 Aug) recording the highest mean OA (73.9%), followed by early September (3 Sept = 70.3%), mid-October (13 Oct = 60.7%), early October (3 Oct = 56.6%) and early June (6 Jun = 51.5%). The 4th of August image also returned a relatively low OA standard deviation (SD = 5.41%), indicating that it consistently produced good results across all classifiers. The differences in mean OAs between the images collected in August and those collected in September (maturation/harvesting stage, depending on the crop and the respective planting and harvest dates) are not statistically significant (two-tailed t-test $p = 0.387$). However, the difference in OAs between the August image and those collected at the beginning of the growing season (June) and after harvest (January) is statistically significant (two-tailed t-test $p < 0.0009$).

The highest individual OA (79.6%) for Site B (Table 3.5) was achieved in August using SVM (79.6%) (approximately eleven weeks before harvest). The second-highest OA (77.8%) was achieved in the second week of August with DT (roughly ten weeks before harvest). The difference in OA between these classifications was, however, statistically insignificant ($p < 1.09$). In contrast, the outputs of k-NN (67.6%) and ML (47.9%) were significantly ($p > 3$) lower than those achieved by SVM and RF. For Site B, the highest mean OA was recorded with images collected between July and October. Similar to Site A, the highest mean OA was recorded with an image collected early in August (1 Aug = 65.4%), followed by images collected mid-August (11 & 21 Aug = 63.5%), the beginning of July (2 Jul = 51.6%) and mid-October (20 Oct = 50.9%). The 21 Aug image returned a relatively low OA standard deviation (SD = 9.83%), indicating that it consistently produced good results across all classifiers. Comparable to Site A, there is a statistically significant

difference (two-tailed t-test $p < 0.0488$) in OAs achieved with the images collected in August (complete maturity), compared to those collected in June and January.

Table 3.5 Uni-temporal image classification overall accuracies (OAs %) and Kappa coefficients (Ks), as well as the average (AVG) and standard deviation (SD) of OAs and Ks, for all classifiers and image dates in Study Sites A & B

Site	Image	Date	SVM		K-NN		DT		RF		ML		AVG		SD	
			OA	K	OA	K	OA	K	OA	K	OA	K	OA	K	OA	K
A	1	6 Apr	46.6	0.29	42.7	0.24	40.7	0.22	50.9	0.34	42.7	0.24	44.7	0.26	4.06	0.04
	2	26 Apr	48.2	0.30	35.6	0.15	41.1	0.23	45.8	0.27	42.3	0.25	42.6	0.24	4.88	0.05
	3	16 May	52.1	0.36	42.3	0.25	40.7	0.22	53.7	0.39	47.0	0.31	47.1	0.30	5.75	0.07
	4	6 Jun	60.3	0.48	42.3	0.24	48.6	0.32	58.4	0.44	48.2	0.29	51.5	0.35	7.56	0.10
	5	4 Aug	79.6	0.73	70.1	0.61	66.6	0.56	77.2	0.70	76.4	0.69	73.9	0.65	5.41	0.07
	6	3 Sep	80.0	0.73	62.3	0.51	65.0	0.54	74.5	0.66	69.8	0.59	70.3	0.60	7.14	0.08
	7	3 Oct	74.9	0.67	55.6	0.55	51.7	0.37	67.4	0.57	33.7	0.23	56.6	0.47	15.8	0.17
	8	13 Oct	74.5	0.66	53.3	0.38	56.0	0.42	67.0	0.56	52.9	0.37	60.7	0.47	9.58	0.12
	9	23 Oct	70.1	0.60	54.9	0.40	51.7	0.37	68.6	0.58	48.2	0.31	58.7	0.45	10.0	0.13
	10	31 Jan	54.1	0.39	47.8	0.32	50.5	0.35	57.6	0.44	50.1	0.35	52.0	0.37	3.84	0.04
		AVG	64.0	0.52	50.6	0.36	51.2	0.36	62.1	0.49	51.1	0.36				
		SD	13.2	0.17	10.5	0.15	9.31	0.12	10.3	0.14	12.8	0.15				
B	1	3 Apr	45.5	0.30	34.1	0.16	41.9	0.26	50.2	0.36	20.3	0.00	38.4	0.21	11.7	0.14
	2	22 Jun	66.4	0.57	42.9	0.34	52.6	0.39	67.6	0.58	22.7	0.00	50.4	0.37	18.5	0.23
	3	2 Jul	70.0	0.61	50.2	0.37	54.4	0.42	63.4	0.53	20.3	0.00	51.6	0.38	19.1	0.23
	4	1 Aug	79.6	0.74	65.2	0.56	66.4	0.57	75.4	0.68	40.7	0.23	65.4	0.55	15.1	0.19
	5	11 Aug	73.6	0.66	67.6	0.58	77.8	0.71	76.6	0.70	20.3	0.00	63.5	0.53	24.2	0.30
	6	21 Aug	72.4	0.64	64.6	0.54	61.6	0.50	71.2	0.63	47.9	0.32	63.5	0.52	9.83	0.12
	7	20 Oct	63.4	0.53	55.1	0.42	51.4	0.38	61.6	0.50	23.3	0.04	50.9	0.37	16.2	0.19
	8	29 Dec	63.4	0.53	42.5	0.27	44.9	0.30	57.4	0.45	32.3	0.14	48.1	0.33	12.3	0.15
	9	8 Jan	58.6	0.46	44.3	0.28	48.5	0.35	58.6	0.46	43.7	0.28	50.7	0.36	7.40	0.09
	10	18 Jan	59.2	0.47	53.2	0.40	43.7	0.28	59.2	0.47	42.5	0.27	51.5	0.37	8.11	0.09
		AVG	65.2	0.55	51.9	0.39	54.3	0.41	64.1	0.53	20.3	0.00				
		SD	9.59	0.12	11.2	0.13	11.3	0.14	8.47	0.10	11.2	0.13				

With regards to the overall performance of the classifiers, SVM yielded the highest mean OA (64%), followed by RF (62.1%), DT (51.2%), k-NN (51.1%) and ML (50.6%) in Site A. Both

SVM and RF performed significantly better than k-NN, DT and ML (two-tailed: t-test $p < 0.039$). Similarly, SVM yielded the highest mean OA (65.2%) in Site B, followed by RF (64.1%), DT (54.1%), k-NN (51.9%) and ML (20.3%). Again, SVM and RF performed significantly better than k-NN, DT and ML (two-tailed: t-test $p < 0.032$). In Site A, SVM was the least stable classifier (OA SD = 13.2%), while it generated accuracies that were the second most stable (OA SD = 9.59%) in Site B. RF produced consistently good results (OA SDs of 10.3% and 8.47% in sites A and B respectively). Overall, for Experiment 1 (uni-temporal images), OAs increased from the beginning of the growing season and peaked around August and/or September. The OAs then dropped at the start of harvest.

3.4.2 Experiment 2: Multi-temporal, rank-based image set

This experiment was conducted using combinations of five images, selected based on the performance of individual images (from Experiment 1). Four different combinations of these images were tested and the results are presented in Table 3.6. The highest individual OA (82.4%) in Site A was achieved using SVM on a combination of the two images with the highest ranking (4 Aug & 3 Sept). However, this was only marginally (2.2%) and insignificantly ($p = -1.34$) higher than when SVM was applied to a combination of three images (4 Aug, 3 Sept & 13 Oct). When the mean OAs of all classifiers are considered, the combination of the 4 Aug & 3 Sept images yielded a mean OA of 70.4%, which was slightly lower than when only the 4 Aug image was used as input (OA of 73.9%).

The highest individual OA (79.6%) for Site B was achieved using the single image with the highest rank (1 Aug) as input to SVM (Table 3.6). However, this is only marginally (0.6%) and insignificantly (p-value of 0.25) higher than when SVM was applied to a combination of three images (1, 11 & 21 August). The combination of the two highest-ranked individual images (1 August & 11 August) yielded the highest mean OA (72.1%), but this was not significantly higher (two-tailed t-test $p = 0.757$) than the second-highest mean OA (70.8%) achieved when all five images were used as input. Overall, the mean OA declines with an increase in the number of images in Site A, while the opposite is observed in Site B. These results confirm those of Experiment 1 in that the highest OAs are achievable with combinations of images collected between August and September. This finding applies to both sites.

Overall, SVM achieved superior results across all image combinations, with a mean OA of 80% in Site A. Although there is no statistically significant difference between SVM, RF, k-NN and DT (two-tailed t-test $p < 0.174$), the difference between SVM and ML is statistically significant (two-tailed t-test $p = 0.003$). A similar pattern is seen in the results of Site B – there is no statistically significant difference in the performance of SVM, RF, k-NN and DT, but SVM

performed significantly better than ML (two-tailed t-test p = 0.0003). From the standard deviations, it is evident that SVM, RF, k-NN and DT were more stable (SD < 2.5) in both sites, while ML displayed some instability (see Table 3.6).

Table 3.6 OAs and Kappa coefficients for rank-based image combinations, OAs obtained with all the images available for the season (All) and the average (AVG) for classifiers and image combinations in Study Sites A & B

Site	# image	Dates	SVM		K-NN		DT		RF		ML		AVG		SD	
			OA	K	OA	K	OA	K	OA	K	OA	K	OA	K	OA	K
A	Best	4 Aug	79.6	0.73	70.1	0.61	66.6	0.56	77.2	0.70	76.4	0.69	73.9	0.65	5.41	0.07
	2 Best	4 Aug & 3 Sep	82.4	0.76	70.6	0.62	72.0	0.63	77.8	0.71	49.2	0.36	70.4	0.62	12.7	0.15
	3 Best	4 Aug, 3 Sep, 13 Oct	80.2	0.74	69.6	0.58	69.6	0.59	79.0	0.73	49.2	0.36	69.5	0.60	12.4	0.15
	4 Best	4 Aug, 3 Sep, 3 & 13 Oct	79.3	0.73	72.5	0.65	67.5	0.58	80.2	0.74	38.6	0.26	67.6	0.59	17.0	0.19
	5 Best	4 Aug, 3 Sep, 3, 13 & 23 Oct	78.4	0.72	74.3	0.68	70.4	0.60	79.3	0.73	35.8	0.18	67.6	0.58	18.1	0.23
	All		81.1	0.75	69.8	0.60	67.4	0.57	80.3	0.74	32.5	0.03	66.2	0.53	19.8	0.29
	AVG		80.0	0.74	71.2	0.62	69.2	0.59	78.7	0.72	49.8	0.37				
	SD		1.50	0.01	1.94	0.03	2.18	0.02	1.20	0.01	16.0	0.19				
B	Best	1 Aug	79.6	0.74	65.2	0.56	66.4	0.57	75.4	0.68	40.7	0.23	65.4	0.55	15.1	0.19
	2 Best	1 & 11 Aug	78.4	0.72	68.2	0.59	71.2	0.63	77.2	0.70	65.8	0.55	72.1	0.64	5.50	0.07
	3 Best	1, 11 & 21Aug	79.0	0.73	67.6	0.58	69.4	0.61	78.4	0.72	58.6	0.46	70.6	0.62	8.45	0.11
	4 Best	1, 11 & 21 Aug & 2 Jul	79.0	0.73	69.4	0.61	68.8	0.60	79.0	0.73	54.4	0.41	70.9	0.61	10.0	0.13
	5 Best	1, 11, 21 Aug, 2 Jul & 20 Oct	78.4	0.72	65.8	0.56	71.8	0.64	77.2	0.71	61.0	0.49	70.8	0.62	7.42	0.09
	All		80.8	0.75	66.4	0.57	71.8	0.64	76.0	0.69	62.8	0.52	71.5	0.63	7.21	0.09
	AVG		78.9	0.73	67.2	0.58	69.5	0.61	77.4	0.70	56.1	0.42				
	SD		0.50	0.00	1.72	0.02	2.13	0.02	1.38	0.01	9.54	0.12				

3.4.3 Experiment 3: Multi-temporal, hand-selected image set

Experiment 3 was undertaken using five images which were hand-selected on the basis of the critical developmental stages in the growing cycle of crops, as demonstrated in Gilbertson, Kemp & Van Niekerk (2017). Results are presented in Table 3.7. The highest individual OA (81.5%) in Site A was achieved with RF, which is marginally higher than the second-highest OA achieved with SVM (79.6%). Overall, DT and ML achieved the lowest OA, with ML being the worst

performing classifier (28.2%), which was found to be significantly lower (p = 11.1) than the OA achieved with RF (81.5%). Overall, this experiment achieved a mean OA of 67.0%, which is not significantly different (two-tailed t-test; p = 0.515) from the mean OA achieved with the highest mean OA (73.9%) obtained with Experiment 2 (Table 3.6) in Site A (although a 5% difference would be regarded as significant by many analysts).

Table 3.7 OA and Kappa coefficients and the average (AVG) for the five images selected based on the crop development stages for Study Sites A & B (refer to Figure 2.2 for respective crop development stages corresponding to the selected images)

Site	# image	Image dates	SVM		K-NN		DT		RF		ML		AVG		SD	
			OA	K	OA	K	OA	K	OA	K	OA	K	OA	K	OA	K
A	Five	26 Apr, 6 Jun, 4 Aug, 3 Sept & 23 Oct	79.6	0.73	76.8	0.69	69.0	0.59	81.5	0.75	28.2	0.13	67.0	0.57	22.2	0.25
B	Five	3 Apr, 22 Jun, 11 & 21 Aug & 20 Oct	80.2	0.74	65.2	0.55	73.6	0.66	77.2	0.70	64.6	0.54	72.1	0.63	7.03	0.08

With regard to Site B, the highest OA was achieved with SVM (80.2%), followed by RF (77.2%) (Table 3.7). The difference between the classifiers with the highest and second-highest OAs was found to be statistically insignificant (p = 1.14). K-NN and ML achieved the lowest OA. Overall, this experiment achieved a mean OA of 72.1%, which is identical to the highest mean OA obtained with Experiment 2 (Table 3.6) in Site B. Similar to Experiment 1 & 2, the highest OAs for both sites were based on both SVM and RF.

3.4.4 Experiment 4: Chronologic image addition

Experiment 4 was conducted by chronologically adding images from the beginning to the end of the growing season. At Site A (Table 3.8), SVM and RF were able to achieve accuracies of more than 75% (SVM = 79.6%; RF = 78%) by the first week of August (about eight weeks before harvest). The highest individual OA for this site (83.1%) was achieved when all images up to 13 October (approximately one week after harvest started) were used as input to RF. A slightly lower OA (81.1%) was achieved when all images up to January were used with SVM. Overall, the highest mean OA (66.6%) for Site A was obtained when the image collected in the first week of September (Image 6) was added to the classification. This mean OA is slightly higher than what was obtained with the entire time-series (66.2%) but is not significant (two-tailed: t-test p = 0.97). For Experiment 4, RF generally outperformed the other classifiers, with a mean OA of 70.5% for all scenarios, followed by SVM (69.2%), k-NN (60.3%), DT (58.7%) and ML (30.6%).

The results for the entire time-series were slightly better than when the pre-harvest images were used, but the differences in OAs are statistically insignificant across all classifiers (two-tailed: t-test $p > 0.321$). Generally, RF and SVM outperformed the other classifiers and there is no statistical significance between the SVM and RF results (two-tailed: t-test $p > 0.864$). There is, however, a statistically significant difference in the OAs of both RF and SVM in comparison to k-NN, DT and ML (two-tailed: t-test $p < 0.04$). All classifiers displayed some instability across the different growth stages (SD > 11), except for ML which consistently produced low OAs.

Similar to Site A, SVM and RF achieved OAs of more than 75% (SVM = 77.2%; RF = 77.8%) in Site B (Table 3.8), when images up to the beginning of August (approximately eleven weeks before harvest) were used as input. The difference between these results was statistically insignificant ($p = 0.22$). The highest individual classification result (82%) was achieved when all images up to the image collected in the second week of August (11 August) was used as input to RF. This is only marginally higher than the highest individual OA (80.5%) obtained when the entire time-series was used with SVM. Although there is no statistically significant difference between the highest individual OAs obtained when using images collected pre-harvest only and when the entire time-series is used in both Sites A & B ($p < 0.5$), there is a notable difference, with pre-harvest images achieving a slightly higher (1.5%) OA. In Site B, the highest mean OA (73.2%) was achieved with all images up to the image collected in the third week of August (21 August: Image 6), which is approximately four weeks before harvest. This is slightly higher than the mean OA achieved when using the entire time-series (71.5%). Similar to Site A, the difference in these OAs is not statistically significant (two-tailed: t-test $p = 0.793$).

Concerning classifiers, RF recorded the highest mean OA (73.4%), followed by SVM (72%), when only pre-harvest images were used. The two classifiers performed on par when the entire time-series was used as input (72.7%). Although there is no significant difference between the performance of SVM and RF, they both achieved significantly higher OAs than those of k-NN and ML (two-tailed: t-test $p > 0.1$) in both sites. Overall, all classifiers achieved slightly higher results in Site A when the entire time-series was used, compared to when only pre-harvest images were used. No clear trend could be established regarding the difference in OA between pre-harvest and the entire time-series for the various classifiers in Site B

Table 3.8 OAs and Kappa coefficients, as well as the average (AVG) and standard deviation (SD) of OAs and Ks, for all classifiers and image dates in Study Sites A & B for the incremental classifications in Sites A and B

Site	Image	Dates	SVM		K-NN		DT		RF		ML		Mean		SD	
			OA	K	OA	K	OA	K	OA	K	OA	K	OA	K	OA	K
A	1 – 2	6 Apr – 26 Apr	51.7	0.35	44.3	0.27	41.5	0.24	54.5	0.39	26.6	0.12	43.7	0.30	10.9	0.10
	1 – 3	6 Apr – 16 May	56.0	0.42	50.5	0.36	46.2	0.30	57.6	0.44	22.7	0.10	46.6	0.32	14.1	0.13
	1 – 4	6 Apr – 6 Jun	61.5	0.49	57.2	0.44	49.0	0.33	63.1	0.51	27.4	0.10	51.6	0.35	14.6	0.16
	1 – 5	6 Apr – 4 Aug	79.6	0.73	63.1	0.51	70.1	0.61	78.0	0.71	21.5	0.06	62.6	0.52	23.8	0.27
	1 – 6	6 Apr – 3 Sept	80.3	0.74	68.2	0.58	70.1	0.61	79.6	0.73	34.9	0.05	66.6	0.54	18.5	0.28
	1 – 7	6 Apr – 3 Oct	79.2	0.72	69.0	0.59	69.4	0.60	79.6	0.73	33.3	0.02	66.1	0.53	19.0	0.29
	1 – 8	6 Apr – 13 Oct	78.0	0.71	69.4	0.60	66.6	0.56	83.1	0.78	32.5	0.13	65.9	0.55	19.8	0.25
	1 – 9	6 Apr – 23 Oct	78.8	0.72	69.0	0.59	66.6	0.56	78.8	0.72	32.5	0.13	65.4	0.54	19.0	0.24
	All	6 Apr – 31 Jan	81.1	0.75	69.8	0.60	67.4	0.57	80.3	0.74	32.5	0.03	66.2	0.53	19.8	0.29
		AVG	69.2	0.59	60.3	0.47	58.7	0.46	70.5	0.60	30.6	0.08				
		SD	11.8	0.15	9.49	0.12	11.6	0.15	11.0	0.14	4.91	0.04				
B	1 – 2	3 Apr – 22 Jun	56.8	0.45	52.0	0.39	54.4	0.42	62.2	0.52	55.0	0.41	56.0	0.43	3.82	0.05
	1 – 3	3 Apr – 2 Jul	68.8	0.60	55.6	0.44	50.2	0.36	67.6	0.58	47.9	0.32	58.0	0.46	9.71	0.12
	1 – 4	3 Apr – 1 Aug	77.2	0.70	65.2	0.56	74.2	0.67	77.8	0.71	55.0	0.41	69.8	0.61	9.72	0.12
	1 – 5	3 Apr – 11 Aug	79.0	0.73	67.6	0.59	74.2	0.67	82.0	0.77	59.8	0.48	72.5	0.64	8.95	0.11
	1 – 6	3 Apr – 21 Aug	78.4	0.72	70.6	0.62	71.8	0.64	77.8	0.71	67.6	0.58	73.2	0.65	4.69	0.05
	1 – 7	3 Apr – 20 Oct	80.2	0.74	68.8	0.60	72.4	0.64	78.4	0.72	64.0	0.53	72.7	0.64	6.70	0.08
	1 – 8	3 Apr – 29 Dec	80.2	0.74	71.2	0.63	72.4	0.65	76.6	0.70	65.2	0.55	73.2	0.65	5.68	0.07
	1 – 9	3 Apr – 8 Jan	80.8	0.75	68.2	0.59	71.8	0.64	78.4	0.72	64.0	0.53	72.6	0.64	6.97	0.09
	All	3 Apr – 18 Jan	80.5	0.75	66.4	0.57	71.8	0.64	76.0	0.69	62.8	0.52	71.5	0.63	7.12	0.09
		AVG	72.7	0.64	61.9	0.51	65.5	0.55	72.7	0.64	72.1	0.43				
		SD	8.02	0.10	6.71	0.08	9.08	0.11	6.22	0.07	6.33	0.08				

In comparison to Experiment 2, Experiment 4 achieved significantly lower results (two-tailed t-test $p = 0.014$) in Site A, while Experiment 4 achieved a slightly higher OA in Site B (although the difference is statistically insignificant; $p = 0.587$). Table 3.9 summarises the overall results per experiment (using only the best results in each experiment). Compared to Experiment 3, Experiment 4 achieved slightly lower OAs in Site A, while achieving slightly higher OAs in Site B. When both sites are considered in combination, Experiment 4 (pre-harvest images)

outperformed the other experiments (average OA of 81.1%), but this is only marginally higher than the 81% OA achieved in Experiment 2 and 80.9% and 80.8% attained in Experiment 4 (all) and Experiment 3 respectively.

Table 3.9 Summary of the highest OAs achieved across all experiments in Sites A & B

Experiment	Site A Best OAs	Site B Best OAs	AVG Best OAs
1	80.0	79.6	79.8
2	82.4	79.6	81.0
3	81.5	80.2	80.8
4 (pre-harvest)	80.3	82.0	81.1
4 (all)	81.1	80.8	80.9
AVG Best OAs	81.4	80.4	80.7

With regard to the best period for identifying crop types, it is evident that crops can be classified with good OAs at the beginning of August, which marks the complete maturation stage for most crops. Based on the confusion matrices of the best classification results obtained within the August/September period across all experiments, SVM and RF were able to classify canola and fallow fields with producer's accuracies (PAs) exceeding 90% in both sites. The only exception was in Experiment 1 (87% for canola). Planted pasture was the most confused class in Site A (PA of below 60%), while lucerne was the most confused in Site B (PA of below 55%). Wheat returned OAs of above 70% with SVM and RF across all experiments during the August/September period.

3.5 DISCUSSION

From the results, it is noticeable that rank-based selection (Experiment 2) and pre-harvest images (Experiment 4, pre-harvest) outperformed the other experiments (Table 3.9). However, based on the marginal differences in accuracies among the experiments, it is questionable whether selecting images based on individual performance is worth the effort (and expense) of carrying out multiple uni-temporal classifications, especially given that handpicking images based on critical crop developmental stages (Experiment 3) produced similar results. This finding is in agreement with Peña et al. (2014); Asgarian, Soffianian & Pourmanafi (2016) and Gilbertson, Kemp & Van Niekerk (2017) who reported that the selection of images at important crop developmental stages is an effective strategy to improve crop type classification accuracies. The results of Experiments 3 and 4 are in agreement with Lussem, Hüttish & Waldhoff (2016) who found that the addition of "good" images (images that produced high OAs) to "bad" images (images that produced low OAs) does not compensate for errors caused by the latter. The statistical insignificance in the differences

in OAs achieved across all experiments is in agreement with Hao et al. (2015), who assessed the influence of time-series length on classification accuracies and found that the addition of more than five images did not have any significant impact on classification accuracies.

Although it was not possible to clearly establish trends in Experiments 2 and 3 (image selection), it is clear from Experiment 1 and 4 that the OAs of images acquired at the beginning of the season are low (mean OA < 55%), peak around Aug/Sept (mean OA > 65%) and then decline towards the end of the season (mean OA < 55%). Thus, images collected during the maturation period (August/September) yielded significantly higher classification accuracies when compared to those acquired during the early stages of development (April/June) and after harvest (post-October). Low OAs are expected at the beginning of the season (January–April) due to a lack of growth in most fields, making the soil background the main scattering contributor to the reflected signal and maximising soil interference with the spectral reflectance of the crops in focus. This is supported by the low classification accuracies obtained in Experiment 1, when images collected between April and early June (pre-maturation) and after December (post-harvest) were used. Furthermore, similarities in spectral responses of crops in their early stages of development have also been reported to have a negative effect on classification accuracies (Azar et al. 2016; Hao et al. 2018). For example, the separation of crops such as lucerne and planted pastures are expected to be the most challenging because of their spectral similarities, especially at the beginning of the growing season. This is confirmed by the confusion matrices, which show that most confusion occurred between these two classes.

As the crops reach maturation (late July–late September), they develop more distinguishing properties, providing classifiers with more information for differentiation. For example, crops such as canola turn bright yellow during maturation (flowering), making the crop easy to distinguish from other crops. Wheat was also well differentiated, likely due to the absence of other cereals such as barley and oats in the study sites (the classes most commonly confused with wheat) (Veloso et al. 2017). The confusion between planted pastures and lucerne persisted throughout the maturation stage, suggesting that these two classes do not have sufficient differentiating attributes. Fallow fields were best differentiated when the cultivated crops reached maturation (Aug/Sept), which was expected, given that the biomass difference between cultivated and uncultivated fields (bare soil interspersed with weed growth) is most dramatic at this stage.

Although OAs peaked throughout the maturation stage (until the end of September), a decline in OA is observed at the beginning of harvest (start of October) (Table 3.5). This decline in OA at the start of harvest is likely caused by the sudden removal of biomass and variation in harvest dates. This is supported by the increase in confusion among cultivated and fallow fields (see Table

A-1 − Table A-9). This finding is in agreement with Veloso et al. (2017), who found that crops are mostly misclassified in their early stages of development, with accuracies peaking as the vegetation cover increases and crops mature, then declining again at the beginning of harvest. Also, temporal gaps (missing images at important developmental stages) have been cited as one of the primary causes of reduced classification accuracies in multi-temporal crop type mapping studies (Inglada et al. 2015). Blaes, Vanhalle & Defourny (2005) reported significant drops in classification accuracies when even a single optical image was unavailable at a key period within the growing season.

Additionally, the value of including images collected post-harvest was measured in Experiments 1 and 4. The accuracies were generally low (< 65%) when the post-harvest (January) images were used as input to the uni-temporal classifications (Experiment 1). Fields are generally left fallow after harvest and are thus spectrally similar. Images collected after harvest are unlikely to have any positive effect on crop classification accuracies. This is supported by slightly higher accuracies achieved in Experiment 2, which did not include images from this period.

With regard to classifier performance, SVM and RF achieved significantly higher OAs compared to the other classifiers and were able to achieve relatively good results by August/September (approximately eight weeks before harvest when the image captured early in August is used; the period will vary depending on planting and harvesting dates of different crops). The highest individual accuracy (83.1%) was achieved with RF when all images up to mid-October were used. The strength of RF over the other classifiers, especially with the addition of the eighth image (Experiment 4) can be attributed to the classifier's ability to handle highly dimensional data without deletion. This is supported by the classifier's ability to perform well (mean OA = 80.3%) when all images were used as input (410 variables). This is comparable to the findings of Gilbertson, Kemp & Van Niekerk (2017), who compared feature sets with different sizes to assess the impact of dimensionality reduction on crop type classification accuracies and found both SVM and RF to produce high accuracies (> 85%) when all features (205) were used as input. This is also in agreement with Rodriguez-Galiano et al. (2012) who used RF to classify Mediterranean land cover with multi-temporal imagery and multi-seasonal texture measures – 972 input variables in total – and found RF to be able to handle the high-dimensional data well.

The strong performance of SVM corresponds to the findings of Myburgh & Van Niekerk (2013). While differences within crop fields (e.g. crop conditions), differences in developmental stages, etc. have been shown to have a negative impact on classification accuracies when remotely sensed imagery is used (Peña-Barragán et al. 2011), SVM has been shown to be less sensitive to intra-class variations compared to other classifiers (Zheng et al. 2015). This characteristic is believed to

have been a major contributing factor to its above-average performance in this study. Furthermore, SVM's use of an optimised sample for calculating support vectors and defining the hyperplane by prioritising samples that lie on the edge of the class distribution in feature space (Zheng et al. 2015) make it suitable for use with high-dimensional datasets. This explains the classifier's relatively good performance when all images were included in the classification (Experiment 4). The insignificance in the different OAs achieved among the various experiments in this study suggests that image selection does not have any significant impact on crop type mapping. This is an important finding for operational crop type mapping, as the use of all available cloud-free images reduces the complexity of automated workflows. However, images during the August/September period (a few weeks before harvest) are critical as it seems to have contributed the most to the OAs achieved in this study.

In this study, cloud-contaminated images were manually identified (through visual interpretation) and excluded from the analyses. Given that manual selection of cloud-free images is not viable for many operational implementations (e.g. over very large areas and involving multiple images), alternative approaches are needed. One option is to make use of cloud-masking algorithms (Sedano et al. 2011; Bai et al. 2016; Han, Bovolo & Lee 2017) to automatically select suitable images. Another option is to perform image compositing (Vancutsem 2007; Flood 2013; Lück & Van Niekerk 2016) to reduce the effect of cloud-contamination. These approaches warrant more research, particularly within the context of crop type classification.

This study made use of Sentinel-2A imagery only. It would be of interest to perform a similar set of experiments using the improved temporal resolution provided by the Sentinel-2B satellite (which became operational after the in situ survey of this study was carried out). The denser time-series provided by the combination of imagery from both satellites is expected to increase classification accuracies, but more research is needed to test this hypothesis.

3.6 CONCLUSION

This study investigated the use of five machine learning classifiers for crop type classification in two sites located in the Western Cape Province of South Africa. A set of cloud-free Sentinel-2 images was used as input to the classifiers. Considering the effort involved in developing crop calendars, as well as the impact of seasonal weather variations on the accuracy of such calendars, alternative approaches for selecting images were evaluated. Specifically, the efficacy of selecting images based on their uni-temporal performance (i.e. using a single image as input to the classifiers) was assessed. The performance of the machine learning classifiers when only pre-harvest images are used as input was also tested. The results showed that the selection of images based on individual performance offers a viable alternative to selecting images based on crop

developmental stages, but the effort and cost of implementing such an approach may not warrant the marginal (and insignificant) accuracy improvements observed. The findings of this study suggest that the classification of crops using an entire time-series can be as accurate as when a subset of hand-selected images are used. This suggests that image selection is not necessary for operational crop type mapping, which simplifies automated image processing workflows.

The principal finding of this study is that the crops (and fallow fields) considered herein can effectively be classified with images acquired from the beginning of June to before harvest (up to Sept). SVM and RF are recommended, as these classifiers performed consistently well in all the experiments.

CHAPTER 4: VALUE OF IMAGE COMPOSITING FOR DIFFERENTIATING PERENNIAL CROPS WITH MACHINE LEARNING AND MULTI-TEMPORAL SENTINEL-2 IMAGERY

4.1 ABSTRACT

Accurate and up-to-date crop type maps are needed for many applications. Spatially-explicit crop type information is used to estimate planted areas, which is invaluable for crop insurance assessments, supply-chain logistics, commodity trading and market forecasting. This study evaluated the efficacy of four simple image compositing techniques and the effects of cloud cover on perennial crop type classification in an agricultural region located in the Western Cape Province of South Africa. Four machine learning classifiers, namely: support vector machine (SVM), decision tree (DT), k-nearest neighbour (k-NN) and random forest (RF) were considered. Six experiments with different image sets were carried out. Cloud-free images were hand-selected for the first experiment while all images, including cloud-contaminated images, were used as input to the machine learning algorithms in the second experiment. These two experiments were undertaken to quantify the effect of cloud-contamination on crop classification accuracies. The remaining four experiments were carried out with different sets of monthly image composites. The four compositing techniques implemented were: mean compositing (MC), multidimensional analogue of the median (MEDOID), maximum normalised difference vegetation index (MaxNDVI) and minimum red (MinRed). The results show that when using all images – including cloud-contaminated images – overall accuracies of more than 75% were achieved. This is comparable to when different compositing approaches were implemented to reduce cloud-contamination. This finding is important for operational implementations as the use of all images eliminates the need to manually identify and exclude cloud-contaminated images from classifications. We conclude that using all available Sentinel-2 images is effective and that generating monthly Sentinel-2 composites is not beneficial for perennial crop type mapping.

4.2 INTRODUCTION

Ensuring food security for a continually growing population is a global priority. The expansion of areas under cultivation is a common response to the increasing demand for food. However, expanding croplands compromises the sustainability of other natural resources and ecosystems (Siachalou, Mallinis & Tsakiri-Strati 2015). An alternative to agricultural expansion is intensification, which is often associated with changes in agricultural products and practices. Dependable, up-to-date and accurate cropland mapping is needed to monitor these dynamics and

to ensure sufficient crop production while maintaining sustainable land use practices (Löw & Duveiller 2014).

Crop type information has traditionally been obtained through farmer communications, which in some instances is verified through field visits (Peña-Barragán et al. 2008). This approach is costly, time-consuming, and often produces inconsistent results (Peña et al. 2014). Consequently, agricultural censuses are not routinely carried out, particularly not in developing countries. For instance, in South Africa, the most recent national agricultural census was carried out in 2007 (StatsSA 2007). Although invaluable, this census provided an incomplete profile of agricultural activities in South Africa as many crop types were excluded. To address this gap, the Western Cape Department of Agriculture (WCDoA) embarked on an initiative to routinely map all agricultural areas in the Western Cape Province. The census was first carried out in 2012/2013 and was recently updated (WCDoA 2018). This was performed by means of a combination of expert (visual) interpretations during aerial surveys ("flyovers"), stakeholder meetings, field questionnaires, and telephonic surveys – a very costly exercise. In addition, each census took several years to complete, which means that the information is outdated by the time it is released.

Methods involving automated analyses of multi-temporal satellite imagery offer an objective, less tedious and more cost-effective alternative to agricultural censuses. The increasing availability of satellite sensors that provide imagery with high spatial, spectral and temporal resolution (for example Sentinel-2 satellite) offers new opportunities for the operational monitoring of agricultural activities at regional scales. Both single-date and multi-temporal techniques have been employed for mapping crop types with satellite imagery (Zheng et al. 2015; Inglada et al. 2016; Gilbertson & Van Niekerk 2017; Cai et al. 2018). In single-date approaches the spatial, spectral and temporal features of crop types are extracted from a single scene acquired during the growing season (Boryan et al. 2011; Yang, Everitt & Murden 2011), while multi-temporal approaches use a combination of imagery acquired throughout the growing season (Hao et al. 2015). While both approaches work relatively well for annual (field) crops, differentiating perennial crops (e.g. fruit orchards, vineyards, olive groves) is challenging due to their spectral similarity during long periods in the production cycle. For example, fruit trees such as apple, pear, peach and apricot trees may have very similar spectral characteristics during leave-on phenological stages. However, crop species are unlikely to have similar spectral characteristics throughout the entire production cycle, which makes multi-temporal classification suitable for fruit crop identification (Hochschild, Weise & Selsam 2005; Karjalainen, Kaartinen & Hyyppä 2008; Sabour, Lohmann & Soergel 2008).

Although multi-temporal approaches have been successfully used to identify crop types (Hao et al. 2015; Gilbertson, Kemp & Van Niekerk 2017), the vulnerability of optical imagery to cloud

cover compromises the performance of classifiers (Inglada et al. 2016). Innovative methods are needed to reduce the effect of cloud cover (and shadow) for crop type mapping. As such, image compositing has been used in various remote sensing applications to minimise the effects of cloud cover (Hüttich et al. 2011; White et al. 2014; Kussul et al. 2015; Lück & Van Niekerk 2016; Higginbottom et al. 2018). In essence, image compositing is achieved by aggregating image observations and replacing contaminated observations with good observations from imagery acquired within a stipulated compositing period (Liu, Ozdogan & Zhu 2013; Lück & Van Niekerk 2016).

Various image compositing approaches have been used, with the maximum value composite (MVC) – also known as the maximum value normalised difference vegetation index (MaxNDVI) composite – being the most commonly used multi-temporal compositing method (Holben 1986; Yan & Roy 2014; Lück & Van Niekerk 2016). MaxNDVI is computed by selecting the observation with the highest NDVI (Holben 1986) because it is assumed to represent a lower cloud fraction (Fraser, Massom & Michael 2009). MaxNDVI has been successfully used for vegetation monitoring (Kasischke et al. 1993; Diwakar et al. 1989; Potter & Brooks 2000; Du et al. 2001; Peters et al. 2002) but is unstable in areas with medium to low-density vegetation cover (Holben 1986). Discrepancies due to the vulnerability of the NDVI to soil background variations and atmospheric effects have also been reported (Roy, Kucukural & Zhang 2010). Replacing NDVI by the soil-adjusted vegetation index (SAVI) (Huete 1988) and atmospheric resistant vegetation index (ARVI) to account for these limitations (Kaufman & Tanre 1992) was not completely effective. An alternative to vegetation index-based approaches is the minimum red value (MinRed) (D'Iorio 1991) image compositing technique. MinRed selects the minimum red band reflectance, as the reflectance of clouds in the red band is significantly higher than that of vegetation. MinRed thus minimises the probability of selecting cloud-contaminated pixel values (Qi & Kerr 1997). Luo, Trishchenko & Khlopenkov (2008) evaluated MinRed and found that, although it was successful in eliminating clouds, it retained shadow-contaminated pixels in the final composite.

According to Vancutsem et al. (2007), selecting a single extreme value (e.g. minimum or maximum) may favour specific atmospheric and geometric conditions, which can result in spatial inconsistencies in the composites. An alternative is to make use of multiple values to identify uncontaminated observations. For instance, Lück & Van Niekerk (2016) combined different image compositing approaches, including MaxNDVI and MinRed, to develop a rule-based image compositing technique. The disadvantage of this approach is that a pre-classification is required to identify cloud-contaminated pixels and land cover classes to inform the selection of the appropriate values, which is a difficult and error-prone undertaking. As an alternative, the mean compositing

(MC) approach, averages all reflectance values per pixel and per spectral band within the specified compositing period (Vancutsem et al. 2007). Hüttich et al. (2011) found that MC was consistent and easy to apply when compared to other algorithms. Brems, Lissens & Veroustraete (2000) used the median composite of fuzzy multispectral estimate (MC-FUME) method to create 10-day composites of NOAA-AVHRR imagery. Unlike MC, MC-FUME uses the median value of the estimated top-of-canopy reflectance values to generate image composites. Yan & Roy (2014) also used median values in the web-enabled Landsat data (WELD) approach to generate annual composites of Landsat ETM+ imagery. Similarly, Flood (2013) employed a multidimensional analogue of the median (MEDOID) algorithm to select uncontaminated observations. From these results, it seems that the use of the centre (median) of a multivariate set of values to generate a composite is advantageous as it is less sensitive to outliers. However, the use of the median value is only effective when the number of uncontaminated observations exceeds those that are contaminated.

According to Inglada et al. (2015), imagery with high spatial and temporal resolution is needed for the accurate differentiation of crop types. The simultaneous operation of Sentinel-2A and -2B provides 10 m (spatial) resolution imagery at a revisit frequency of five days. Depending on the region of interest, up to four images can be collected within 10 days (Vuolo et al. 2018). In addition, the imagery has a relatively high spectral resolution, with 13 bands including three red-edge and two shortwave infrared (SWIR) bands (Delegido et al. 2010). These sensor and orbit characteristics provide an unprecedented combination of high spectral, temporal and spatial resolution imagery, at no cost to end-users, which makes it ideal for operational crop type mapping at field-level (Chapter 3).

Although many studies have evaluated different compositing techniques on MODIS, AVHRR and Landsat imagery, not much is known about how effective they will be for compositing Sentinel-2 imagery. To the best of our knowledge, the impact of cloud cover and using different compositing techniques on crop type differentiation with machine learning has not been evaluated before. This study thus investigates the value of four popular image compositing techniques for perennial crop type classification in a Mediterranean region within the Western Cape Province of South Africa. Crop type classification results when six different multi-temporal Sentinel-2 datasets are used as input to four machine learning classifiers (SVM, DT, RT, and k-NN) are compared. The first dataset (Dataset 1) consists of cloud-free images selected based on a crop calendar, while the second (Dataset 2) consists of all available images (including cloud-contaminated images). The rest of the datasets consist of monthly composites generated using the MC (Dataset 3), MEDOID (Dataset 4), MaxNDVI (Dataset 5), MinRed (Dataset 6) approaches. The results are interpreted in

the interest of developing an operational (automated) solution for crop type mapping in the Western Cape.

4.3 MATERIALS AND METHODS

4.3.1 Study site

This study was conducted in the lower west coast region of South Africa (Figure 4.1). The area, which is located about 50 km north of Cape Town, was chosen owing to the diversity of perennial crops cultivated in the region. The site has a Mediterranean climate, which is characterised by warm and dry summers, and a cool and wet winter season (Malan 2016). The area receives an average annual rainfall of 550 mm, with a minimum temperature of 11°C and a maximum temperature of 22° C (Tererai et al. 2015). A variety of crops are grown in the area, with the most common perennial crops being pome fruits (apple and pear), citrus fruits (orange, lime, lemon and tangerine), stone fruits (apricot, olive, peach and plum), grapes (table and wine grapes), tree fruits (pomegranate, persimmon and guava) and planted pastures (WCDoA 2018). The study was undertaken during the 2017/2018 growing season.

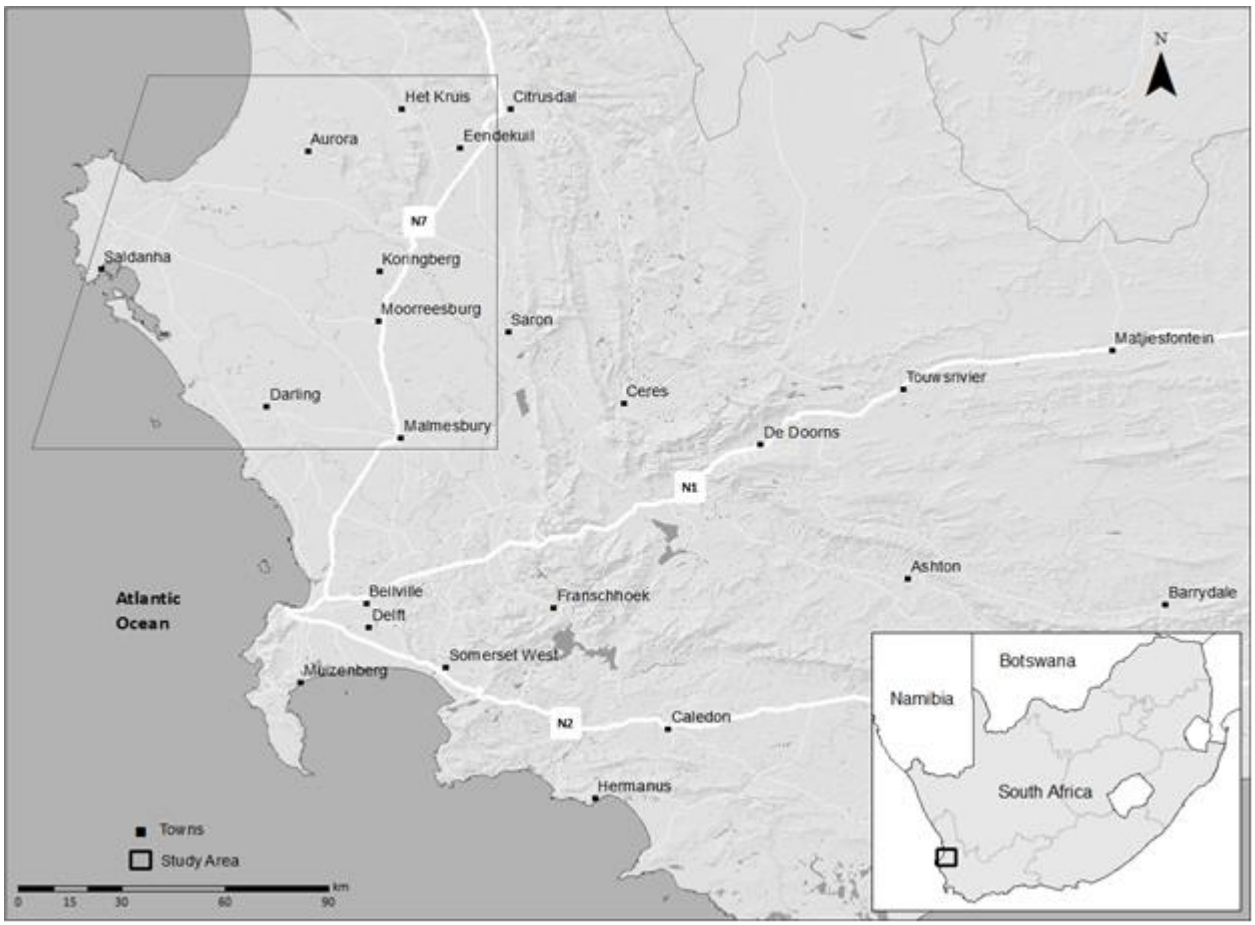

Figure 4.1 Location of the study site in the Western Cape, South Africa

4.3.2 Satellite imagery acquisition and preparation

All available Sentinel-2A and -2B images captured between June 2017 and March 2018 were sourced from the Sentinel Hub (https://www.sentinel-hub.com/). The period was chosen to coincide with a typical growth cycle of perennial crops in the study area. Data preparation involved resampling the 20 m spectral bands to 10 m (Immitzer, Vuolo & Atzberger 2016). All images were pre-processed at Level 1C, which includes radiometric and geometric corrections (orthorectification and spatial registration on a global reference system with sub-pixel accuracy). Figure 4.2 presents the number cloud-free images versus cloud-contaminated images per month.

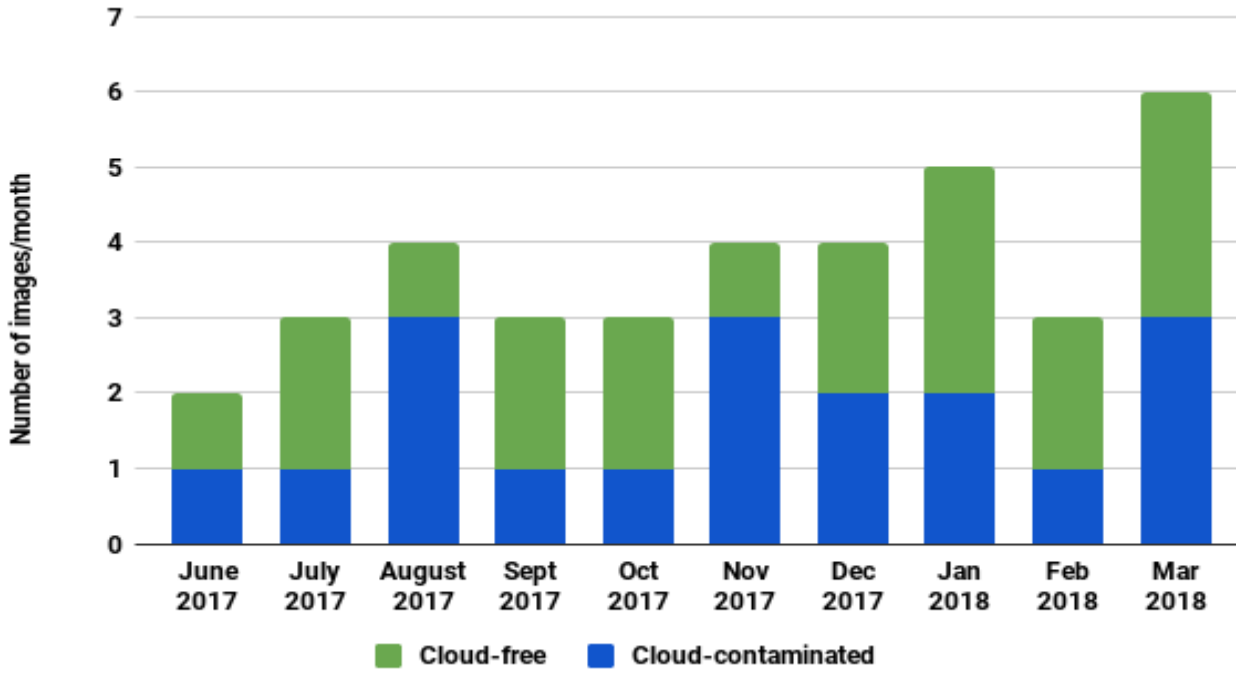

Figure 4.2 Number of cloud-free images versus the number of cloud-contaminated images collected for each month

4.3.3 In situ data collection and field delimitation

A geographical information system (GIS) vector-based crop type boundary dataset containing polygons of agricultural fields was obtained from the Western Cape Department of Agriculture. These field boundaries were used as objects (basic units for classification). A stratified random sampling technique was used to select 945 perennial crop fields, which were subsequently used for training and validating the classifiers. The crop types and number of samples per class are given in Table 4.1.

Table 4.1 The number of samples per class

Crop type	Sub-class	Number of samples/crop type
Citrus fruit	Orange, Lime, Lemon, Naartjie	114
Pome fruit	Apple & Pear	94
Stone fruit	Apricot, Olive, Peach, Plum, Nectarine	100
Exotic fruit	Pomegranate, Persimmon, Guava	60
Planted pastures		326
Grapes	Table grapes, Wine grapes	251

4.3.4 Image feature set development

23 features (per image date) were generated from the Sentinel-2 bands (Table 4.2). The coastal aerosol (Band 1), water vapour (Band 9) and SWIR cirrus (Band 10) bands were not included in the classifications, as they were reported by Immitzer, Vuolo & Atzberger (2016) and Inglada et al. (2016) to be unsuitable for crop type classification. Six vegetation indices (VIs) (Table 4.2) commonly used in vegetation studies were derived using the equations in Table 4.3. Homogeneity, dissimilarity and entropy texture features measuring pixel uniformity and disorder were also calculated and included in the classifications (Schmedtmann & Campagnolo 2015). A principal component analysis (PCA) was performed on all spectral bands per image date, and the first four principal components (PCs) were retained as recommended by Gilbertson, Kemp & Van Niekerk (2017). Mean values for all spectral features were calculated for each agricultural field.

Table 4.2 Features used as input for classifications (refer to Table 4.3 for the full names, formulae and bands used to compute each feature)

Variable source	Features
Spectral bands	Blue, Green, Red, Vegetation red-edge1, Vegetation red-edge2,
	Vegetation red-edge3, NIR, Narrow NIR, SWIR1, SWIR2
Spectral indices	ARVI, GNDVI, IPVI, NDVI, RVI, SAVI
Textural features	Dissimilarity, Entropy, Homogeneity
Image transforms	PC1, PC2, PC3, PC4

Table 4.3 Equations used to calculate the vegetation indices considered in the classifications

Name	Index	Formulation	Source
Atmospherically resistant vegetation index	ARVI	$\frac{NIR - RED}{NIR + RED} - \frac{y\,(RED - BLUE)}{y(RED + BLUE)}$	Kaufman & Tanre (1992)
Green normalised vegetation difference index	GNDVI	$\frac{NIR - GREEN}{NIR + GREEN}$	Gitelson & Merzlyak (1998)
Normalised difference vegetation index	NDVI	$\frac{NIR - RED}{NIR + RED}$	Rouse (1974)
Infrared percentage vegetation index	IPVI	$\frac{1}{2}NDVI + 1$	Crippen (1990)
Ratio vegetation index	RVI	$\frac{NIR}{RED}$	Jordan (1969)
Soil-adjusted vegetation index	SAVI	$(1 + L) = \frac{NIR - RED}{NIR + RED + L}$	Huete (1988)

4.3.5 Experimental design

The experimental design is shown in Figure 4.3. The first two experiments involved undertaking the classifications using non-composited images, with Experiment 1 using selected cloud-free images only, while Experiment 2 involved using all available images (including those contaminated by clouds). For the last four experiments, monthly composites were generated using the following approaches:

- Mean compositing (Vancutsem et al. 2007);
- Median compositing (Flood 2013);
- MaxNDVI (Roy, Kucukural & Zhang 2010);
- MinRed (Liang, Li & Wang 2012).

The supervised learning and image classification environment (SLICE) software, developed by the Centre for Geographical Analysis (CGA) at Stellenbosch University, was used for classification and accuracy assessment (Myburgh & Van Niekerk 2013). SLICE includes several classification algorithms, namely: SVM, k-NN, DT, RF and maximum likelihood (maxlike). The ML and k-NN classifiers were implemented using the Open CV 2.2 libraries (Bradski 2000), while Libsvm 3.0 was used to implement the SVM classifier (Chang 2011). The parameters for DT and RF were based on the guidelines provided in the Open CV library documentation. The Geospatial data abstraction library (GDAL) was used to manipulate the raster files and shapefiles. (See

Myburgh & Van Niekerk (2013) for an incisive description of how the various classifiers were configured).

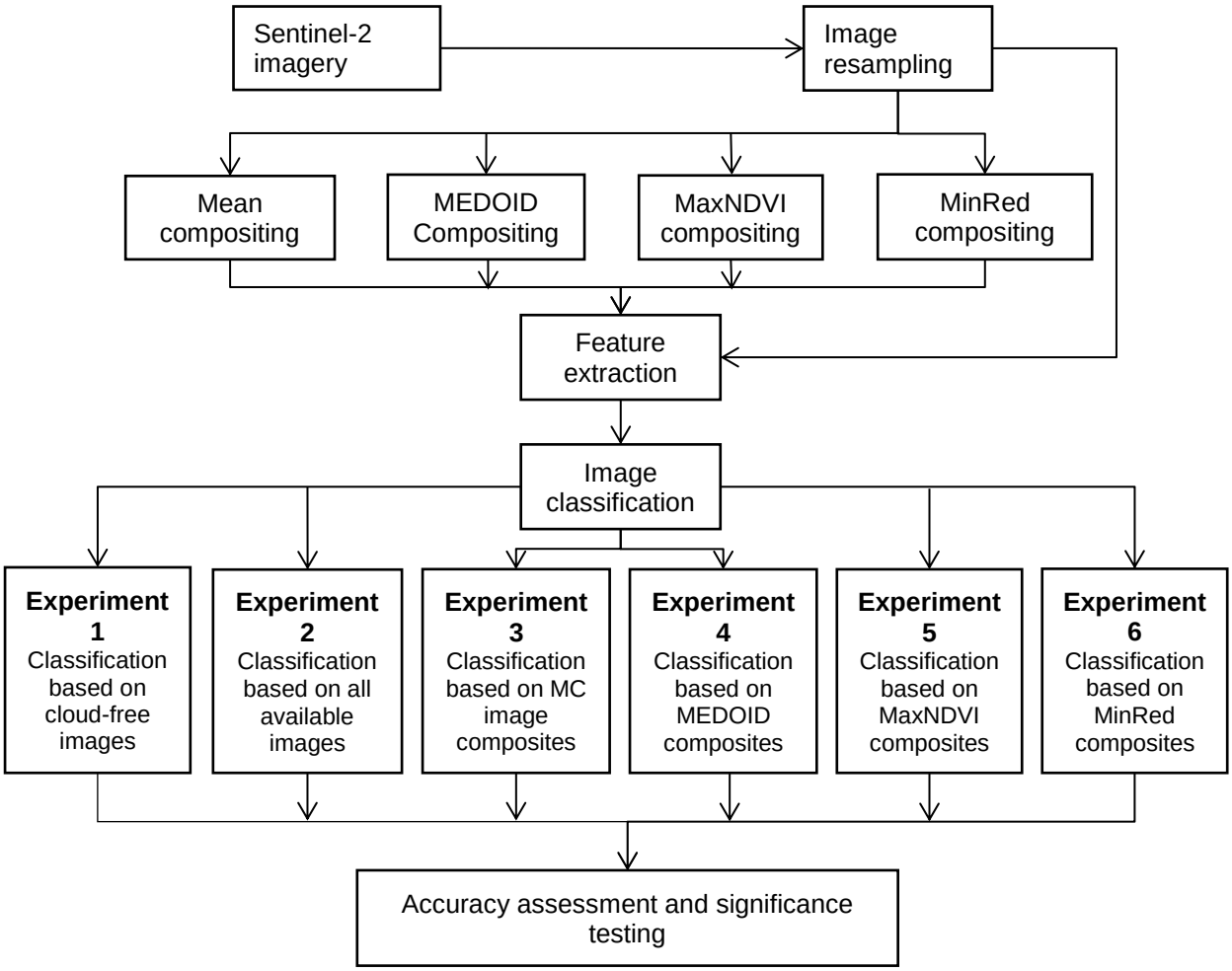

Figure 4.3 Experimental design for assessing the value of image compositing for crop type mapping

A 3:2 sample split ratio was employed for accuracy assessment, i.e. 40% of the samples were randomly selected and excluded from classifier training. These samples were then used to validate the classifications. The same set of training and validation samples were used for all the experiments. Overall accuracy (OA) and the kappa coefficient (K) was calculated for every classification. McNemar's test, ANOVA and t-tests (as implemented in Microsoft Excel) were used for assessing the statistical significance of the accuracies obtained from the experiments, as recommended by Foody & Mathur (2004). The alpha values for ANOVA and t-tests were set to 0.05, while the alpha value for McNemar's test was set to 1.96.

4.4 RESULTS

The results of the six experiments are summarised in Table 4.4. Using all images as input to the classifiers, including those contaminated by clouds (Experiment 2), recorded the highest OA among all of the classifiers (mean OA = 72.6%), followed by using selected cloud-free images

(Experiment 1) (mean OA = 72.4%). The use of median composites (Experiment 4) yielded the lowest accuracies (mean OA = 70.3%). According to a two-tailed t-test, the differences in mean OAs obtained with the different experiments are statistically insignificant ($p > 0.683$). However, the 2.3% range in mean OAs suggests that different approaches can have an impact on accuracies.

Table 4.4 Overall accuracies (OA), mean OAs and standard deviations (SD) for all experiments

Experiment	**SVM**		**RF**		**k-NN**		**DT**		**AVG**		**SD**	
	OA	K	OA	K	OA	K	OA	K	OA	K	OA	K
1	77.5	0.70	77.2	0.70	73.7	0.70	61.2	0.49	72.4	0.64	6.66	0.09
2	81.0	0.75	77.2	0.70	69.2	0.60	63.3	0.52	72.6	0.64	6.88	0.08
3	78.5	0.72	75.8	0.68	72.1	0.63	62.7	0.52	72.2	0.63	5.97	0.07
4	77.2	0.70	75.8	0.68	61.1	0.57	67.2	0.49	70.3	0.61	6.55	0.08
5	76.7	0.69	78.0	0.71	67.1	0.57	63.1	0.52	71.2	0.62	6.30	0.07
6	77.8	0.71	73.2	0.64	67.6	0.58	65.7	0.55	71.0	0.62	4.76	0.06
AVG	78.1	0.71	76.2	0.68	68.4	0.60	63.8	0.51				
SD	1.53	0.02	1.70	0.02	4.42	0.02	0.01					

Of the compositing methods, MC (Experiment 3) yielded the highest accuracy (mean OA = 72.2%), while MEDOID produced the least accurate classification (mean OA = 70.3%). Figure 4.4 and Figure 4.5 presents the results achieved when the different compositing approaches are used under different conditions (i.e. densely vegetated vs. sparsely vegetated). A visual inspection of Figure 4.5 shows the ability of MC to eliminate clouds. According to what is shown in Figure 4.4, the MC approach retained some clouds. From visually inspecting both Figure 4.4 and Figure 4.5, the MC approach seems to perform poorly over areas with a high frequency of cloud cover. The MEDOID approach, on the other hand, was more successful with removing clouds/shadows over sparsely vegetated areas (Figure 4.5) but was inconsistent over densely vegetated areas (Figure 4.4). On the contrary, the MaxNDVI performed relatively well over vegetated areas (Figure 4.4) but performed poorly over sparsely vegetated areas (Figure 4.5). While the MinRed was able to eliminate clouds in all instances, Figure 4.4 & Figure 4.5 show that this approach retains cloud shadows. It is clear from both Figure 4.4 & Figure 4.5 that the efficacy of the different compositing approaches for eliminating clouds varies with the surface type and cloud cover characteristics and intensity.

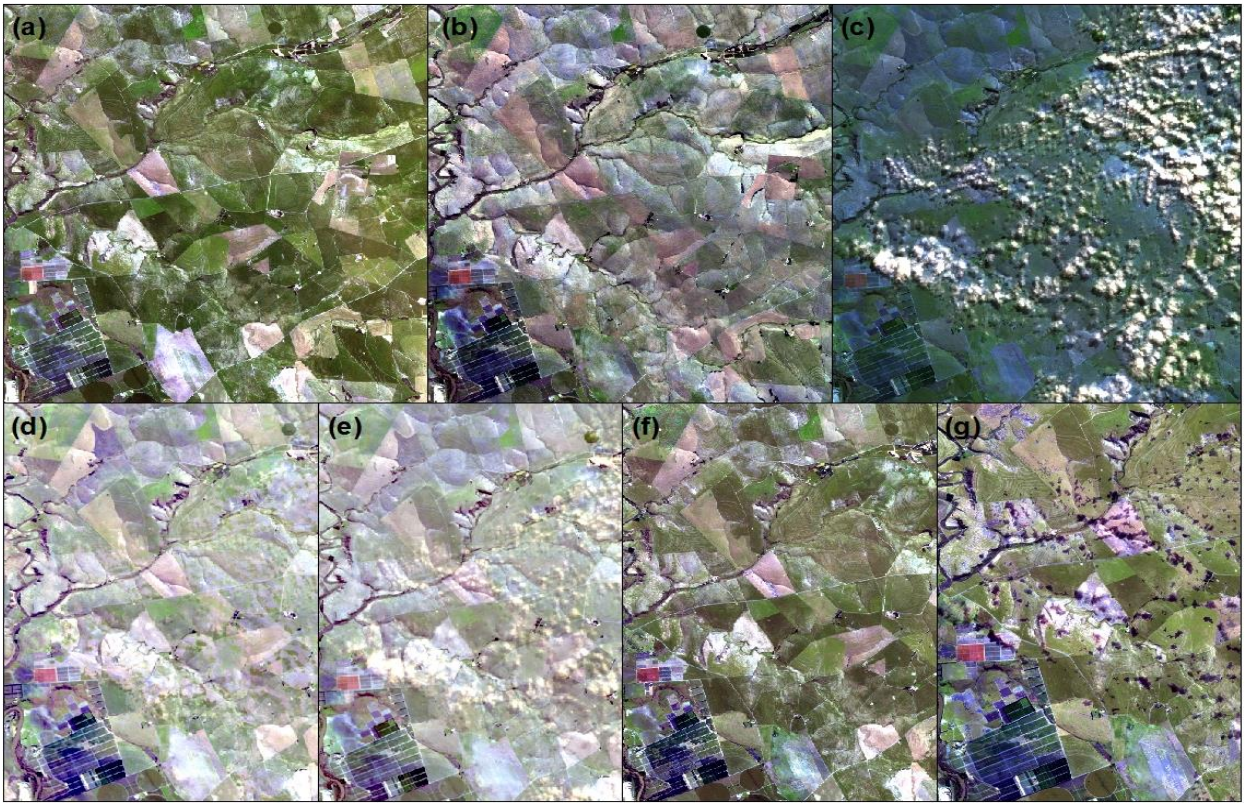

Figure 4.4 Individual images of a densely vegetated area acquired on (a) 3rd, (b), 5th and (c) 10th July 2017 – with (a) containing cloud-contaminated pixels – compared to image composites generated with (d) MEDOID, (e) MC, (f) MaxNDVI and (g) MinRed.

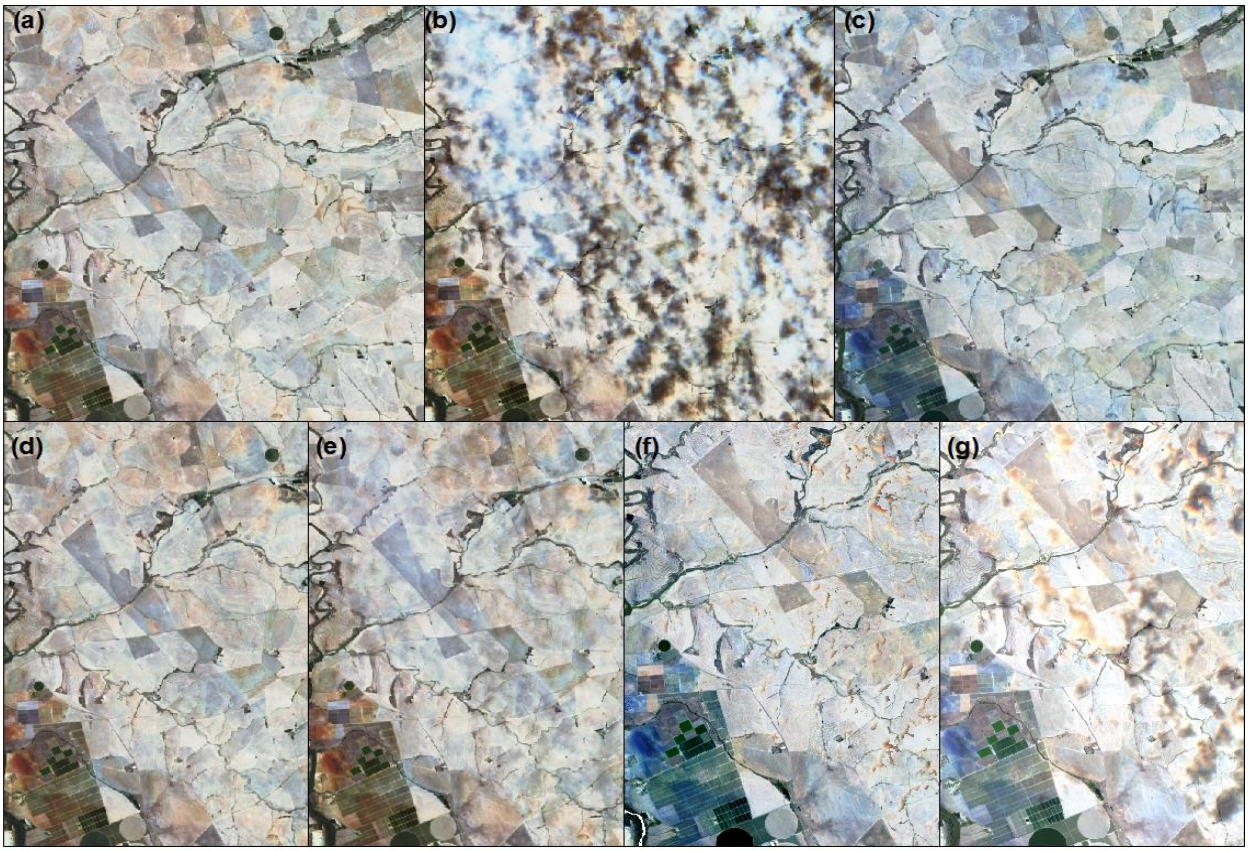

Figure 4.5 Individual images of a sparsely vegetated area acquired on (a) 12th, (b) 17th and 27th December 2017 – with (b) containing cloud-contaminated pixels – compared to image composites generated with (d) MEDOID, (e) MC, (f) MaxNDVI and (g) MinRed.

Overall, the most accurate classification was achieved in Experiment 2, using SVM (OA = 81%), while the least accurate classification was achieved in Experiment 4, using the k-NN classifier. The superiority of SVM was observed across all experiments, with the exception of Experiment 5, in which RF achieved a slightly (1.3%) higher OA. Generally, SVM (mean = 78.1%) and RF (mean = 76.2%) outperformed the other classifiers in all experiments (Table 4.4) with only marginal (2%) differences between the two classifiers. K-NN and DT obtained the lowest OAs, recording average OAs of 69.6% and 63.3% respectively. The difference in the classification accuracy of SVM and RF in comparison to that of k-NN and DT is statistically significant (two-tailed t-test p-values < 0.004).

Based on the confusion matrices of SVM and RF, grapes and stone fruits were the most frequently misclassified crop types (mean PA < 70% for both classes) (Table 4.5). The confusion of grapes and stone fruits were noted in all experiments, with the exception of Experiment 5 (MaxNDVI) in which stone fruits (PA=53.1%) were misclassified much more frequently than grapes (PA=72%) when SVM was used as the classification algorithm. At closer inspection, it was observed that the low PA of grapes was due to the misclassification of some vineyards as planted pastures, while several stone fruit orchards were misclassified as pome fruit orchards. Planted pastures were the least confused (mean PA > 90%), followed by pome fruits (mean PA > 80%). A slight increase in the confusion of citrus and exotic fruits was observed when RF was used as the classification algorithm, resulting in lower PAs compared to those achieved with SVM (Table 4.5).

Table 4.5 Crop specific producer's accuracies of the two best-performing classifiers (SVM and RF)

	SVM						**RF**						
	Exp1	**Exp2**	**Exp3**	**Exp4**	**Exp5**	**Exp6**	**Exp1**	**Exp2**	**Exp3**	**Exp4**	**Exp5**	**Exp6**	**AVG**
Citrus fruit	84.7	82.6	82.6	84.7	80.4	80.4	78.2	76	73.9	73.9	73.9	76	75.5
Grapes	66	68	65	65	72	69	69	71	71	68	73	69	69.7
Pasture	91.1	99.1	95.1	91.1	91.1	91.9	94.3	94.3	92.7	96.7	93.5	91.1	94.7
Pome fruit	89.4	81.5	78.3	78.3	65.7	71	89.4	89.4	81	75.6	86.8	76.3	83.8
Stone fruit	51	59.5	59.5	61.7	53.1	61.7	44.6	38.2	42.5	42.5	48.9	34	41.9
Exotic fruit	68.4	78.9	78.9	68.4	78.9	78.9	63.1	73.6	68.4	68.4	68.4	63.1	68.3

4.5 DISCUSSION

None of the experiments stood out as being superior for identifying perennial crops. However, using all available images, inclusive of cloud-contaminated images, (Experiment 2) produced slightly better results (72.6%) compared to the other scenarios. Although the differences in the

mean OAs of the experiments were within a narrow margin (2.3%) and insignificant, this finding is encouraging as it suggests that the considered algorithms (particularly SVM and RF) were insensitive to the noise caused by cloud-contamination and that – within our study area – complex pre-classification procedures may not be required for operational crop type mapping. This is in agreement with Rodriguez-Galiano et al. (2012), who noted the ability of machine learning classifiers to handle noisy data. For instance, RF uses a subset of labelled samples and variables to identify features that contribute most to an accurate classification. It is likely that cloud-contaminated variables are excluded from (or are considered less important in) the classification outputs. Conversely, SVM uses an optimised subsample of labelled instances to define a hyperplane (Zheng et al. 2015). Because these support vectors are located at the edges of class separation in feature space (Brown, Lewis & Gunn 2000), it is unlikely that they would include cloud-contaminated samples (because cloud-contaminated samples would have similar spectral vectors) (Zheng et al. 2015). Also, both SVM and RF are robust against high feature dimensionality; as a result, these classifiers performed well using more than 880 features as input (Experiment 2). This corresponds with Gilbertson & Van Niekerk (2017) who also reported SVM and RF to be superior to other classifiers under high feature dimensionality.

Generally, image compositing did not have any positive impact on accuracies (mean OAs of Experiments 3–6 were 2.1% lower than the mean OAs of Experiments 1 and 2). The poor performance of the compositing techniques is partially attributed to the use of a monthly compositing interval, as it may have been inadequate to capture the phenological characteristics of the targeted crops. The five-day temporal resolution provided by the Sentinel-2 constellation mission limits the total number of available images to four per month (depending on the location of the area of interest), which makes the implementation of shorter compositing periods unviable (i.e. the risk that all observations are cloud-contaminated becomes too high). This was confirmed by a qualitative assessment of the resulting image composites, which revealed evidence of cloud-contamination in several cases. Cloud shadows were also not removed in all cases. For example, when the image composites of July 2017 (a period of high vegetation cover due to relatively high rainfall) and December 2017 (dry period with reduced vegetation cover) are compared, it is clear that MaxNDVI performed well over vegetated areas, but failed in sparsely vegetated areas. Our results show that MinRed does not remove cloud shadows, which is in agreement with Liang, Li & Wang (2012). MC performed poorly in areas where the frequency of cloud cover was high. This is not unexpected, given that the technique simply averages all reflectance values over the compositing period. It is also well known that averaging is sensitive to outliers (very high and low values due to clouds and shadows respectively). This finding concurs with Flood (2013), who reported that MC was unable to successfully reduce the effects of clouds.

Grapes and stone fruits were frequently misclassified (Table 4.5). According to Lundy (2017), cover crops such as rye, oats, lupins and peas are planted in-between vine rows to add organic matter, supplement nitrogen and other nutrients, and to aerate soils. Cover crops also help to suppress weed growth, which reduces the need for herbicides. Cover crops have very different spectral and phenological characteristics to those of vines and may have negatively influenced classifier performance. The misclassification of stone fruits is attributed to within-class variations in some of the classes. For example, apricots and olives are grouped in the stone fruit class, but olives flower between March and May while apricots flower between July and September (more or less the same time as pome fruits). These intra-class phenological differences may have negatively influenced the classification results. In addition, different farming practices and crop conditions likely also negatively influenced classification accuracies. Citrus and pasture were relatively well differentiated. PAs of more than 80% were achieved across all experiments using SVM. This is attributed to the distinct spectral and phenological characteristics of these classes (e.g. evergreen trees vs. grasses).

Overall, the insignificant difference in mean OAs achieved by the different experiments undertaken in this study suggests that identifying cloud-free images prior to image classification does not improve classification accuracies. This finding is encouraging because manually identifying cloudy observations is not feasible in operational implementations. The ability of the machine learning algorithms, particularly SVM and RF, to identify crops using all available images (including those contaminated by clouds) is of great value for designing operational crop type mapping workflows. It also suggests that extensive pre-processing (e.g. image compositing) is not needed, which would reduce the computational expense and complexity of operational workflows, particularly when multi-temporal approaches are used over large areas.

4.6 CONCLUSION

This study evaluated the efficacy of four image compositing techniques for perennial crop type classification in an agricultural region located in the Western Cape Province of South Africa. The effect of cloud cover on crop classification accuracies was also evaluated. The results showed that the highest accuracies were obtained when the SVM and RF classifiers were applied to all available images, including those contaminated by clouds. This finding suggests that pre-assessing images prior to classification – to identify cloud-free images – is not necessary in our study area. In addition, it seems that there is no benefit in performing image compositing prior to classification. In fact, image compositing reduced the ability of the machine learning classifiers to differentiate between the targeted crop types. The most likely explanation for this finding is that compositing reduces the fidelity of the multi-temporal Sentinel-2 imagery, thereby reducing the ability of the

machine learning algorithms to detect subtle phenological changes. Visual inspections also revealed artefacts (noise) in the image composites. Although SVM and RF were able to effectively ignore cloud and cloud shadow observations when all the images were used as input (Experiment 2), the spectral artefacts introduced by image compositing are more subtle (less distinct) and were likely regarded as uncontaminated observations by the classifiers. This would have had a negative effect on accuracies.

Although the findings of this study provided new insights into the effect of cloud cover on crop type mapping using machine learning, the results should be interpreted within the context of Mediterranean climates where cloud cover is relatively infrequent, compared to other regions. The value of image compositing might be different in areas with higher cloud cover frequencies (e.g. the tropics). In such areas it may be of value to incorporate imagery from other satellites, such as Landsat, to increase temporal resolution. Another approach to improve classification accuracies would be to increase the number of labelled instances used for classifier training, but more work is needed to investigate the cost-benefits of increasing training set sizes for operational crop type mapping.

CHAPTER 5: SYNTHESIS – TOWARDS OPERATIONAL CROP TYPE MAPPING WITH REMOTE SENSING

This study is relevant because of the significant contribution of the agricultural sector to the economies of developing countries such as South Africa. Up-to-date crop type data is required for accurate crop production monitoring. Crop type information is necessary for estimating planted areas and crop yields, which are crucial for decisions relating to food security and the forecasting of commodity markets. Although various studies have successfully applied remote sensing techniques for mapping crop types, they often involve workflows that are not viable for use in operational map production systems through which crop type maps can be systematically and automatically generated. This chapter synthesizes and reflects on the findings of this study. The first section revisits the aim, objectives and research questions. The main findings of the study are then summarised and evaluated, after which limitations, recommendations and directions for further research are outlined. The chapter ends by presenting the conclusions drawn from the study.

5.1.1 Revisiting aim and objectives

The study aimed to evaluate the value of machine learning classifiers and multi-temporal Sentinel-2 data for discriminating crop types grown in a Mediterranean climate in the Western Cape Province of South Africa. To realize this aim, the objectives were: review literature on remote sensing for crop type mapping (Objective 1); investigate the significance of image selection for crop type classification (Objective 2); assess classifier performance when only pre-harvest images are used as input (Objective 3); investigate the impact of cloud cover and image compositing on crop type classifications (Objective 4).

The literature review (Chapter 2) focused on the application of optical remote sensing for classifying crop types, with specific emphasis on pre-processing and interpretation methods applied to remotely sensed imagery. Multi-temporal approaches for crop type mapping, image classification approaches, and measures used for assessing the accuracy of image classification results were also overviewed. It was concluded that multi-temporal approaches are most effective for crop type identification (Hao et al. 2015; Zheng et al. 2015; Gilbertson, Kemp & Van Niekerk 2017), with several studies suggesting the use of Sentinel-2 imagery (Immitzer et al. 2016; Kussul et al. 2017; Veloso et al. 2017). However, the literature review revealed that very little is known about the efficacy of Sentinel-2 imagery for mapping both perennial and non-perennial crop types.

Following the literature review, the value of image selection for crop type mapping (Objective 2) was investigated. This was achieved by comparing two different approaches based on 1) crop developmental stages and 2) the performance rank of individual images. Applying the two

approaches also enabled us to evaluate the efficacy of selecting images based on the performance of individual images as a possible alternative to the conventional way of image selection based on crop developmental stages (Hao et al. 2015). Objective 2 was accomplished by setting up Experiments 1–3, where Experiment 1 determined the five best-performing uni-temporal images within a specific growing season, which were used for crop classification in Experiment 2. In Experiment 3, five images based on crop developmental stages were selected, as recommended by Gilbertson, Kemp & Van Niekerk (2017). The two image selection approaches of Experiments 2 and 3 were then compared with Experiment 4 (using the entire time-series) to assess the significance of image selection on crop type classification accuracies.

The performance of machine learning classifiers when only pre-harvest images are used as input (Objective 3) was evaluated in Experiment 4, which was set up by incrementally adding images to the classification. This made it possible to assess the progression in classification accuracy as a function of time and the number of images. Objective 2 and 3 were both addressed in Chapter 3.

While the second and third objectives focused on non-perennial crops, the fourth objective focused on perennial crops. This was addressed by Experiments 5 to 10 (Chapter 4), through which the effect of clouds and image compositing on crop classification accuracies was investigated. Four different image compositing techniques, namely: MC, MEDOID, MaxNDVI and MinRed were considered.

5.1.2 Main findings of the study

The results of Experiments 5 to 10 show that using all available images – including those contaminated by clouds – produced more accurate maps than when the image composites and hand-selected images were used as input. Image compositing was not beneficial for crop type classification accuracies. Image selection – based on a crop calendar or based on pre-assessments – did not have a significant influence on crop classification accuracies when compared to using either pre-harvest images only or the entire time-series. Although much research has been conducted on the feasibility of image selection for identifying crop types, no work has been done on the significance of image selection for mapping crop types. This is an important finding for operational crop type classifications as it warrants the use of all available images. However, it is important to note that these results are interpreted within the context of Mediterranean climates where cloud cover is relatively infrequent compared to other regions. The results might differ in areas with higher cloud cover frequencies (e.g. the tropics).

While the use of multi-temporal imagery for classifying crop types is a common application in remote sensing, pre-harvest classification of crop types using high spatial and temporal resolution

imagery such as Sentinel-2 had not been explored prior to this study. The availability of crop type data before harvest is beneficial for commodity market forecasting, risk assessments, and food security monitoring. From the five classifiers evaluated, SVM and RF were the most effective in identifying non-perennial crop types pre-harvest (approximately eight weeks before harvest) in both study sites.

Identifying and hand-selecting images unaffected by cloud cover is tedious and time-consuming. Experiments 5 and 6 evaluated the sensitivity of machine learning classifiers to noise introduced by clouds within the context of crop type mapping. The results show that machine learning classifiers – especially SVM and RF – were able to handle the noise introduced by cloudy observations; in fact, they performed better when cloud-affected images were included in the classifications. This agrees with the findings of others that both SVM and RF are robust against outliers (Myburg & Van Niekerk 2014; Zheng et al. 2015). It also has practical value for operational implementations as it suggests that in areas with cloud cover frequencies similar to the study area, the selection and assessment (crop calendar/performance ranking-based) of imagery pre-classification are not necessary.

Much research has been done on the efficacy of machine learning for crop type mapping, but most of it focused on non-perennial crops (Gilbertson, Kemp & Van Niekerk 2017). This study found that, although perennial crop type differentiation is a complex task – given that many of the crops are spectrally and structurally similar – SVM and RF, coupled with Sentinel-2 imagery, is a viable solution for differentiating and mapping perennial crops.

The main findings of this research are summarised as follows:

- Image selection based on the performance ranking of uni-temporal images provides a viable alternative to the conventional approach of selecting images based on crop developmental stages.
- There was no statistical difference between selecting specific images, using pre-harvest images only or using the entire time-series as input to the classifiers.
- Images collected between August and September contributed the most to crop classification accuracies and produced the highest OAs, even as single images (> 79%).
- The best pre-harvest crop type classifications were obtained using the SVM and RF algorithms. SVM and RF also yielded the most accurate crop type classifications when cloudy images were included, thus demonstrating their capability to handle noise.

- Machine learning classifiers based on Sentinel-2 imagery yielded reliable perennial crop type maps, despite the challenges introduced by the structural variations, different agronomic practices and spectral similarities among the targeted classes.

5.1.3 Limitations, recommendations and suggestions for future research

This research was undertaken in study sites representative of a Mediterranean climatic region characterised by winter rainfall and dry summers. The results of this study should be interpreted within this context and different results may emerge in other climatic regions. This is because the seasonal characterisation of a region has a direct impact on image availability due to factors such as cloud cover. It is consequently recommended that different climatic regions be considered in future studies.

Several studies have proven the efficacy of image selection for crop type mapping (Peña-Barragán et al. 2011; Brown et al. 2013; Hao et al. 2015). However, these studies selected images based on crop calendars. Considering the effort involved in developing crop calendars for each targeted region, as well as the impact of seasonal weather variations on the accuracy of such calendars, alternative approaches for selecting images were evaluated. While both approaches proved to be sufficient for crop type classifications, the classification undertaken with the entire time-series (by incrementally adding images) revealed that images collected during the August/September (maturation) period have the greatest influence on classification accuracies. It was also noted that images collected between the end of harvest and the beginning of a new growing season do not contribute much to classification accuracies. It is therefore recommended that future studies independently assess the importance of images acquired during August/September.

Although a monthly compositing period has been reported to be effective (Loveland et al. 2000; Friedl et al. 2010; Hüttich et al. 2011) to reduce cloud-contamination, the five-day revisit frequency of the Sentinel-2 imagery used in this research may be too low in areas or seasons with high frequencies of cloudy conditions. For instance, in this research, there were compositing periods with more cloudy observations than cloud-free images (e.g. November 2017 only had one cloud-free observation). This had a detrimental effect on the compositing techniques, especially MaxNDVI, which averages the reflectance values of all observations. More research is needed on combining Sentinel-2 imagery with other sources of imagery to increase the number of observations in compositing periods – as demonstrated by Xiong et al. (2017) and Skakun et al. (2017) using Landsat-8 imagery.

During the period in which this study was undertaken, Sentinel-2 imagery was only available at 1C processing level (top-of-atmosphere reflectance). In the interest of producing image composites

with minimal pre-processing (to simplify the image classification workflows), no further pre-processing was undertaken prior to classifications. Future research should make use of the Sentinel-2 imagery at processing level 2A (top-of-canopy reflectance), which has recently been released. The use of this imagery would be beneficial for most of the image compositing techniques. Ideally, BRDF corrections should also be carried out prior to compositing.

Advanced compositing techniques, such as rule-based image compositing implemented by Lück & Van Niekerk (2016), hold much potential for overcoming the limitations encountered with the image compositing techniques evaluated in this research. However, rule-based compositing adds a level of complexity to mapping workflows and more work is needed to make such techniques easy and implementable.

5.1.4 Conclusion

This study investigated the use of machine learning classifiers for crop type classification in two sites located in the Western Cape Province of South Africa. Four research objectives (1.3) were set to address the aim. The conclusions drawn from the study are that image selection based on the individual performance (ranking) of images offers a viable alternative to selecting images based on crop developmental stages. However, the additional computational cost of implementing such an approach may not warrant the marginal (and insignificant) accuracy improvements observed in this study. The findings of this study also suggest that the accuracy achieved when using an entire time-series can be as high as when a subset of hand-selected images is used. This suggests that image selection is not necessary for operational crop type mapping in the study area, which simplifies automated image processing workflows.

The research also revealed that the non-perennial crops (and fallow fields) considered in this study can be effectively classified with images acquired from the beginning of June to before harvest (up to Sept). SVM and RF are recommended, as these classifiers performed consistently well in all the experiments.

The study demonstrated that perennial crops (fruits and fallow fields) can be classified using all images, including those contaminated by clouds. This finding suggests that there is no need to exclude cloud-contaminated images, which would simplify the automation of image processing workflows.

Crop type data and statistics are essential for continuous monitoring of agricultural activities and crop production (yields). This information is of particular importance in developing countries such as South Africa, where a large proportion of the population (often the poor) are dependent on agriculture for providing food and employment. The experiments undertaken in this study provide

a good foundation for operational implementations of crop type map production and will hopefully contribute to economic growth through the realization of more sustainable and cost-effective agricultural production.

REFERENCES

Adam E, Mutanga O & Rugege D 2010. Multispectral and hyperspectral remote sensing for identification and mapping of wetland vegetation: A review. *Wetlands Ecology and Management* 18(3): 281-296.

Aguilar M, Vallario A, Aguilar F, Lorca A & Parente C 2015. Object-based greenhouse horticultural crop identification from multi-temporal satellite imagery: A case study in Almeria, Spain. *Remote Sensing* 7(6): 7378-7401.

Akar Ö & Güngör O 2012. Classification of multispectral images using Random Forest algorithm. *Journal of Geodesy and Geoinformation* 1(2): 105-112.

Akar Ö & Güngör O 2015. Integrating multiple texture methods and NDVI to the Random Forest classification algorithm to detect tea and hazelnut plantation areas in northeast Turkey. *International Journal of Remote Sensing* 36(2): 442-464.

Al-Doski J, Mansorl SB & Shafri HZM 2013. Image classification in remote sensing. *Journal of Environment and Earth Science* 3(10): 2225-0948.

Almeida TIRD & Filho DS 2004. Principal component analysis applied to feature-oriented band ratios of hyperspectral data: A tool for vegetation studies. *International Journal of Remote Sensing* 25(22): 5005-5023.

Archer KJ & Kimes RV 2008. Empirical characterization of random forest variable importance measures. *Computational Statistics & Data Analysis* 52(4): 2249-2260.

Asgarian A, Soffianian A & Pourmanafi S 2016. Crop type mapping in a highly fragmented and heterogeneous agricultural landscape: A case of central Iran using multi-temporal Landsat-8 imagery. *Computers and Electronics in Agriculture* 127: 531-540.

Athick AMA & Naqvi HR 2016. *A method for compositing MODIS images to remove cloud cover over Himalayas for snow cover mapping*. In 2016 IEEE International Geoscience and Remote Sensing Symposium (IGARSS) held 2000, Adama, Ethiopia. 4901-4904.

Atzberger C 2013. Advances in remote sensing of agriculture: Context description, existing operational monitoring systems and major information needs. *Remote Sensing* 5(2): 949-981.

Azar R, Villa P, Stroppiana D, Crema A, Boschetti M & Brivio PA 2016. Assessing in-season crop classification performance using satellite data: A test case in Northern Italy. *European Journal of Remote Sensing* 49(1): 361-380.

Bai T, Li D, Sun K, Chen Y & Li W 2016. Cloud detection for high-resolution satellite imagery using machine learning and multi-feature fusion. *Remote Sensing* 8(9): 715.

Balaguer A, Ruiz LA, Hermosilla T & Recio JA 2010. Definition of a comprehensive set of texture semivariogram features and their evaluation for object-oriented image classification. *Computers & Geosciences* 36(2): 231-240.

Balasubramanian 2017. Identifying the most important spectral and textural features to map specific crops with very high-resolution images. Master's thesis. Twente: University of Twente, Department of Geo-Information Science and Earth Observation.

Bannari A, Pacheco A, Staenz K, McNairn H & Omari K 2006. Estimating and mapping crop residues cover on agricultural lands using hyperspectral and IKONOS data. *Remote Sensing of Environment* 104(4): 447-459.

Barrett EC 2013. *Introduction to environmental remote sensing*. Routledge.

Basso B, Cammarano D & De Vita P 2004. Remotely sensed vegetation indices: Theory and applications for crop management. *Rivista Italiana di Agrometeorologia* 1(5): 36-53.

Bauer ME & Cipra JE 1973. Identification of agricultural crops by computer processing of ERTS MSS data. Technical Report. Indiana: The laboratory for applications of remote sensing.

Belgiu M & Csillik O 2018. Sentinel-2 cropland mapping using pixel-based and object-based time-weighted dynamic time warping analysis. *Remote Sensing of Environment* 204: 509-523.

Beyer F, Jarmer T & Siegmann B 2015. Identification of agricultural crop types in northern Israel using multitemporal rapideye data. *Photogrammetry, Remote Sensing and Geoinformation* 2015(1): 21-32.

Biggs TW, Thenkabail PS, Gumma MK, Scott CA, Parthasaradhi GR & Turral HN 2006. Irrigated area mapping in heterogeneous landscapes with MODIS time series, ground truth and census data, Krishna Basin, India. *International Journal of Remote Sensing* 27(19): 4245-4266.

Blaes X, Vanhalle L & Defourny P 2005. Efficiency of crop identification based on optical and SAR image time series. *Remote Sensing of Environment* 96(3-4): 352-365.

Bolton DK & Friedl MA 2013. Forecasting crop yield using remotely sensed vegetation indices and crop phenology metrics. *Agricultural and Forest Meteorology* 173:74-84.

Boryan C, Yang Z, Mueller R, & Craig M 2011. Monitoring US agriculture: The US department of agriculture, national agricultural statistics service, cropland data layer program. *Geocarto International* 26(5): 341-358.

Bradski G 2000. The OpenCV library. *Dr. Dobb's Journal of Software Tools* 25(120): 122-125.

Bradski GR & Pisarevsky V 2000. *Intel's Computer Vision Library: Applications in calibration, stereo segmentation, tracking, gesture, face and object recognition*. In Computer Vision and Pattern Recognition. Proceedings. IEEE Conference held 2000 in Head Island. 796-797.

Branca G, McCarthy N, Lipper L & Jolejole MC 2011. Climate-smart agriculture: A synthesis of empirical evidence of food security and mitigation benefits from improved cropland management. *Mitigation of Climate Change in Agriculture Series* 3:1-42.

Breiman L 2001. Random forests. *Machine Learning* 45(1): 5-32.

Breiman L, Friedman J, Stone CJ & Olshen RA 1984. *Classification and regression trees*. Wadsworth, Belmont: CRC Press.

Brems E, Lissens G & Veroustraete F 2000. MC-FUME: A new method for compositing individual reflective channels. *IEEE Transactions on Geoscience and Remote Sensing* 38(1): 553-569.

Broge NH & Mortensen JV 2002. Deriving green crop area index and canopy chlorophyll density of winter wheat from spectral reflectance data. *Remote Sensing of Environment* 81(1): 45-57.

Brown JC, Kastens JH, Coutinho AC, De Castro Victoria D & Bishop CR 2013. Classifying multiyear agricultural land use data from Mato Grosso using time-series MODIS vegetation index data. *Remote Sensing of Environment* 130: 39-50.

Brown M, Lewis HG & Gunn SR 2000. Linear spectral mixture models and support vector machines for remote sensing. *IEEE Transactions on Geoscience and Remote Sensing* 38(5): 2346-2360.

Cabral A, De Vasconcelos MJ, Pereira JM, Bartholomé É & Mayaux P 2003. Multi-temporal compositing approaches for SPOT-4 VEGETATION. *International Journal of Remote Sensing* 24(16): 3343-3350.

Cai Y, Guan K, Peng J, Wang S, Seifert C, Wardlow B & Li Z 2018. A high-performance and in-season classification system of field-level crop types using time-series Landsat data and a machine learning approach. *Remote Sensing of Environment* 210: 35-47.

Campbell J 2007. *Introduction to remote sensing*. 4th ed. London: Taylor & Francis.

Campbell JB & Wynne RH 2011. *Introduction to remote sensing*. Guilford Press.

Castillejo-González IL, López-Granados F, García-Ferrer A, Peña-Barragán JM, Jurado-Expósito M, De la Orden MS & González-Audicana M 2009. Object- and pixel-based analysis for

mapping crops and their agro-environmental associated measures using QuickBird imagery. *Computers and Electronics in Agriculture* 68(2): 207-215.

Chang CC 2011. "LIBSVM: A library for support vector machines. *ACM Transactions on Intelligent Systems and Technology* 2(27): 1-27.

Chen Y, Lu D, Moran E, Batistella M, Dutra LV, Sanches IDA, Da Silva RFB, Huang J, Luiz AJB & De Oliveira MAF 2018. Mapping croplands, cropping patterns, and crop types using MODIS time-series data. *International Journal of Applied Earth Observation and Geoinformation* 69: 133-147.

Chuvieco E & Huete A 2010. *Fundamentals of satellite remote sensing*. Boca Raton: Taylor & Francis Group.

Cihlar J, Manak D & Voisin N 1994. AVHRR bidirectional reflectance effects and compositing. *Remote Sensing of Environment* 48(1): 77-88.

Cohen Y & Shoshany M 2002. A national knowledge-based crop recognition in Mediterranean environment. *International Journal of Applied Earth Observation and Geoinformation* 4(1): 75-87.

Congalton RG 1991. A review of assessing the accuracy of classifications of remotely sensed data. *Remote Sensing of Environment* 37(1): 35-46.

Congalton RG & Green K 2002. *Assessing the accuracy of remotely sensed data: principles and practices*. CRC press.

Congalton RG & Green K 2008. *Assessing the accuracy of remotely sensed data: Principles and practices.* 2nd ed. Boca Raton FL: CRC Press.

Conrad C, Fritsch S, Zeidler J, Rücker G & Dech S 2010. Per-field irrigated crop classification in arid Central Asia using SPOT and ASTER data. *Remote Sensing* 2(4): 1035-1056.

Crippen RE 1990. Calculating the vegetation index faster. *Remote Sensing of Environment* 34(1): 71-73.

Cruz-Cárdenas G, López-Mata L, Villaseñor JL & Ortiz E 2014. Potential species distribution modeling and the use of principal component analysis as predictor variables. *Revista Mexicana de Biodiversidad* 85(1): 189-199.

DAFF [Department of Agriculture, Forestries and Fisheries] 2018. Plant Production - Brochures and Production guidelines. Available from: http://www.daff.gov.za/daffweb3/Branches/Agricultural-Production-Health-Food-Safety/Plant-Production/Production-Guidelines.

De Carvalho LM, Acerbi FW, Clevers JG, Fonseca LM & De Jong SM 2004. Multiscale feature extraction from images using wavelets. In *Remote sensing image analysis: Including the spatial domain* (237-270). Springer, Dordrecht.

De Colstoun ECB, Story MH, Thompson C, Commisso K, Smith TG & Irons JR 2003. National Park vegetation mapping using multitemporal Landsat-7 data and a decision tree classifier. *Remote Sensing of Environment* 85(3): 316-327.

De Jong SM & Van der Meer FD (eds) 2007. *Remote sensing image analysis: Including the spatial domain*. Springer Science & Business Media.

De Wasseige C, Vancutsem C & Defourny P 2000. *Sensitivity analysis of compositing strategies: Modelling and experimental investigations.* In Proceedings of Vegetation 2000 held 3-6 April 2000, Lake Maggiore, Italy. Université catholique de Louvain: Department of Environmental Science.

Del Frate F, Ferrazzoli P & Schiavon G 2003. Retrieving soil moisture and agricultural variables by microwave radiometry using neural networks. *Remote Sensing of Environment* 84(2): 174-183.

Delegido J, Alonso L, González G & Moreno J 2010. Estimating chlorophyll content of crops from hyperspectral data using a normalized area over reflectance curve (NAOC). *International Journal of Applied Earth Observation and Geoinformation* 12(3):165-174.

Dennison PE, Roberts DA & Peterson SH 2007. Spectral shape-based temporal compositing algorithms for MODIS surface reflectance data. *Remote Sensing of Environment* 109(4): 510-522.

D'Iorio M 1991. Effect of the calibration of AVHRR data on the normalized difference vegetation index and compositing. *Canadian Journal of Remote Sensing* 17(3): 251-262.

Diwakar PG, Prabhakar P, Venkataramana I & Devarajan R 1989. Derivation of maximum value composite images using multidate NOAA-AVHRR data. *Journal of the Indian Society of Remote Sensing* 17(1): 1-6.

Doraiswamy PC, Sinclair TR, Hollinger S, Akhmedov B, Stern A & Prueger J 2005. Application of MODIS derived parameters for regional crop yield assessment. *Remote Sensing of Environment* 97(2): 192-202.

Drusch M, Del Bello U, Carlier S, Colin O, Fernandez V, Gascon F, Hoersch B, Isola C, Laberinti P, Martimort P & Meygret A 2012. Sentinel-2: ESA's optical high-resolution mission for GMES operational services. *Remote Sensing of Environment* 120: 25-36.

Du Y, Cihlar J, Beaubien J & Latifovic R 2001. Radiometric normalization, compositing, and quality control for satellite high-resolution image mosaics over large areas. *IEEE Transactions on Geoscience and Remote Sensing* 39(3): 0196-2892.

Duro DC, Franklin SE & Dubé MG 2012. A comparison of pixel-based and object-based image analysis with selected machine learning algorithms for the classification of agricultural landscapes using SPOT-5 HRG imagery. *Remote Sensing of Environment* 118: 259-272.

Eitel JUH, Long DS, Gessler PE & Smith AMS 2007. Using in- situ measurements to evaluate the new RapidEye™ satellite series for prediction of wheat nitrogen status. *International Journal of Remote Sensing* 28(18): 4183-4190.

Eitel JU, Vierling LA, Litvak ME, Long DS, Schulthess U, Ager AA, Krofcheck DJ & Stoscheck L 2011. Broadband, red-edge information from satellites improves early stress detection in a New Mexico conifer woodland. *Remote Sensing of Environment* 115(12): 3640-3646.

Elvidge CD & Chen Z 1995. Comparison of broad-band and narrow-band red and near-infrared vegetation indices. *Remote Sensing of Environment* 54(1): 38-48.

Esetlili MT, Balcik FB, Sanl FB, Kalkan K, Ustuner M, Goksel C, Gazioğlu C & Kurucu Y 2018. Comparison of object and pixel-based classifications for mapping crops using Rapideye imagery: A case study of Menemen Plain, Turkey. *International Journal of Environment and Geoinformatics* 5(2): 231-243.

Flood N 2013. Seasonal composite Landsat TM/ETM+ images using the medoid (a multi-dimensional median). *Remote Sensing* 5(12): 6481-6500.

Foerster S, Kaden K, Foerster M & Itzerott S 2012. Crop type mapping using spectral–temporal profiles and phenological information. *Computers and Electronics in Agriculture* 89: 30-40.

Foley JA, Ramankutty N, Brauman KA, Cassidy ES, Gerber JS, Johnston M, Mueller ND, O'Connell C, Ray DK, West PC & Balzer C 2011. Solutions for a cultivated planet. *Nature* 478(7369): 337.

Foody GM 2002. Status of land cover classification accuracy assessment. *Remote Sensing of Environment* 80(1): 185-201.

Foody G & Atkinson P 2002. *Uncertainty in remote sensing and GIS*. Chichester: Wiley.

Foody GM & Mathur A 2004. A relative evaluation of multiclass image classification by support vector machines. *IEEE Transactions on Geoscience and Remote Sensing* 42(6): 1335-1343.

Forkuor G, Conrad C, Thiel M, Ullmann T & Zoungrana E 2014. Integration of optical and synthetic aperture radar imagery for improving crop mapping in Northwestern Benin, West Africa. *Remote Sensing* 6(7): 6472-6499.

Fraser AD, Massom RA & Michael KJ 2009. A method for compositing polar MODIS satellite images to remove cloud cover for landfast sea-ice detection. *IEEE Transactions on Geoscience and Remote Sensing* 47(9): 3272-3282.

Friedl MA, Sulla-Menashe D, Tan B, Schneider A, Ramankutty N, Sibley A & Huang X 2010. MODIS Collection 5 global land cover: Algorithm refinements and characterization of new datasets. *Remote Sensing of Environment* 114(1): 168-182.

Galoppo A, Castellani C & Carriero F 2018. *Sentinel-2 products specification document*. Proceedings of the international conference on AI, Simulation, and Planning in High Autonomy Systems held March 2018, Berlin, Heidelberg: Springer.

Gao J, Hu Y, Liu J & Yang R 2009. Unsupervised learning of high-order structural semantics from images. In *2009 IEEE 12th International Conference on Computer Vision* 2122-2129.

Gatti A, Galoppo A, Castellani C, Carriero F 2018. Sentinel-2 Products Specification Document [online]. Available from: https://sentinel.esa.int/documents/247904/685211/Sentinel-2-Products-Specification-Document [Accessed 2 February 2019].

Ghosh SM & Behera MD 2018. Aboveground biomass estimation using multi-sensor data synergy and machine learning algorithms in a dense tropical forest. *Applied Geography* 96: 29-40.

Gibson PJ 2000. *Introductory remote sensing: Principles and concepts.* London: Routledge.

Gilbertson JK 2017. Machine learning for object-based crop classification using multi-temporal Landsat-8 imagery. Master's Thesis. Stellenbosch: Stellenbosch University, Department of Geography and Environmental Studies.

Gilbertson JK, Kemp J & Van Niekerk A 2017. Effect of pan-sharpening multi-temporal Landsat-8 imagery for crop type differentiation using different classification techniques. *Computers and Electronics in Agriculture* 134:151-159.

Gilbertson JK & Van Niekerk A 2017. Value of dimensionality reduction for crop differentiation with multi-temporal imagery and machine learning. *Computers and Electronics in Agriculture* 142: 50-58.

Gitelson AA, Kaufman YJ & Merzlyak MN 1996. Use of a green channel in remote sensing of global vegetation from EOS-MODIS. *Remote Sensing of Environment* 58(3): 289-298.

Gitelson AA & Merzlyak MN 1998. Remote sensing of chlorophyll concentration in higher plant leaves. *Advances in Space Research* 22(5): 689-692.

Govender M, Chetty K & Bulcock H 2007. A review of hyperspectral remote sensing and its application in vegetation and water resource studies. *Water SA* 33(2).

Grandoni D 2018. *Advantages and limitations of using satellite images for flood mapping*. Proceedings of the workshop on the use of the Copernicus emergency service for floods held January 2018. Brussel.

Gumbricht T, McCarthy J & Mahlander C 1996. Digital interpretation and management of land cover—a case study of Cyprus. *Ecological Engineering* 6(4): 273-279.

Gumma MK, Nelson A, Thenkabail PS & Singh AN 2011. Mapping rice areas of South Asia using MODIS multitemporal data. *Journal of Applied Remote Sensing* 5(1): 053547.

Hagolle O, Nicolas JM, Fougnie B, Cabot F & Henry P 2004. Absolute calibration of VEGETATION derived from an interband method based on the sun glint over ocean. *IEEE Transactions on Geoscience and Remote Sensing* 42(7): 1472-1481.

Han Y, Bovolo F & Lee WH 2017. Automatic cloud-free image generation from high-resolution multitemporal imagery. *Journal of Applied Remote Sensing* 11(2): 025005.

Hao P, Zhan Y, Wang L, Niu Z & Shakir M 2015. Feature selection of time-series MODIS data for early crop classification using random forest: A case study in Kansas, USA. *Remote Sensing* 7(5): 5347-5369.

Haralick RM & Shanmugam K 1973. Textural features for image classification. *IEEE Transactions on Systems, Man, and Cybernetics* 6: 610-621.

Heinl M, Walde J, Tappeiner G & Tappeiner U 2009. Classifiers vs. input variables—The drivers in image classification for land cover mapping. *International Journal of Applied Earth Observation and Geoinformation* 11(6): 423-430.

Heller E, Rhemtulla JM, Lele S, Kalacska M, Badiger S, Sengupta R & Ramankutty N 2012. Mapping crop types, irrigated areas, and cropping intensities in heterogeneous landscapes of Southern India using multi-temporal medium-resolution imagery. *Photogrammetric Engineering & Remote Sensing* 78(8): 815-827.

Higginbottom TP, Symeonakis E, Meyer H & Van der Linden S 2018. Mapping fractional woody cover in semi-arid savannahs using multi-seasonal composites from Landsat data. *ISPRS Journal of Photogrammetry and Remote Sensing* 139: 88-102.

Hochschild V, Weise C & Selsam P 2005. The update of the digital basic map of agriculture in Thuringia with the help of remote sensing data. *Photogrammetry, Remote Sensing and Geoinformatics* 2005(3): 201.

Hodgson ME, Jensen JR, Tullis JA, Riordan KD & Archer CM 2003. Synergistic use of lidar and color aerial photography for mapping urban parcel imperviousness. *Photogrammetric Engineering & Remote Sensing* 69(9): 973-980.

Hoffer RM, Johannsen CJ & Baumgardner MF 1966. Agricultural applications of remote multispectral sensing. *Indiana Academy of Science* 76: 386-396.

Holben B 1986. Characteristics of maximum-value composite images from temporal AVHRR data. *International Journal of Remote Sensing* 7(11): 1417-1434.

Houborg R, Soegaard H & Boegh E 2007. Combining vegetation index and model inversion methods for the extraction of key vegetation biophysical parameters using Terra and Aqua MODIS reflectance data. *Remote Sensing of Environment* 106(1): 39-58.

Huang C, Wylie B, Yang L, Homer C & Zylstra 2002. Derivation of a tasseled cap transformation based on Landsat 7 at-satellite reflectance. *International Journal of Remote Sensing* 23(8): 1741-1748.

Huete AR 1988. A soil-adjusted vegetation index (SAVI). *Remote Sensing of Environment* 25(3): 295-309.

Huete AR, Justice C & Liu H 1994. Development of vegetation and soil indices for MODIS-EOS. *Remote Sensing of Environment* 49(3): 224-234.

Huete AR, Liu H & Van Leeuwen WJ 1997, August. The use of vegetation indices in forested regions: Issues of linearity and saturation. *Remote Sensing – A Scientific Vision for Sustainable Development* 4: 1966-1968.

Hunt ER, Daughtry CST, Eitel JU & Long DS 2011. Remote sensing leaf chlorophyll content using a visible band index. *Agronomy Journal* 103(4): 1090-1099.

Hüttich C, Herold M, Wegmann M, Cord A, Strohbach B, Schmullius C & Dech S 2011. Assessing effects of temporal compositing and varying observation periods for large-area land-cover mapping in semi-arid ecosystems: Implications for global monitoring. *Remote Sensing of Environment* 115(10): 2445-2459.

Immitzer M, Vuolo F & Atzberger C 2016. First experience with Sentinel-2 data for crop and tree species classifications in central Europe. *Remote Sensing* 8(3): 166.

Inglada J, Arias M, Tardy B, Hagolle O, Valero S, Morin D, Dedieu G, Sepulcre G, Bontemps S, Defourny P & Koetz B 2015. Assessment of an operational system for crop type map production using high temporal and spatial resolution satellite optical imagery. *Remote Sensing* 7(9): 12356-12379.

Inglada J, Vincent A, Arias M & Marais-Sicre C 2016. Improved early crop type identification by joint use of high temporal resolution SAR and optical image time series. *Remote Sensing* 8(5): 362.

Ippoliti- Ramilo GA, Epiphanio JCN & Shimabukuro YE 2003. Landsat- 5 Thematic Mapper data for pre- planting crop area evaluation in tropical countries. *International Journal of Remote Sensing* 24(7): 1521-1534.

Jackson RD & Huete AR 1991. Interpreting vegetation indices. *Preventive Veterinary Medicine* 11(3-4): 185-200.

Janssen LL & Vanderwel FJ 1994. Accuracy assessment of satellite derived land-cover data: A review. *Photogrammetric Engineering and Remote Sensing* 60(4).

Jay S, Lawrence R, Repasky K & Keith C 2009, March. *Invasive species mapping using low cost hyperspectral imagery.* In ASPRS 2009 Annual Conference held 9-13 March 2009, Baltimore, Maryland. Montana State University: Department of Land Resource and Environmental Science.

Jayne TS & Rashid S 2010. The value of accurate crop production forecasts: Fourth African Agricultural Markets Program (AAMP) Policy Symposium. MSU International Development Working Paper. Lilongwe, Malawi.

Jiang Z, Huete AR, Didan K & Miura T 2008. Development of a two-band enhanced vegetation index without a blue band. *Remote Sensing of Environment* 112(10): 3833-3845.

Jiao X, Kovacs JM, Shang J, McNairn H, Walters D, Ma B & Geng X 2014. Object-oriented crop mapping and monitoring using multi-temporal polarimetric RADARSAT-2 data. *ISPRS Journal of Photogrammetry and Remote Sensing* 96: 38-46.

Jolliffe IT & Cadima J 2016. Principal component analysis: A review and recent developments. *Philosophical Transactions of the Royal Society A: Mathematical, Physical and Engineering Sciences* 374(2065): 2015-0202.

Jordan CF 1969. Derivation of leaf- area index from quality of light on the forest floor. *Ecology* 50(4): 663-666.

Joshi N, Baumann M, Ehammer A, Fensholt R, Grogan K, Hostert P, Jepsen M, Kuemmerle T, Meyfroidt P, Mitchard E & Reiche J 2016. A review of the application of optical and radar remote sensing data fusion to land use mapping and monitoring. *Remote Sensing* 8(1): 70.

Karjalainen M, Kaartinen H & Hyyppä J 2008. Agricultural monitoring using Envisat alternating polarization SAR images. *Photogrammetric Engineering & Remote Sensing* 74(1): 117-126.

Karnieli A, Kaufman YJ, Remer L & Wald A 2001. AFRI—Aerosol free vegetation index. *Remote Sensing of Environment* 77(1): 10-21.

Kasischke ES, French NH, Harrell P, Christensen Jr NL, Ustin SL & Barry D 1993. Monitoring of wildfires in boreal forests using large area AVHRR NDVI composite image data. *Remote Sensing of Environment* 45(1): 61-71.

Kaufman YJ & Tanre D 1992. Atmospherically resistant vegetation index (ARVI) for EOS-MODIS. *IEEE Transactions on Geoscience and Remote Sensing* 30(2): 261-270.

Kauth RJ & Thomas GS 1976. *The tasseled cap – a graphic description of the spectral-temporal development of agricultural crops as seen by Landsat*. In LARS Symposia: 159. 1976.

Keifer JA 2014. Agricultural classification of Multi-Temporal MODIS Imagery in Northwest Argentina using Kansas crop phenologies. Master's Thesis. Portland: Portland State University, Department of Geography.

Kross A, Fernandes R, Seaquist J & Beaubien E 2011. The effect of the temporal resolution of NDVI data on season onset dates and trends across Canadian broadleaf forests. *Remote Sensing of Environment* 115(6): 1564-1575.

Kussul N, Skakun S, Shelestov A, Lavreniuk M, Yailymov B & Kussul O 2015. Regional scale crop mapping using multi-temporal satellite imagery. *The International Archives of Photogrammetry, Remote Sensing and Spatial Information Sciences* 40(7): 45.

Kussul N, Lavreniuk M, Skakun S & Shelestov A 2017. Deep learning classification of land cover and crop types using remote sensing data. *IEEE Geoscience and Remote Sensing Letters* 14(5): 778-782.

LaDue DS, Heinselman PL & Newman JF 2010. Strengths and limitations of current radar systems for two stakeholder groups in the southern plains. *Bulletin of the American Meteorological Society* 91(7): 899-910.

Lang MW, Kasisckhe ES, Prince SD & Pittman KW 2008. Assessment of C-band synthetic aperture radar data for mapping and monitoring coastal plain forested wetlands in the Mid-Atlantic Region, USA. *Remote Sensing of the Environment* 112: 4120-4130.

Lebourgeois V, Dupuy S, Vintrou É, Ameline M, Butler S & Bégué A 2017. A combined random forest and OBIA classification scheme for mapping smallholder agriculture at different nomenclature levels using multisource data (simulated Sentinel-2 time series, VHRS and DEM). *Remote Sensing* 9(3): 259.

Liang S, Li X & Wang J (eds) 2012. *Advanced remote sensing: Terrestrial information extraction and applications*. Academic Press.

Lillesand TM, Kiefer RW & Chipman JW 2004. *Remote sensing and image interpretation*. New York: John Wiley and Sons.

Lissens G, Veroustraete F & Van Rensbergen J 2000. *MC-FUME: A new method for compositing individual reflective channels*. In Proceedings of VEGETATION 2000, 2 years of operation to prepare the future. 281-285.

Liu HQ & Huete A 1995. A feedback-based modification of the NDVI to minimize canopy background and atmospheric noise. *IEEE Transactions on Geoscience and Remote Sensing* 33(2): 457-465.

Liu MW, Ozdogan M & Zhu 2013. Crop type classification by simultaneous use of satellite images of different resolutions. *IEEE Transactions on Geoscience and Remote Sensing* 52(6): 3637-3649.

Liu XH, Skidmore AK & Van Oosten H 2002. Integration of classification methods for improvement of land-cover map accuracy. *ISPRS Journal of Photogrammetry and Remote Sensing* 56(4): 257-268.

Lobser SE & Cohen WB 2007. MODIS tasselled cap: Land cover characteristics expressed through transformed MODIS data. *International Journal of Remote Sensing* 28(22): 5079-5101.

Lohmann P, Soergel U, Tavakkoli M & Farghaly D 2009. Multi-temporal classification for crop discrimination using TerraSAR-X spotlight images. *Proceedings IntArchPhRS* 38.

Long JA, Lawrence RL, Greenwood MC, Marshall L & Miller PR 2013. Object-oriented crop classification using multitemporal ETM+ SLC-off imagery and random forest. *GIScience & Remote Sensing* 50(4): 418-436.

Loughlin WP 1991. Principal component analysis for alteration mapping. *Photogrammetric Engineering and Remote Sensing* 57(9): 1163-1169.

Loveland TR, Reed BC, Brown JF, Ohlen DO, Zhu Z, Yang LWMJ & Merchant JW 2000. Development of a global land cover characteristics database and IGBP DISCover from 1 km AVHRR data. *International Journal of Remote Sensing* 21(6-7): 1303-1330.

Löw F & Duveiller G 2014. Defining the spatial resolution requirements for crop identification using optical remote sensing. *Remote Sensing* 6(9): 9034-9063.

Lu D & Weng Q 2007. A survey of image classification methods and techniques for improving classification performance. *International Journal of Remote Sensing* 28(5): 823-870.

Lück W & Van Niekerk A 2016. Evaluation of a rule-based compositing technique for Landsat-5 TM and Landsat-7 ETM+ images. *International Journal of Applied Earth Observation and Geoinformation* 47: 1-14.

Lundy C 2017. The art of the cover crop in South African vineyards. *Great Domains* 28 August: 17.

Lunetta RS, Shao Y, Ediriwickrema J & Lyon JG 2010. Monitoring agricultural cropping patterns across the Laurentian Great Lakes Basin using MODIS-NDVI data. *International Journal of Applied Earth Observation and Geoinformation* 12(2): 81-88.

Luo Y, Trishchenko AP & Khlopenkov KV 2008. Developing clear-sky, cloud and cloud shadow mask for producing clear-sky composites at 250-meter spatial resolution for the seven MODIS land bands over Canada and North America. *Remote Sensing of Environment* 112(12): 4167-4185.

Lussem U, Hüttish C & Waldhoff G 2016. Combined analysis of sentinel-1 and rapideye data for improved crop type classification: An early season approach for rapeseed and cereals. *International Archives of the Photogrammetry, Remote Sensing & Spatial Information Sciences* 41.

Ma L, Li M, Ma X, Cheng L, Du P & Liu Y 2017. A review of supervised object-based land-cover image classification. *ISPRS Journal of Photogrammetry and Remote Sensing* 130: 277-293.

Maccherone B & Frazier S 2010. *MODIS Specifications*. MODIS WEB [online]. Available from http://modis.gsfc.nasa.gov/about/media.php. [Accessed 15 September 2018]

Malan GJ 2016. Investigating the suitability of land type information for hydrological modelling in the mountain regions of Hessequa, South Africa. Master's thesis. Stellenbosch: Stellenbosch University, Department of Soil Sciences.

Massey R, Sankey TT, Congalton RG, Yadav K, Thenkabail PS, Ozdogan M & Meador AJS 2017. MODIS phenology-derived, multi-year distribution of conterminous US crop types. *Remote Sensing of Environment* 198: 490-503.

Mather PM 2004. *Computer processing of remotely-sensed images: An introduction*. Chichester: Wiley.

Mather P & Magaly K 2011. *Computer processing of remotely-sensed images*. 4th ed. Chichester: John Wiley & Sons.

Mathur A & Foody GM 2008. Crop classification by support vector machine with intelligently selected training data for an operational application. *International Journal of Remote Sensing* 29(8): 2227-2240.

Matton N, Canto G, Waldner F, Valero S, Morin D, Inglada J, Arias M, Bontemps S, Koetz B & Defourny P 2015. An automated method for annual cropland mapping along the season for various globally-distributed agrosystems using high spatial and temporal resolution time series. *Remote Sensing* 7(10): 13208-13232.

Maxwell SK & Sylvester KM 2012. Identification of "ever-cropped" land (1984–2010) using Landsat annual maximum NDVI image composites: South western Kansas case study. *Remote Sensing of Environment* 121: 186-195.

McNairn H, Champagne C, Shang J, Holmstrom D & Reichert G 2009. Integration of optical and Synthetic Aperture Radar (SAR) imagery for delivering operational annual crop inventories. *ISPRS Journal of Photogrammetry and Remote Sensing* 64(5): 434-449.

McNairn H, Kross A, Lapen D, Caves R & Shang J 2014. Early season monitoring of corn and soybeans with TerraSAR-X and RADARSAT-2. *International Journal of Applied Earth Observation and Geoinformation* 28: 252-259.

Meyer D, Verstraete M & Pinty B 1995. The effect of surface anisotropy and viewing geometry on the estimation of NDVI from AVHRR. *Remote Sensing Reviews* 12(1-2): 3-27.

Mingwei Z, Qingbo Z, Zhongxin C, Jia L, Yong Z & Chongfa C 2008. Crop discrimination in Northern China with double cropping systems using Fourier analysis of time-series MODIS data. *International Journal of Applied Earth Observation and Geoinformation* 10(4): 476-485.

Mountrakis G, Im J & Ogole C 2011. Support vector machines in remote sensing: A review. *ISPRS Journal of Photogrammetry and Remote Sensing* 66(3): 247-259.

Muhd-Ekhzarizal ME, Mohd-Hasmadi I, Hamdan O, Mohamad-Roslan MK & Noor-Shaila S 2018. Estimation of aboveground biomass in mangrove forests using vegetation indices from SPOT-5 image. *Journal of Tropical Forest Science* 30(2): 224-233.

Muller SJ 2017. Indirect soil salinity detection in irrigated areas using earth observation methods. Master's thesis. Stellenbosch: Stellenbosch University, Department of Geography and Environmental Studies.

Murakami T, Ogawa S, Ishitsuka N, Kumagai K & Saito G 2001. Crop discrimination with multitemporal SPOT/HRV data in the Saga Plains, Japan. *International Journal of Remote Sensing* 22(7): 1335-1348.

Murthy CS, Raju PV & Badrinath KVS 2003. Classification of wheat crop with multi-temporal images: Performance of maximum likelihood and artificial neural networks. *International Journal of Remote Sensing* 24(23): 4871-4890.

Myburgh G 2012. The impact of training set size and feature dimensionality on supervised object-based classification: A comparison of three classifiers. Master's Thesis. Stellenbosch: Stellenbosch University, Department of Geography and Environmental Studies.

Myburgh G & Van Niekerk A 2013. Effect of feature dimensionality on object-based land cover classification: A comparison of three classifiers. *South African Journal of Geomatics* 2(1): 13-27.

Myint SW, Gober P, Brazel A, Grossman-Clarke S & Weng Q 2011. Per-pixel vs. object-based classification of urban land cover extraction using high spatial resolution imagery. *Remote Sensing of Environment* 115(5): 1145-1161.

Nangendo G, Skidmore AK & Van Oosten H 2007. Mapping East African tropical forests and woodlands − a comparison of classifiers. *ISPRS Journal of Photogrammetry and Remote Sensing* 61(6): 393-404.

Neinavaz E, Darvishzadeh R, Skidmore AK & Groen TA 2016. Measuring the response of canopy emissivity spectra to leaf area index variation using thermal hyperspectral data. *International Journal of Applied Earth Observation and Geoformation* 53: 40-47.

Nellis MD, Price KP & Rundquist D 2009. Remote sensing of cropland agriculture. *The SAGE Handbook of Remote Sensing* 1: 368-380.

Nigam R, Vyas SS, Bhattacharya BK, Oza MP, Srivastava SS, Bhagia N, Dhar D & Manjunath KR 2015. Modeling temporal growth profile of vegetation index from Indian geostationary

satellite for assessing in-season progress of crop area. *GIScience & Remote Sensing* 52(6): 723-745.

Nigam R, Tripathy R, Dutta S, Bhagia N, Nagori R, Chandrasekar K, Kot R, Bhattacharya BK & Ustin S 2019. Crop type discrimination and health assessment using hyperspectral imaging. *Current Science* (00113891) 116(7).

Nitze I, Schulthess U & Asche H 2012. *Comparison of machine learning algorithms random forest, artificial neural network and support vector machine to maximum likelihood for supervised crop type classification.* Proceedings of the 4th GEOBIA held 7-9 May 2012, Rio de Janeiro, Brazil. University of Potsdam, Department of Geography.

Nolin AW & Payne MC 2007. Classification of glacier zones in Western Greenland using albedo and surface roughness from the Multi-angle Imaging SpectroRadiometer (MISR). *Remote Sensing of the Environment* 107: 264-275.

Oetter DR, Cohen WB, Berterretche M, Maiersperger TK & Kennedy RE 2001. Land cover mapping in an agricultural setting using multiseasonal Thematic Mapper data. *Remote Sensing of Environment* 76(2): 139-155.

Ogunbadewa EY 2012. Investigating availability of cloud-free images with cloud masks in relation to satellite revisit frequency in the Northwest of England. *Contributions Geophysics Geodesy* 42: 63-100.

Oyekola MA & Adewuyi GK 2018. Unsupervised classification in land cover types using remote sensing and GIS techniques. *International Journal of Science and Engineering Investigations* 7(72): 2251-8843.

Ozdarici-Ok A, Ok A & Schindler K 2015. Mapping of agricultural crops from single high-resolution multispectral images—Data-driven smoothing vs. parcel-based smoothing. *Remote Sensing* 7(5): 5611-5638.

Ozdogan M & Woodcock CE 2006. Resolution dependent errors in remote sensing of cultivated areas. *Remote Sensing of Environment* 103(2): 203-217.

Pacheco A & McNairn H 2010. Evaluating multispectral remote sensing and spectral unmixing analysis for crop residue mapping. *Remote Sensing of Environment* 114(10): 2219-2228.

Pahlevan N, Sarkar S, Franz BA, Balasubramanian SV & He J 2017. Sentinel-2 MultiSpectral Instrument (MSI) data processing for aquatic science applications: Demonstrations and validations. *Remote Sensing of Environment* 201: 47-56.

Pal M & Mather PM 2003. An assessment of the effectiveness of decision tree methods for land cover classification. *Remote Sensing of Environment* 86(4): 554-565.

Palchowdhuri Y, Valcarce-Diñeiro R, King P & Sanabria-Soto M 2018. Classification of multi-temporal spectral indices for crop type mapping: A case study in Coalville, UK. *The Journal of Agricultural Science* 156(1): 24-36.

Peña J, Gutiérrez P, Hervás-Martínez C, Six J, Plant R & López-Granados F 2014. Object-based image classification of summer crops with machine learning methods. *Remote Sensing* 6(6): 5019-5041.

Peña-Barragán JM, López-Granados F, García-Torres L, Jurado-Expósito M, De La Orden MS & García-Ferrer A 2008. Discriminating cropping systems and agro-environmental measures by remote sensing. *Agronomy for Sustainable Development* 28(2): 355-362.

Peña-Barragán JM, Ngugi MK, Plant RE & Six J 2011. Object-based crop identification using multiple vegetation indices, textural features and crop phenology. *Remote Sensing of Environment* 115(6): 1301-1316.

Peters AJ, Walter-Shea EA, Ji L, Vina A, Hayes M & Svoboda MD 2002. Drought monitoring with NDVI-based standardized vegetation index. *Photogrammetric Engineering and Remote Sensing* 68(1): 71-75.

Potter CS & Brooks V 2000. Global analysis of empirical relations between annual climate and seasonality of NDVI. *International Journal of Remote Sensing* 19(15): 2921-2948.

Pouliot D, Latifovic R, Fernandes R & Olthof I 2011. Evaluation of compositing period and AVHRR and MERIS combination for improvement of spring phenology detection in deciduous forests. *Remote Sensing of Environment* 115(1): 158-166.

Prasad AM, Iverson LR & Liaw A 2006. Newer classification and regression tree techniques: Bagging and random forests for ecological prediction. *Ecosystems* 9(2): 181-199.

Qi J 1993. Compositing multitemporal remote sensing data. Doctoral dissertation. Arizona: University of Arizona, Department of Oil and Water Science.

Qi J & Kerr Y 1997. On current compositing algorithms. *Remote Sensing Reviews* 15(1-4): 235-256.

Ramoelo A, Skidmore AK, Cho MA, Schlerf M, Mathieu R & Heitkönig IM (2012). Regional estimation of savanna grass nitrogen using the red-edge band of the spaceborne RapidEye sensor. *International Journal of Applied Earth Observation and Geoinformation* 19: 151-162.

Ranjan R, Chandel AK, Khot LR, Bahlol HY, Zhou J, Boydston RA & Miklas PN 2019. Irrigated pinto bean crop stress and yield assessment using ground based low altitude remote sensing technology. *Information Processing in Agriculture* [online]. Available from https://doi.org/10.1016/j.inpa.2019.01.005. [Accessed 10 March 2017.

Roberts D, Mueller N & Mcintyre A 2017. High-dimensional pixel composites from earth observation time series. *IEEE Transactions on Geoscience and Remote Sensing* 55(11): 6254-6264.

Rodriguez-Galiano VF, Ghimire B, Rogan J, Chica-Olmo M & Rigol-Sanchez JP 2012. An assessment of the effectiveness of a random forest classifier for land-cover classification. *ISPRS Journal of Photogrammetry and Remote Sensing* 67: 93-104.

Rosina K & Kopecká M 2016. *Mapping of urban green spaces using Sentinel-2A data: Methodical aspects.* In 6th International Conference on Cartography and GIS held 13-17 June 2016, Albena, Bulgaria. Bulgarian Cartographic Association.

Roteta E, Bastarrika A, Padilla M, Storm T & Chuvieco E 2019. Development of a Sentinel-2 burned area algorithm: Generation of a small fire database for sub-Saharan Africa. *Remote Sensing of Environment* 222: 1-17.

Rouse JW 1974. *Monitoring the vernal advancement of retrogradation of natural vegetation*. Publication No 371/1974. NASA/GSFG.

Roy A, Kucukural A & Zhang Y 2010. I-TASSER: A unified platform for automated protein structure and function prediction. *Nature Protocols* 5(4): 725.

Rozenstein O & Karnieli A 2011. Comparison of methods for land-use classification incorporating remote sensing and GIS inputs. *Applied Geography* 31(2): 533-544.

Ruiz LA, Recio JA, Fernández-Sarría A & Hermosilla T 2011. A feature extraction software tool for agricultural object-based image analysis. *Computers and Electronics in Agriculture* 76(2): 284-296.

Sabour ST, Lohmann P & Soergel U 2008. Monitoring agricultural activities using multi-temporal ASAR ENVISAT data. *International Archives of the Photogrammetry, Remote Sensing and Spatial Information Sciences* 37: 735-742.

Salehi B, Daneshfar B & Davidson AM 2017. Accurate crop-type classification using multi-temporal optical and multi-polarization SAR data in an object-based image analysis framework. *International Journal of Remote Sensing* 38(14): 4130-4155.

Samaniego L & Schulz K 2009. Supervised classification of agricultural land cover using a modified k-NN technique (MNN) and Landsat remote sensing imagery. *Remote Sensing* 1(4): 875-895.

Satir O & Berberoglu S 2016. Crop yield prediction under soil salinity using satellite derived vegetation indices. *Field Crops Research* 192: 134-143.

Schmedtmann J & Campagnolo M 2015. Reliable crop identification with satellite imagery in the context of common agriculture policy subsidy control. *Remote Sensing* 7(7): 9325-9346.

Schuster C, Förster M & Kleinschmit B 2012. Testing the red-edge channel for improving land-use classifications based on high-resolution multi-spectral satellite data. *International Journal of Remote Sensing* 33(17): 5583-5599.

Sedano F, Kempeneers P, Strobl P, Kucera J, Vogt P, Seebach L & San-Miguel-Ayanz J 2011. A cloud mask methodology for high-resolution remote sensing data combining information from high and medium resolution optical sensors. *ISPRS Journal of Photogrammetry and Remote Sensing* 66(5): 588-596.

Shao Y, Lunetta RS, Ediriwickrema J & Iiames J 2010. Mapping cropland and major crop types across the Great Lakes Basin using MODIS-NDVI data. *Photogrammetric Engineering & Remote Sensing* 76(1): 73-84.

Shao Y & Lunetta RS 2012. Comparison of support vector machine, neural network, and CART algorithms for the land-cover classification using limited training data points. *ISPRS Journal of Photogrammetry and Remote Sensing* 70: 78-87.

Shelestov A, Lavreniuk M, Kussul N, Novikov A & Skakun S 2017. Exploring Google Earth Engine platform for big data processing: Classification of multi-temporal satellite imagery for crop mapping. *Frontiers in Earth Science* 5: 17.

Shewalkar P, Khobragade A & Jajulwar K 2014. Review paper on crop area estimation using SAR remote sensing data. *IOSR Journal of Electrical and Electronics Engineering* 9: 97-98.

Siachalou S, Mallinis G & Tsakiri-Strati M 2015. A hidden Markov models approach for crop classification: Linking crop phenology to time series of multi-sensor remote sensing data. *Remote Sensing* 7(4): 3633-3650.

Simonneaux V, Duchemin B, Helson D, Er- Raki S, Olioso A & Chehbouni AG 2008. The use of high- resolution image time series for crop classification and evapotranspiration estimate over an irrigated area in central Morocco. *International Journal of Remote Sensing* 29(1): 95-116.

Sims DA, Rahman AF, Cordova VD, El-Masri BZ, Baldocchi DD, Bolstad PV, Flanagan LB, Goldstein AH, Hollinger DY, Misson L & Monson RK 2008. A new model of gross primary productivity for North American ecosystems based solely on the enhanced vegetation index and land surface temperature from MODIS. *Remote Sensing of Environment* 112(4): 1633-1646.

Singh VP, Zhang Q, Kong D & Shi P 2017. Response of vegetation to different time-scales drought across China: Spatiotemporal patterns, causes and implications. *Global and Planetary Change* 152: 1-11.

Skakun S, Franch B, Vermote E, Roger JC, Becker-Reshef I, Justice C & Kussul N 2017. Early season large-area winter crop mapping using MODIS NDVI data, growing degree-days information and a Gaussian mixture model. *Remote Sensing of Environment* 195: 244-258.

Sonobe R, Tani H, Wang X, Kobayashi N & Shimamura H 2014. Random forest classification of crop type using multi-temporal TerraSAR-X dual-polarimetric data. *Remote Sensing Letters* 5(2): 157-164.

Sonobe R, Yamaya Y, Tani H, Wang X, Kobayashi N & Mochizuki KI 2017. Assessing the suitability of data from Sentinel-1A and 2A for crop classification. *GIScience & Remote Sensing* 54(6): 918-938.

Sonobe R, Yamaya Y, Tani H, Wang X, Kobayashi N & Mochizuki KI 2018. Crop classification from Sentinel-2-derived vegetation indices using ensemble learning. *Journal of Applied Remote Sensing* 12(2): 026019.

Statistics South Africa (StatsSA) 2007. *2007 Community Survey*. Pretoria: South Africa.

Stellacci AM, Castrignanò A, Diacono M, Troccoli A, Ciccarese A, Armenise E, Gallo A, De Vita P, Lonigro A, Mastro MA & Rubino P 2012. Combined approach based on principal component analysis and canonical discriminant analysis for investigating hyperspectral plant response. *Italian Journal of Agronomy* 34:34.

Stephenson GR 2010. A comparison of supervised and rule-based object-orientated classification for forest mapping. Master's Thesis. Stellenbosch: University of Stellenbosch, Department of Geography and Environmental Studies.

Story M & Congalton RG 1986. Accuracy assessment: A user's perspective. *Photogrammetric Engineering and Remote Sensing* 52(3): 397-399.

Sun L, Wei J, Wang J, Mi X, Guo Y, Lv Y, Yang Y, Gan, P, Zhou X, Jia C & Tian X 2016. A universal dynamic threshold cloud detection algorithm (UDTCDA) supported by a prior surface reflectance database. *Journal of Geophysical Research: Atmospheres* 121(12): 7172-7196.

Sun L, Mi X, Wei J, Wang J, Tian X, Yu H & Gan P 2017. A cloud detection algorithm-generating method for remote sensing data at visible to short-wave infrared wavelengths. *ISPRS Journal of Photogrammetry and Remote Sensing* 124: 70-88.

Sun C, Bian Y, Zhou T & Pan J 2019. Using of multi-source and multi-temporal remote sensing data improves crop-type mapping in the Subtropical agriculture region. *Sensors* 19(10): 2401.

Szuster BW, Chen Q & Borger M 2011. A comparison of classification techniques to support land cover and land use analysis in tropical coastal zones. *Applied Geography* 31: 525–532.

Teluguntla P, Thenkabail P, Oliphant A, Xiong J, Gumma MK, Congalton RG, Yadav K & Huete A 2018. A 30-m landsat-derived cropland extent product of Australia and China using random forest machine learning algorithm on Google Earth Engine cloud computing platform. *ISPRS Journal of Photogrammetry and Remote Sensing* 144: 325-340.

Tempfli K, Kerle N, Huurneman GC & Janssen LLF 2009. *Principles of remote sensing*. Enschede: ITC.

Tererai F, Gaertner M, Jacobs SM & Richardson DM 2015. Resilience of invaded riparian landscapes: The potential role of soil-stored seed banks. *Environmental Management* 55(1): 86-99.

Thanh Noi P & Kappas M 2018. Comparison of random forest, k-nearest neighbor, and support vector machine classifiers for land cover classification using Sentinel-2 imagery. *Sensors* 18(1): 18.

Thenkabail PS, Mariotto I, Gumma MK, Middleton EM, Landis DR & Huemmrich KF 2013. Selection of hyperspectral narrowbands (HNBs) and composition of hyperspectral twoband vegetation indices (HVIs) for biophysical characterization and discrimination of crop types using field reflectance and Hyperion/EO-1 data. *IEEE Journal of Selected Topics in Applied Earth Observations and Remote Sensing* 6(2): 427-439.

Townshend JR & Justice CO 1986. Analysis of the dynamics of African vegetation using the normalized difference vegetation index. *International Journal of Remote Sensing* 7(11): 1435-1445.

Tucker CJ, Vanpraet CL, Sharman MJ & Van Ittersum G 1985. Satellite remote sensing of total herbaceous biomass production in the Senegalese Sahel: 1980–1984. *Remote Sensing of Environment* 17(3): 233-249.

Turner W, Spector S, Gardiner N, Fladeland M, Sterling E & Steininger M 2003. Remote sensing for biodiversity science and conservation. *Trends in Ecology & Evolution* 18(6): 306-314.

Vancutsem C, Pekel JF, Bogaert P & Defourny P 2007. Mean compositing, an alternative strategy for producing temporal syntheses. Concepts and performance assessment for SPOT VEGETATION time series. *International Journal of Remote Sensing* 28(22): 5123-5141.

Vapnik VN 1995. *The nature of statistical learning*. Theory.

Veloso A, Mermoz S, Bouvet A, Le Toan T, Planells M, Dejoux J F & Ceschia E 2017. Understanding the temporal behavior of crops using Sentinel-1 and Sentinel-2-like data for agricultural applications. *Remote Sensing of Environment* 199: 415-426.

Vuolo F, Neuwirth M, Immitzer M, Atzberger C & Ng WT 2018. How much does multi-temporal Sentinel-2 data improve crop type classification? *International Journal of Applied Earth Observation and Geoinformation* 72: 122-130.

Wardlow BD, Egbert SL & Kastens JH 2007. Analysis of time-series MODIS 250 m vegetation index data for crop classification in the US Central Great Plains. *Remote Sensing of Environment* 108(3): 290-310.

Wardlow BD & Egbert SL 2008. Large-area crop mapping using time-series MODIS 250 m NDVI data: An assessment for the US Central Great Plains. *Remote Sensing of Environment* 112(3): 1096-1116.

Waske B, Van der Linden S, Benediktsson JA, Rabe A & Hostert P 2010. Sensitivity of support vector machines to random feature selection in classification of hyperspectral data. *IEEE Transactions on Geoscience and Remote Sensing* 48(7): 2880-2889.

Watts JD & Lawrence RL 2008. Merging random forest classification with an object-oriented approach for analysis of agricultural lands. *The International Archives of the Photogrammetry, Remote Sensing and Spatial Information Sciences* 37(Pat B7): 2006-2009.

Western Cape Department of Agriculture 2018. Mapping of Agricultural Commodity production and infrastructure in the Western Cape, 2017/18-2018/19. Western Cape Department of Agriculture. Elsenburg: Directorate Agricultural Development and Support Services.

White JC, Wulder MA, Hobart GW, Luther JE, Hermosilla T, Griffiths P, Coops NC, Hall RJ, Hostert P, Dyk A & Guindon L 2014. Pixel-based image compositing for large-area dense time series applications and science. *Canadian Journal of Remote Sensing* 40(3): 192-212.

Wu B, Weng J, Li Q, Yan N, Du X & Zhang M 2014. Remote sensing-based global crop monitoring: experiences with China's CropWatch system. *International Journal of Digital Earth* 7(2): 113-137.

Xavier AC, Rudorff BF, Shimabukuro YE, Berka LMS & Moreira MA 2006. Multi- temporal analysis of MODIS data to classify sugarcane crop. *International Journal of Remote Sensing* 27(4): 755-768.

Xiao X, Boles S, Liu J, Zhuang D, Frolking S, Li C, Salas W & Moore III B 2005. Mapping paddy rice agriculture in southern China using multi-temporal MODIS images. *Remote Sensing of Environment* 95(4): 480-492.

Xiong J, Thenkabail P, Tilton J, Gumma M, Teluguntla P, Oliphant A, Congalton R, Yadav K & Gorelick N 2017. Nominal 30-m cropland extent map of continental Africa by integrating pixel-based and object-based algorithms using Sentinel-2 and Landsat-8 data on Google Earth Engine. *Remote Sensing* 9(10): 1065.

Yan L & Roy DP 2014. Automated crop field extraction from multi-temporal Web Enabled Landsat Data. *Remote Sensing of Environment* 144: 42-64.

Yang C, Everitt JH & Murden D 2011. Evaluating high-resolution SPOT 5 satellite imagery for crop identification. *Computers and Electronics in Agriculture* 75(2): 347-354.

Yang C, Odvody GN, Fernandez CJ, Landivar JA, Minzenmayer RR & Nichols RL 2015. Evaluating unsupervised and supervised image classification methods for mapping cotton root rot. *Precision Agriculture* 16(2): 201-215.

Yoder BJ & Waring RH 1994. The normalized difference vegetation index of small Douglas-fir canopies with varying chlorophyll concentrations. *Remote Sensing of Environment* 49(1): 81-91.

You H, Jianjuan X & Xin G 2016. *Radar data processing with applications*. John Wiley & Sons.

Zhang H, Li Q, Liu J, Shang J, Du X, Zhao L, Wang N & Dong T 2017. Crop classification and acreage estimation in North Korea using phenology features. *GIScience & Remote Sensing* 54(3): 381-406.

Zheng B, Myint SW, Thenkabail PS & Aggarwal RM 2015. A support vector machine to identify irrigated crop types using time-series Landsat NDVI data. *International Journal of Applied Earth Observation and Geoinformation* 34: 103-112.

Zhong G, Wang X, Tani H, Guo M, Chittenden A, Yin S, Sun Z & Matsumura S 2016. A modified aerosol free vegetation index algorithm for aerosol optical depth retrieval using GOSAT TANSO-CAI data. *Remote Sensing* 8(12): 998.

APPENDIX A

Supplementary material for Chapter 3 (Confusion matrices for the best-performing classification)

Table A-1 Formulae used for calculating VIs, the respective names, used abbreviations as well as the bands for computation

Name	Index	Formulation	Bands Used
Aerosol Free Vegetation Index (NIR, SWIR1)	AFRI1	$NIR - 0.66\frac{\text{SWIR1}}{\text{NIR} + 0.66(\text{SWIR1})}$	Band 8, Band 11
Aerosol Free Vegetation Index (NIR, SWIR2)	AFRI2	$NIR - 0.66\frac{\text{SWIR2}}{\text{NIR} + 0.66(\text{SWIR2})}$	Band 8, Band 12
Aerosol Free Vegetation Index (Narrow NIR, SWIR1)	AFRI3	$NarrowNIR - 0.66\frac{\text{SWIR1}}{\text{NIR8A} + 0.66(\text{SWIR1})}$	Band 8A, Band 11
Aerosol free vegetation Index (Narrow NIR, SWIR2)	AFRI4	$NarrowNIR - 0.66\frac{\text{SWIR2}}{\text{NIR8A} + 0.66(\text{SWIR2})}$	Band 8A, Band 12
Enhanced Vegetation Index (NIR, Vegetation Red-Edge1)	EVI1	$2.5\frac{\text{NIR}-\text{Red Edge1}}{(\text{NIR}+6\text{Red}-7.5\text{Blue})+1}$	Band 8, Band5, Band2
Enhanced Vegetation Index (NIR, Vegetation Red-Edge2)	EVI2	$2.5\frac{\text{NIR} - \text{Red Edge2}}{(\text{NIR} + 6\text{Red} - 7.5\text{Blue}) + 1}$	Band 8, Band6, Band 2
Enhanced Vegetation Index (NIR, Vegetation Red-Edge3)	EVI3	$2.5\frac{\text{NIR} - \text{Red Edge3}}{(\text{NIR} + 6\text{Red} - 7.5\text{Blue}) + 1}$	Band8, Band7, Band2
Enhanced Vegetation Index (Narrow NIR, Vegetation Red-Edge1)	EVI4	$2.5\frac{\text{Narrow NIR} - \text{Red Edge1}}{(\text{Narrow NIR} + 6\text{Red} - 7.5\text{Blue}) + 1}$	Band8A, Band5, Band2
Enhanced Vegetation Index (Narrow NIR, Vegetation Red-Edge2)	EVI5	$2.5\frac{\text{Narrow NIR} - \text{Red Edge2}}{(\text{Narrow NIR} + 6\text{Red} - 7.5\text{Blue}) + 1}$	Band8A, Band6, Band2
Enhanced Vegetation Index (Narrow NIR, Vegetation Red-Edge3)	EVI6	$2.5\frac{\text{Narrow NIR} - \text{Red Edge3}}{(\text{Narrow NIR} + 6\text{Red} - 7.5\text{Blue}) + 1}$	Band8A, Band7, Band2
Enhanced Vegetation Index (Narrow NIR, Red)	EVI7	$2.5\frac{\text{Narrow NIR} - \text{Red}}{(\text{Narrow NIR} + 6\text{Red} - 7.5\text{Blue}) + 1}$	Band8A, Band4, Band2
Enhanced Vegetation Index (Narrow NIR, Vegetation Red-Edge3)	EVI8	$2.5\frac{\text{Narrow NIR} - \text{Red Edge3}}{(\text{Narrow NIR} + 6\text{Red} - 7.5\text{Blue}) + 1}$	Band8A, Band7, Band2

Normalised Difference Moisture Index (NIR, SWIR1)	NDMI1	$\frac{\text{NIR} - \text{SWIR1}}{NIR + SWIR1}$	Band8, Band11
Normalised Difference Moisture Index (NIR, SWIR2)	NDMI2	$\frac{\text{NIR} - \text{SWIR2}}{NIR + SWIR2}$	Band8, Band12
Normalised Difference Moisture Index (Narrow NIR, SWIR1)	NDMI3	$\frac{\text{Narrow NIR} - \text{SWIR1}}{Narrow\ NIR + SWIR1}$	Band8, Band11
Normalised Difference Moisture Index (Narrow NIR, SWIR2)	NDMI4	$\frac{\text{Narrow NIR} - \text{SWIR2}}{Narrow\ NIR + SWIR2}$	Band8, Band12
Normalised Difference Vegetation Index (NIR, Red)	NDVI1	$\frac{\text{NIR}-\text{RED}}{NIR+RED}$	Band8, Band4
Normalised Difference Vegetation Index (NIR, Red)	NDVI2	$\frac{\text{Narrow NIR}-\text{RED}}{Narrow\ NIR+RED}$	Band8A, Band4
Normalised Difference Vegetation Index (NIR, Red)	NDVI3	$\frac{\text{NIR}-\text{Red Edge1}}{NIR+Red\ Edge1}$	Band8, Band5
Normalised Difference Vegetation Index (NIR, Vegetation Red-Edge2)	NDVI4	$\frac{\text{NIR}-\text{Red Edge2}}{\text{NIR+Red Edge2}}$	Band8, Band6
Normalised Difference Vegetation Index (NIR, Vegetation Red-Edge3)	NDVI5	$\frac{\text{NIR}-\text{Red Edge3}}{\text{NIR+Red Edge3}}$	Band8, Band7
Normalised Difference Vegetation Index (NIR, Vegetation Red-Edge1)	NDVI6	$\frac{\text{Narrow NIR} - \text{Red Edge1}}{\text{Narrow NIR} + \text{Red Edge1}}$	Band8A, Band5
Normalised Difference Vegetation Index (NIR, Vegetation Red-Edge2)	NDVI7	$\frac{\text{Narrow NIR}-\text{Red Edge2}}{\text{Narrow NIR+Red Edge2}}$	Band8A, Band6
Normalised Difference Vegetation Index (NIR, Vegetation Red-Edge3)	NDVI8	$\frac{\text{Narrow NIR}-\text{Red Edge3}}{\text{Narrow NIR+Red Edge3}}$	Band8A, Band7

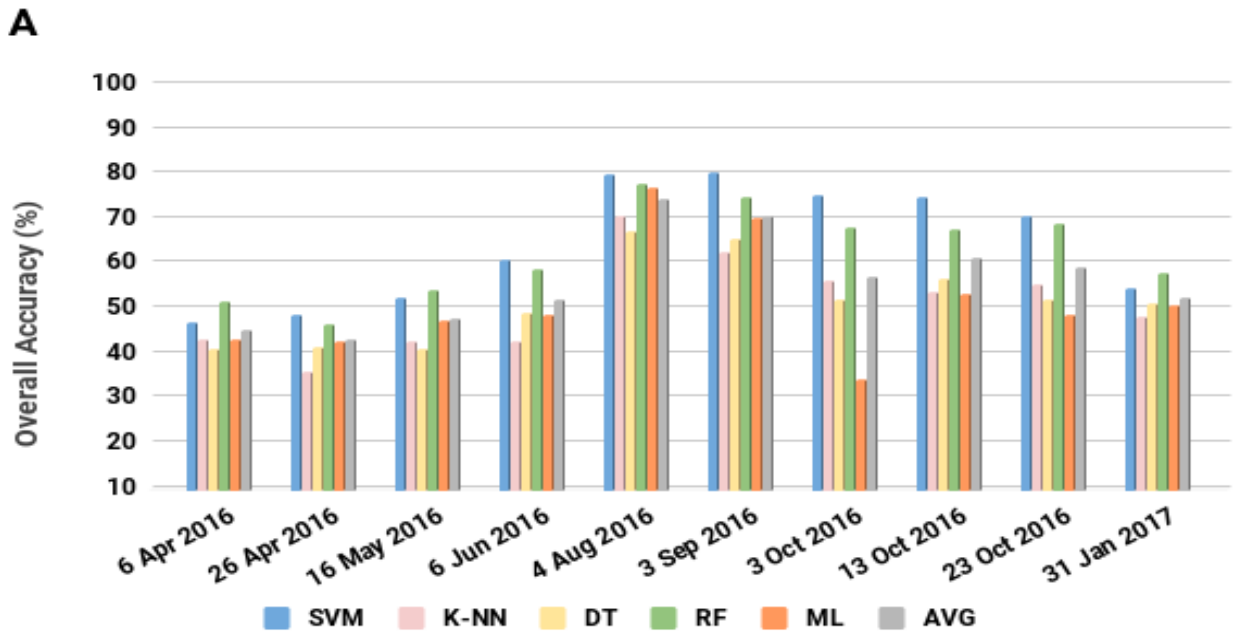

Figure A-1 Single-date Overall accuracies (OAs) and mean OAs (AVG) for all classifiers in Site A.

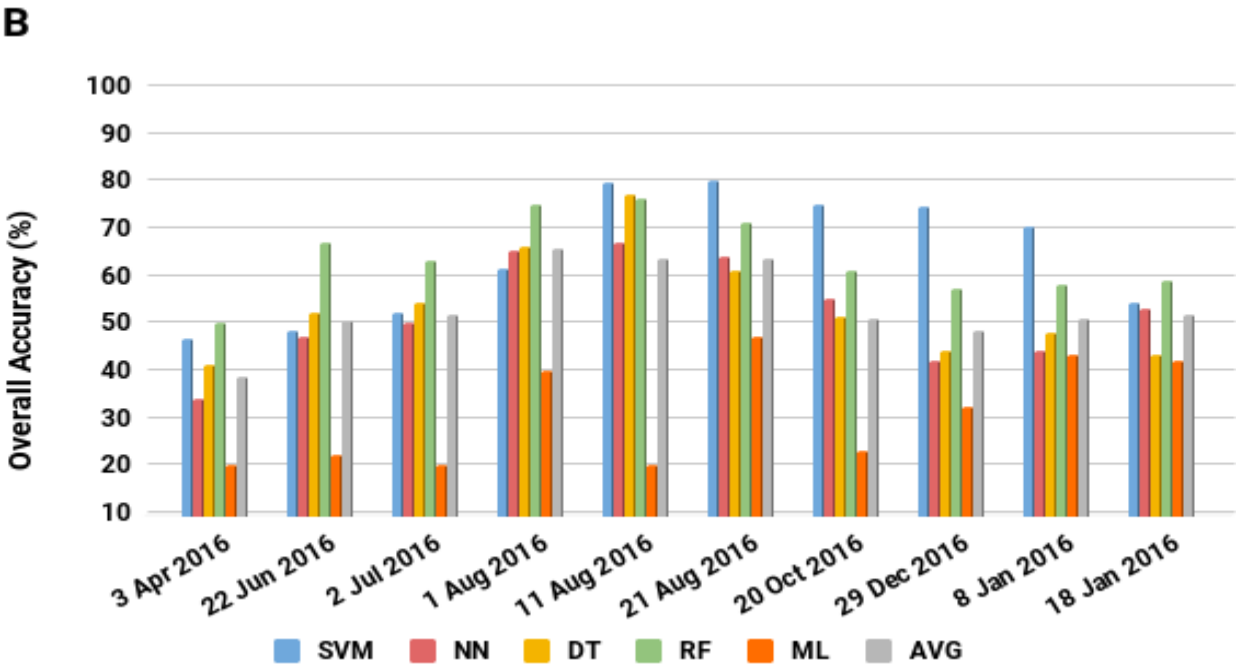

Figure A-2 Single-date Overall accuracies (OAs) and mean OAs (AVG) for all classifiers in Site B.

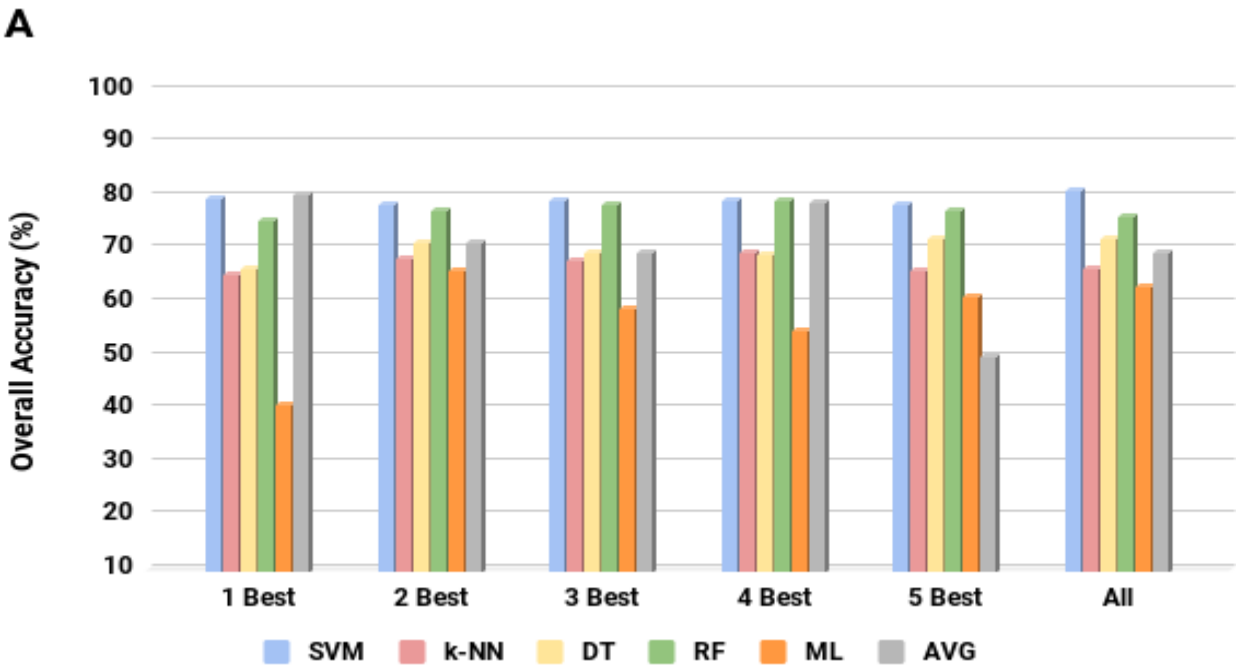

Figure A-3 Multi-temporal rank-based image set Overall accuracies (OAs) and mean OAs (AVG) for all classifiers in Site A.

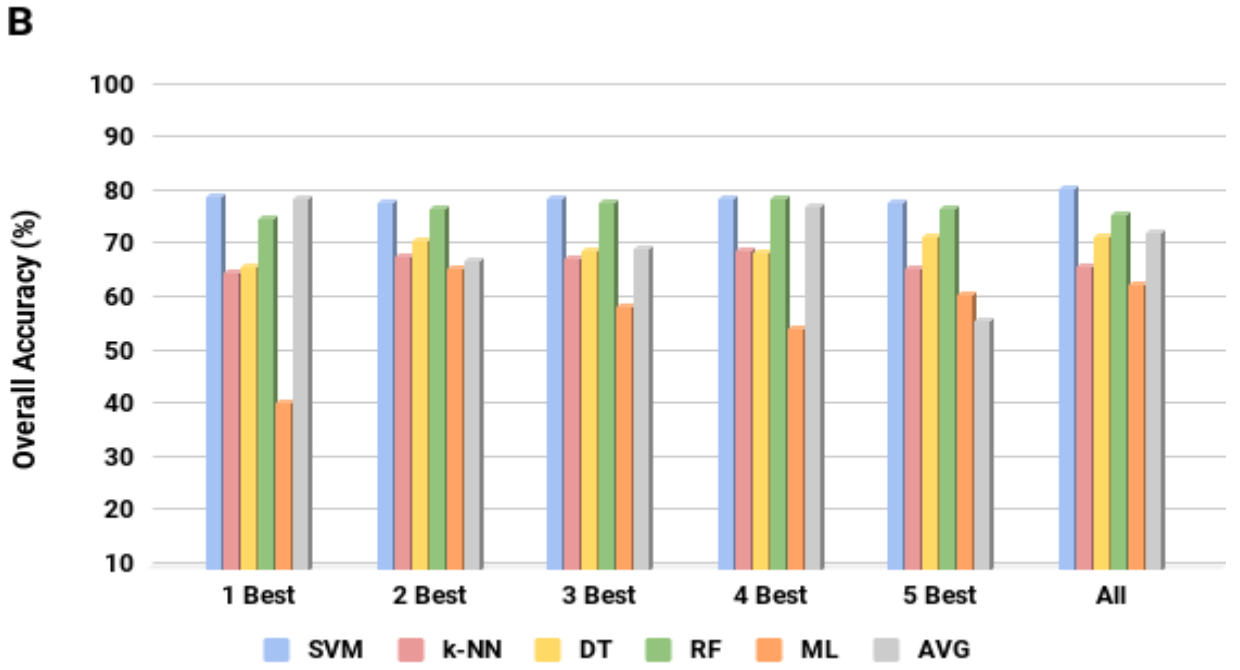

Figure A-4 Multi-temporal rank-based image set Overall accuracies (OAs) and mean OAs (AVG) for all classifiers in Site B.

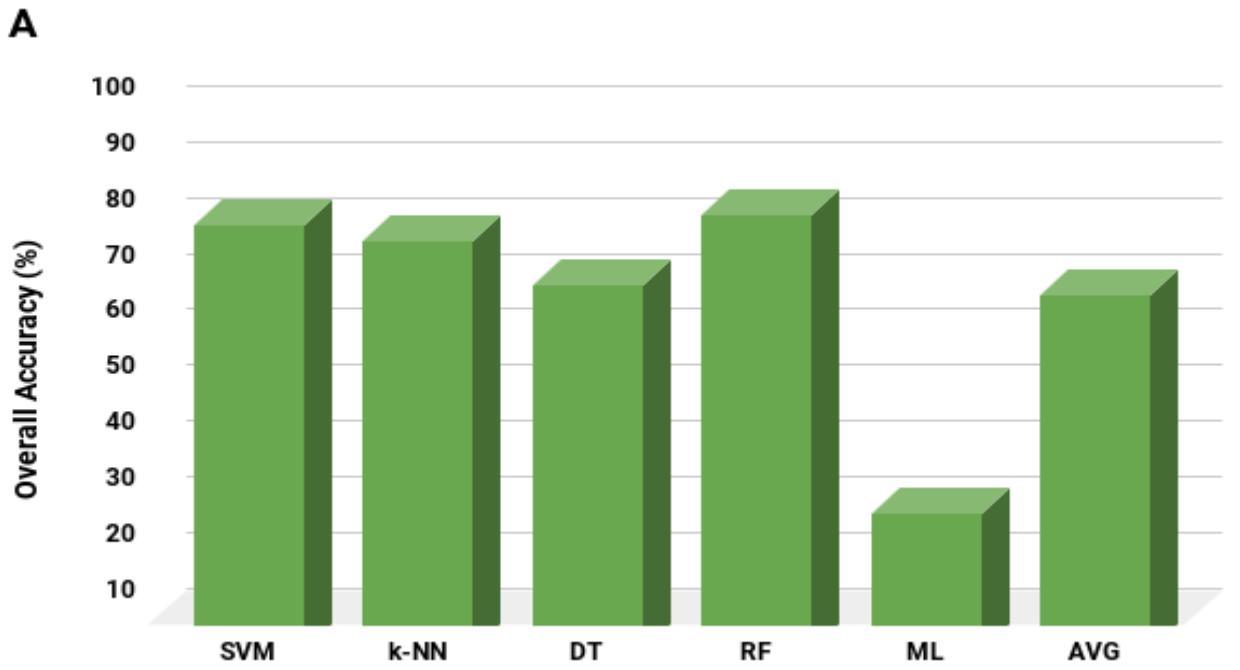

Figure A-5 Multi-temporal hand-selected image set Overall accuracies (OAs) and mean OAs (AVG) for all classifiers in Site A.

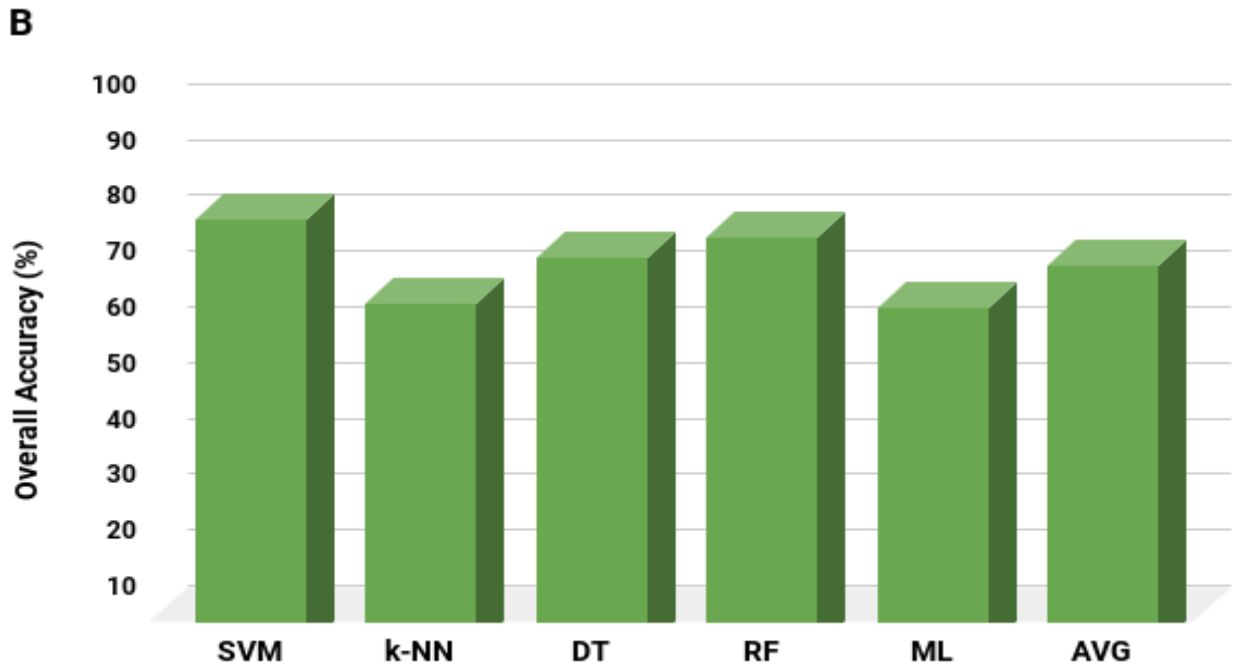

Figure A-6 Multi-temporal hand-selected image set Overall accuracies (OAs) and mean OAs (AVG) for all classifiers in Site B.

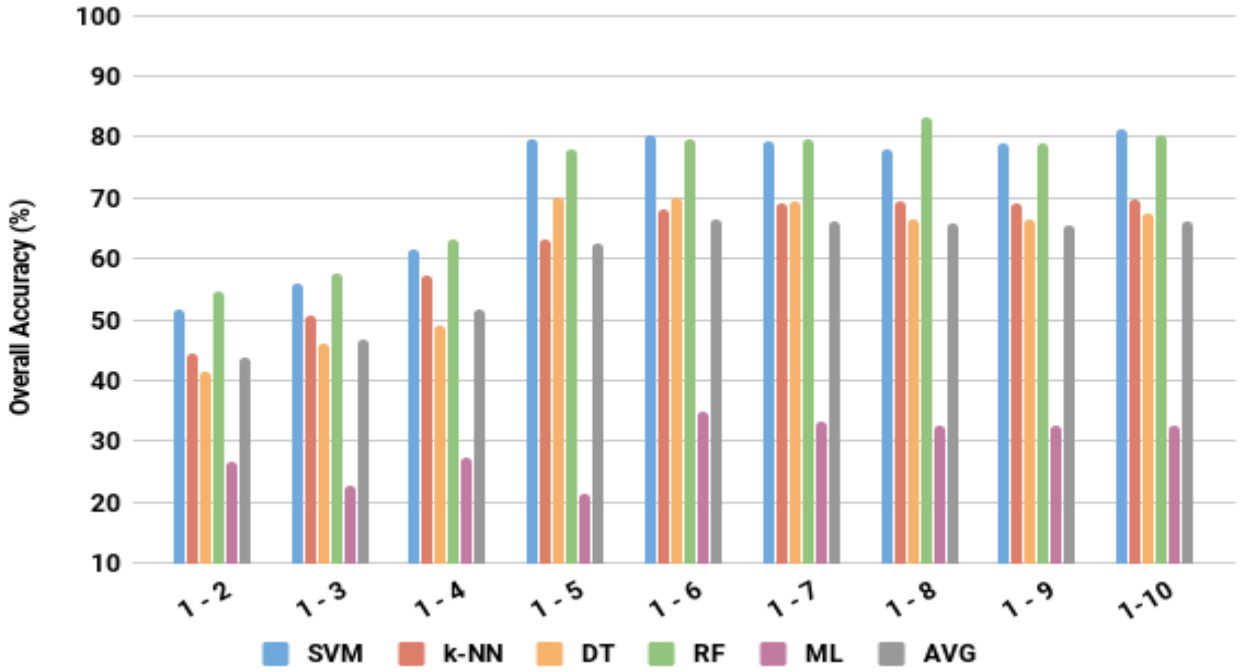

Figure A-7 Chronologic image addition Overall accuracies (OAs) and mean OAs (AVG) for all classifiers in Site A.

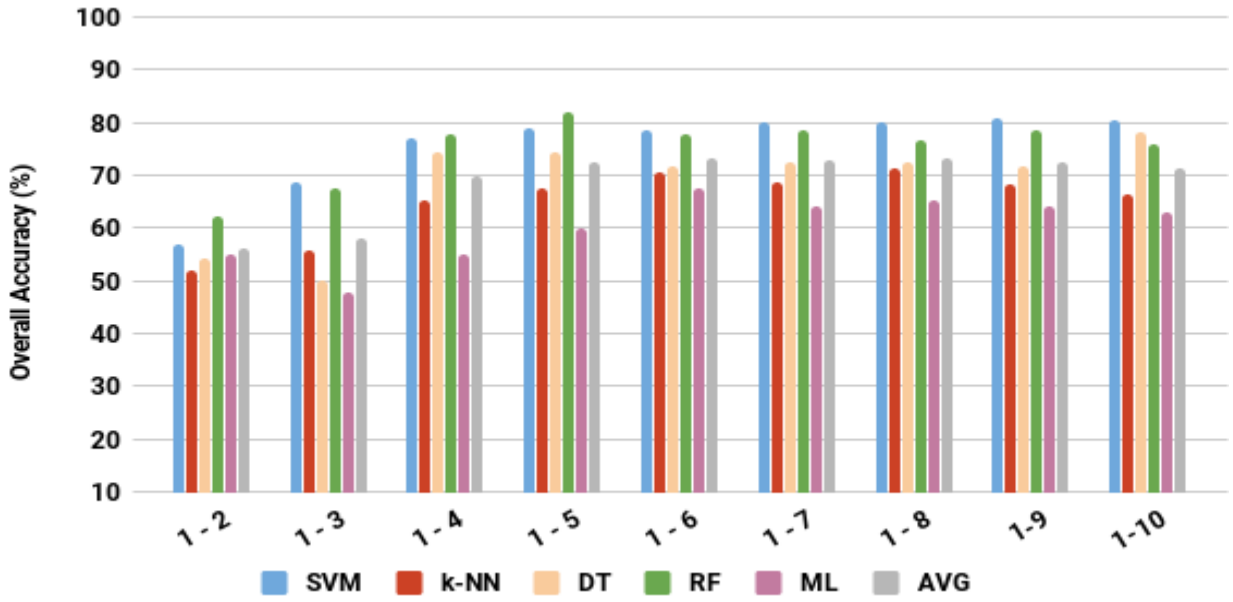

Figure A-8 Chronologic image addition Overall accuracies (OAs) and mean OAs (AVG) for all classifiers in Site B.

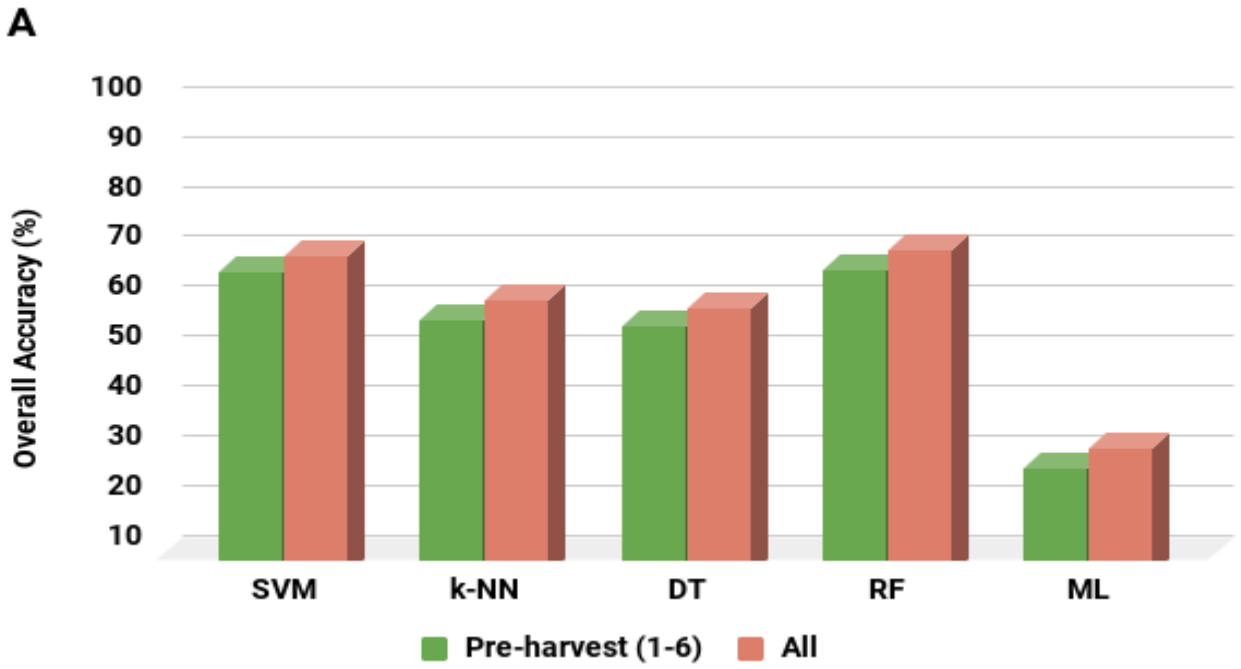

Figure A-9 Classifier performance comparison between pre-harvest and the entire time-series in Site A.

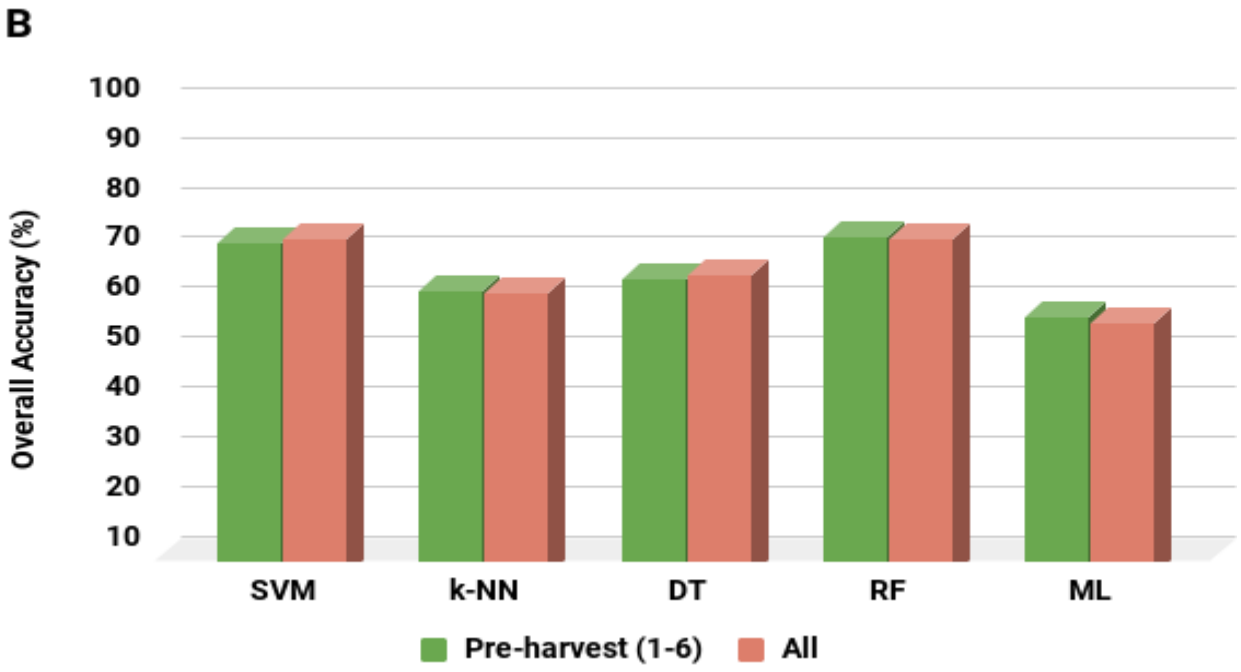

Figure A-10 Classifier performance comparison between pre-harvest and the entire time-series in Site A.

Table A-2 Confusion matrix for the best-performing classification results for Experiment 1 in Site A (4 August)

SVM

Class	**Canola**	**Fallow**	**Lucerne medics**	**Planted pastures**	**Wheat**	**TOTALS**	**PA%**	**EO%**
Canola	27	0	3	0	1	31	87.0968	12.9032
Fallow	0	39	0	1	1	41	95.122	4.87805
Lucerne medics	0	0	58	7	3	68	85.2941	14.7059
Planted pastures	1	3	9	17	4	34	50	50
Wheat	1	0	15	3	62	81	76.5432	23.4568
TOTALS	29	42	85	28	71	255		
CA%	93.1034	92.8571	68.2353	60.7143	87.3239			
EC%	6.89655	7.14286	31.7647	39.2857	12.6761			
Overall Accuracy:	79.6078							
Overall Kappa:	0.73438							

K-NN

Class	Canola	Fallow	Lucerne medics	Planted pastures	Wheat	TOTALS	PA%	EO%
Canola	27	0	3	0	1	31	87.0968	12.9032
Fallow	0	39	0	1	1	41	95.122	4.87805
Lucerne medics	1	0	45	11	11	68	66.1765	33.8235
Planted pastures	1	1	14	13	5	34	38.2353	61.7647
Wheat	1	0	17	8	55	81	67.9012	32.0988
TOTALS	30	40	79	33	73	255		
CA%	90	97.5	56.962	39.3939	75.3425			
EC%	10	2.5	43.038	60.6061	24.6575			
Overall Accuracy:	70.1961							
Overall Kappa:	0.612772							

DT

Class	Canola	Fallow	Lucerne medics	Planted pastures	Wheat	TOTALS	PA%	EO%
Canola	24	0	3	0	4	31	77.4194	22.5806
Fallow	0	37	1	2	1	41	90.2439	9.7561

Lucerne medics	1	3	41	12	11	68	60.2941	39.7059
Planted pastures	1	4	8	14	7	34	41.1765	58.8235
Wheat	3	0	16	8	54	81	66.6667	33.3333
TOTALS	29	44	69	36	77	255		
CA%	82.7586	84.0909	59.4203	38.8889	70.1299			
EC%	17.2414	15.9091	40.5797	61.1111	29.8701			
Overall Accuracy:	66.6667							
Overall Kappa:	0.56796							

RF ERROR MATRIX

Class	Canola	Fallow	Lucerne medics	Planted pastures	Wheat	TOTALS	PA%	EO%
Canola	29	0	1	0	1	31	93.5484	6.45161
Fallow	0	38	0	2	1	41	92.6829	7.31707
Lucerne medics	0	0	55	8	5	68	80.8824	19.1176
Planted pastures	1	4	8	15	6	34	44.1176	55.8824
Wheat	1	0	15	5	60	81	74.0741	25.9259
TOTALS	31	42	79	30	73	255		
CA%	93.5484	90.4762	69.6203	50	82.1918			
EC%	6.45161	9.52381	30.3797	50	17.8082			
Overall Accuracy:	77.2549							
Overall Kappa:	0.704419							

ML

Class	Canola	Fallow	Lucerne medics	Planted pastures	Wheat	TOTALS	PA%	EO%
Canola	26	0	5	0	0	31	83.871	16.129
Fallow	0	38	1	2	0	41	92.6829	7.31707
Lucerne medics	0	1	53	6	8	68	77.9412	22.0588
Planted pastures	0	2	10	16	6	34	47.0588	52.9412
Wheat	1	0	15	3	62	81	76.5432	23.4568
TOTALS	27	41	84	27	76	255		
CA%	96.2963	92.6829	63.0952	59.2593	81.5789			
EC%	3.7037	7.31707	36.9048	40.7407	18.4211			

Overall Accuracy:	76.4706
Overall Kappa:	0.692283

Table A-3 Confusion matrix for the best-performing classification results for Experiment 2 in Site A (4 August – single best)

SVM

Class	Canola	Fallow	Lucerne medics	Planted pastures	Wheat	TOTALS	PA%	EO%
Canola	27	0	3	0	1	31	87.0968	12.9032
Fallow	0	39	0	1	1	41	95.122	4.87805
Lucerne medics	0	0	58	7	3	68	85.2941	14.7059
Planted pastures	1	3	9	17	4	34	50	50
Wheat	1	0	15	3	62	81	76.5432	23.4568
TOTALS	29	42	85	28	71	255		
CA%	93.1034	92.8571	68.2353	60.7143	87.3239			
EC%	6.89655	7.14286	31.7647	39.2857	12.6761			

Overall Accuracy:	79.6078
Overall Kappa:	0.73438

K-NN

Class	Canola	Fallow	Lucerne medics	Planted pastures	Wheat	TOTALS	PA%	EO%
Canola	27	0	3	0	1	31	87.0968	12.9032
Fallow	0	39	0	1	1	41	95.122	4.87805
Lucerne medics	1	0	45	11	11	68	66.1765	33.8235
Planted pastures	1	1	14	13	5	34	38.2353	61.7647
Wheat	1	0	17	8	55	81	67.9012	32.0988
TOTALS	30	40	79	33	73	255		
CA%	90	97.5	56.962	39.3939	75.3425			
EC%	10	2.5	43.038	60.6061	24.6575			

Overall Accuracy:	70.1961
Overall Kappa:	0.612772

DT

Class	Canola	Fallow	Lucerne medics	Planted pastures	Wheat	TOTALS	PA%	EO%
Canola	24	0	3	0	4	31	77.4194	22.5806
Fallow	0	37	1	2	1	41	90.2439	9.7561
Lucerne medics	1	3	41	12	11	68	60.2941	39.7059
Planted pastures	1	4	8	14	7	34	41.1765	58.8235
Wheat	3	0	16	8	54	81	66.6667	33.3333
TOTALS	29	44	69	36	77	255		
CA%	82.7586	84.0909	59.4203	38.8889	70.1299			
EC%	17.2414	15.9091	40.5797	61.1111	29.8701			
Overall Accuracy:	66.6667							
Overall Kappa:	0.56796							

RF

Class	Canola	Fallow	Lucerne medics	Planted pastures	Wheat	TOTALS	PA%	EO%
Canola	29	0	1	0	1	31	93.5484	6.45161
Fallow	0	38	0	2	1	41	92.6829	7.31707
Lucerne medics	0	0	55	8	5	68	80.8824	19.1176
Planted pastures	1	4	8	15	6	34	44.1176	55.8824
Wheat	1	0	15	5	60	81	74.0741	25.9259
TOTALS	31	42	79	30	73	255		
CA%	93.5484	90.4762	69.6203	50	82.1918			
EC%	6.45161	9.52381	30.3797	50	17.8082			
Overall Accuracy:	77.2549							
Overall Kappa:	0.704419							

ML

Class	Canola	Fallow	Lucerne medics	Planted pastures	Wheat	TOTALS	PA%	EO%
Canola	26	0	5	0	0	31	83.871	16.129
Fallow	0	38	1	2	0	41	92.6829	7.31707
Lucerne medics	0	1	53	6	8	68	77.9412	22.0588
Planted pastures	0	2	10	16	6	34	47.0588	52.9412
Wheat	1	0	15	3	62	81	76.5432	23.4568

TOTALS	27	41	84	27	76	255
CA%	96.2963	92.6829	63.0952	59.2593	81.5789	
EC%	3.7037	7.31707	36.9048	40.7407	18.4211	
Overall Accuracy:	76.4706					
Overall Kappa:	0.692283					

Table A-4 Confusion matrix for the best-performing classification results for Experiment 3 in Site A (hand-selected five)

SVM

Class	Canola	Fallow	Lucerne medics	Planted pastures	Wheat	TOTALS	PA%	EO%
Canola	29	0	1	0	1	31	93.5484	6.45161
Fallow	0	39	0	1	1	41	95.122	4.87805
Lucerne medics	0	2	54	4	8	68	79.4118	20.5882
Planted pastures	0	1	10	16	7	34	47.0588	52.9412
Wheat	1	0	12	3	65	81	80.2469	19.7531
TOTALS	30	42	77	24	82	255		
CA%	96.6667	92.8571	70.1299	66.6667	79.2683			
EC%	3.33333	7.14286	29.8701	33.3333	20.7317			
Overall Accuracy:	79.6078							
Overall Kappa:	0.733086							

K-NN

Class	Canola	Fallow	Lucerne medics	Planted pastures	Wheat	TOTALS	PA%	EO%
Canola	28	0	2	0	1	31	90.3226	9.67742
Fallow	0	33	2	1	5	41	80.4878	19.5122
Lucerne medics	0	1	58	4	5	68	85.2941	14.7059
Planted pastures	1	4	10	15	4	34	44.1176	55.8824
Wheat	1	0	10	8	62	81	76.5432	23.4568
TOTALS	30	38	82	28	77	255		
CA%	93.3333	86.8421	70.7317	53.5714	80.5195			
EC%	6.66667	13.1579	29.2683	46.4286	19.4805			
Overall Accuracy:	76.8627							
Overall Kappa:	0.697722							

DT

Class	Canola	Fallow	Lucerne medics	Planted pastures	Wheat	TOTALS	PA% EO%	
Canola	29	0	2	0	0	31	93.5484	6.45161
Fallow	0	35	1	1	4	41	85.3659	14.6341
Lucerne medics	1	2	48	8	9	68	70.5882	29.4118
Planted pastures	0	3	8	11	12	34	32.3529	67.6471
Wheat	4	1	15	8	53	81	65.4321	34.5679
TOTALS	34	41	74	28	78	255		
CA%	85.2941	85.3659	64.8649	39.2857	67.9487			
EC%	14.7059	14.6341	35.1351	60.7143	32.0513			
Overall Accuracy:	69.0196							
Overall Kappa:	0.597003							

RF

Class	Canola	Fallow	Lucerne medics	Planted pastures	Wheat	TOTALS	PA%	EO%
Canola	30	0	1	0	0	31	96.7742	3.22581
Fallow	0	38	1	1	1	41	92.6829	7.31707
Lucerne medics	0	2	56	4	6	68	82.3529	17.6471
Planted pastures	0	3	8	18	5	34	52.9412	47.0588
Wheat	1	0	11	3	66	81	81.4815	18.5185
TOTALS	31	43	77	26	78	255		
CA%	96.7742	88.3721	72.7273	69.2308	84.6154			
EC%	3.22581	11.6279	27.2727	30.7692	15.3846			
Overall Accuracy:	81.5686							
Overall Kappa:	0.759641							

ML

Class	Canola	Fallow	Lucerne medics	Planted pastures	Wheat	TOTALS	PA%	EO%
Canola	20	5	5	0	1	31	64.5161	35.4839
Fallow	0	36	0	0	5	41	87.8049	12.1951
Lucerne medics	0	58	6	1	3	68	8.82353	91.1765

Planted pastures	0	31	1	1	1	34	2.94118	97.0588
Wheat	0	68	1	3	9	81	11.1111	88.8889
TOTALS	20	198	13	5	19	255		
CA%	100	18.1818	46.1538	20	47.3684			
EC%	0	81.8182	53.8462	80	52.6316			
Overall Accuracy:	28.2353							
Overall Kappa:	0.130908							

Table A-5 Confusion matrix for the best-performing classification results for Experiment 3 in Site A (6 April –3 Sept)

SVM								
Class	Canola	Fallow	Lucern medics	Planted pastures	Wheat	TOTALS	PA%	EO%
Canola	28	0	1	0	2	31	90.3226	9.67742
Fallow	0	39	0	1	1	41	95.122	4.87805
Lucern medics	0	2	53	6	7	68	77.9412	22.0588
Planted pastures	0	3	5	20	6	34	58.8235	41.1765
Wheat	1	0	9	6	65	81	80.2469	19.7531
TOTALS	29	44	68	33	81	255		
CA%	96.5517	88.6364	77.9412	60.6061	80.2469			
EC%	3.44828	11.3636	22.0588	39.3939	19.7531			
Overall Accuracy:	80.3922							
Overall Kappa:	0.745076							
K-NN								
Class	Canola	Fallow	Lucern medics	Planted pastures	Wheat	TOTALS	PA%	EO%
Canola	26	0	4	0	1	31	83.871	16.129
Fallow	0	29	2	5	5	41	70.7317	29.2683
Lucern medics	0	4	48	9	7	68	70.5882	29.4118
Planted pastures	1	3	11	14	5	34	41.1765	58.8235
Wheat	3	0	12	9	57	81	70.3704	29.6296
TOTALS	30	36	77	37	75	255		
CA%	86.6667	80.5556	62.3377	37.8378	76			
EC%	13.3333	19.4444	37.6623	62.1622	24			

Overall Accuracy:	68.2353							
Overall Kappa:	0.587313							
DT								
Class	Canola	Fallow	Lucern medics	Planted pastures	Wheat	TOTALS	PA%	EO%
Canola	29	0	1	0	1	31	93.5484	6.45161
Fallow	1	39	1	0	0	41	95.122	4.87805
Lucern medics	2	1	45	9	11	68	66.1765	33.8235
Planted pastures	1	2	6	17	8	34	50	50
Wheat	3	1	17	11	49	81	60.4938	39.5062
TOTALS	36	43	70	37	69	255		
CA%	80.5556	90.6977	64.2857	45.9459	71.0145			
EC%	19.4444	9.30233	35.7143	54.0541	28.9855			
Overall Accuracy:	70.1961							
Overall Kappa:	0.616534							
RF								
Class	Canola	Fallow	Lucern medics	Planted pastures	Wheat	TOTALS	PA%	EO%
Canola	30	0	1	0	0	31	96.7742	3.22581
Fallow	0	38	1	1	1	41	92.6829	7.31707
Lucern medics	0	2	52	8	6	68	76.4706	23.5294
Planted pastures	1	3	6	18	6	34	52.9412	47.0588
Wheat	1	0	12	3	65	81	80.2469	19.7531
TOTALS	32	43	72	30	78	255		
CA%	93.75	88.3721	72.2222	60	83.3333			
EC%	6.25	11.6279	27.7778	40	16.6667			
Overall Accuracy:	79.6078							
Overall Kappa:	0.734991							
ML								
Class	Canola	Fallow	Lucern medics	Planted pastures	Wheat	TOTALS	PA%	EO%
Canola	2	0	0	0	29	31	6.45161	93.5484
Fallow	0	0	22	0	19	41	0	100

Lucern medics	0	0	6	0	62	68	8.82353	91.1765
Planted pastures	0	0	4	0	30	34	0	100
Wheat	0	0	0	0	81	81	100	0
TOTALS	2	0	32	0	221	255		
CA%	100	-1.#IND	18.75	-1.#IND	36.6516			
EC%	0	-1.#IND	81.25	-1.#IND	63.3484			
Overall Accuracy:	34.902							
Overall Kappa:	0.056944							

Table A-6 Confusion matrix for the best-performing classification results for Experiment 1 in Site B (1 August)

SVM

Class	Canola	Fallow	Lucerne medics	Planted pastures	Wheat	TOTALS	PA%	EO%
Canola	34	0	1	0	0	35	97.1429	2.85714
Fallow	0	43	0	0	0	43	100	0
Lucerne medics	0	3	19	12	0	34	55.8824	44.1176
Planted pastures	0	1	11	24	2	38	63.1579	36.8421
Wheat	0	0	1	3	13	17	76.4706	23.5294
TOTALS	34	47	32	39	15	167		
CA%	100	91.4894	59.375	61.5385	86.6667			
EC%	0	8.51064	40.625	38.4615	13.3333			
Overall Accuracy:	79.6407							
Overall Kappa:	0.740173							

K-NN

Class	Canola	Fallow	Lucerne medics	Planted pastures	Wheat	TOTALS	PA%	EO%
Canola	33	0	2	0	0	35	94.2857	5.71429
Fallow	0	32	2	6	3	43	74.4186	25.5814
Lucerne medics	1	1	18	11	3	34	52.9412	47.0588
Planted pastures	0	4	12	16	6	38	42.1053	57.8947
Wheat	0	1	3	3	10	17	58.8235	41.1765
TOTALS	34	38	37	36	22	167		

CA%	97.0588	84.2105	48.6486	44.4444	45.4545			
EC%	2.94118	15.7895	51.3514	55.5556	54.5455			
Overall Accuracy:	65.2695							
Overall Kappa:	0.561024							

DT

Class	Canola	Fallow	Lucerne medics	Planted pastures	Wheat	TOTALS	PA%	EO%
Canola	31	0	2	2	0	35	88.5714	11.4286
Fallow	0	34	5	1	3	43	79.0698	20.9302
Lucerne medics	0	2	17	14	1	34	50	50
Planted pastures	1	2	14	19	2	38	50	50
Wheat	2	1	1	3	10	17	58.8235	41.1765
TOTALS	34	39	39	39	16	167		
CA%	91.1765	87.1795	43.5897	48.7179	62.5			
EC%	8.82353	12.8205	56.4103	51.2821	37.5			
Overall Accuracy:	66.4671							
Overall Kappa:	0.573785							

RF

Class	Canola	Fallow	Lucerne medics	Planted pastures	Wheat	TOTALS	PA%	EO%
Canola	32	0	3	0	0	35	91.4286	8.57143
Fallow	0	43	0	0	0	43	100	0
Lucerne medics	1	2	17	14	0	34	50	50
Planted pastures	1	1	12	22	2	38	57.8947	42.1053
Wheat	0	0	3	2	12	17	70.5882	29.4118
TOTALS	34	46	35	38	14	167		
CA%	94.1176	93.4783	48.5714	57.8947	85.7143			
EC%	5.88235	6.52174	51.4286	42.1053	14.2857			
Overall Accuracy:	75.4491							
Overall Kappa:	0.686622							

ML

Class	Canola	Fallow	Lucerne medics	Planted pastures	Wheat	TOTALS	PA%	EO%
Canola	28	1	0	0	6	35	80	20
Fallow	0	29	2	12	0	43	67.4419	32.5581
Lucerne medics	1	16	8	8	1	34	23.5294	76.4706
Planted pastures	1	15	16	2	4	38	5.26316	94.7368
Wheat	3	9	0	4	1	17	5.88235	94.1176
TOTALS	33	70	26	26	12	167		
CA%	84.8485	41.4286	30.7692	7.69231	8.33333			
EC%	15.1515	58.5714	69.2308	92.3077	91.6667			
Overall Accuracy:	40.7186							
Overall Kappa:	0.23628							

Table A-7 Confusion matrix for the best-performing classification results for Experiment 2 in Site B (2 best – 1 & 11 August)

SVM								
Class	Canola	Fallow	Lucerne medics	Planted pastures	Wheat	TOTALS	PA%	EO%
Canola	35	0	0	0	0	35	100	0
Fallow	0	41	0	0	2	43	95.3488	4.65116
Lucerne medics	2	3	21	7	1	34	61.7647	38.2353
Planted pastures	0	1	12	22	3	38	57.8947	42.1053
Wheat	1	0	2	2	12	17	70.5882	29.4118
TOTALS	38	45	35	31	18	167		
CA%	92.1053	91.1111	60	70.9677	66.6667			
EC%	7.89474	8.88889	40	29.0323	33.3333			
Overall Accuracy:	78.4431							
Overall Kappa:	0.726105							
K-NN								
Class	Canola	Fallow	Lucerne medics	Planted pastures	Wheat	TOTALS	PA%	EO%
Canola	33	1	1	0	0	35	94.2857	5.71429
Fallow	0	32	1	7	3	43	74.4186	25.5814
Lucerne medics	0	1	20	13	0	34	58.8235	41.1765

Planted pastures	1	3	14	17	3	38	44.7368	55.2632
Wheat	0	0	2	3	12	17	70.5882	29.4118
TOTALS	34	37	38	40	18	167		
CA%	97.0588	86.4865	52.6316	42.5	66.6667			
EC%	2.94118	13.5135	47.3684	57.5	33.3333			
Overall Accuracy:	68.2635							
Overall Kappa:	0.597499							

DT

Class	Canola	Fallow	Lucerne medics	Planted pastures	Wheat	TOTALS	PA%	EO%
Canola	33	0	0	2	0	35	94.2857	5.71429
Fallow	0	39	1	2	1	43	90.6977	9.30233
Lucerne medics	1	3	17	12	1	34	50	50
Planted pastures	1	1	14	18	4	38	47.3684	52.6316
Wheat	0	2	2	1	12	17	70.5882	29.4118
TOTALS	35	45	34	35	18	167		
CA%	94.2857	86.6667	50	51.4286	66.6667			
EC%	5.71429	13.3333	50	48.5714	33.3333			
Overall Accuracy:	71.2575							
Overall Kappa:	0.63459							

RF

Class	Canola	Fallow	Lucerne medics	Planted pastures	Wheat	TOTALS	PA%	EO%
Canola	33	0	2	0	0	35	94.2857	5.71429
Fallow	0	43	0	0	0	43	100	0
Lucerne medics	1	2	18	13	0	34	52.9412	47.0588
Planted pastures	1	0	11	24	2	38	63.1579	36.8421
Wheat	1	0	3	2	11	17	64.7059	35.2941
TOTALS	36	45	34	39	13	167		
CA%	91.6667	95.5556	52.9412	61.5385	84.6154			
EC%	8.33333	4.44444	47.0588	38.4615	15.3846			
Overall Accuracy:	77.2455							

Overall Kappa:	0.709366							
ML								
Class	Canola	Fallow	Lucerne medics	Planted pastures	Wheat	TOTALS	PA%	EO%
Canola	31	0	3	1	0	35	88.5714	11.4286
Fallow	0	36	0	7	0	43	83.7209	16.2791
Lucerne medics	0	0	11	23	0	34	32.3529	67.6471
Planted pastures	0	0	6	32	0	38	84.2105	15.7895
Wheat	3	0	2	12	0	17	0	100
TOTALS	34	36	22	75	0	167		
CA%	91.1765	100	50	42.6667	-1.#IND			
EC%	8.82353	0	50	57.3333	-1.#IND			
Overall Accuracy:	65.8683							
Overall Kappa:	0.558345							

Table A-8 Confusion matrix for the best-performing classification results for Experiment 3 in Site B (hand-selected five)

SVM								
Class	Canola	Fallow	Lucerne medics	Planted pastures	Wheat	TOTALS	PA%	EO%
Canola	35	0	0	0	0	35	100	0
Fallow	0	40	0	3	0	43	93.0233	6.97674
Lucerne medics	0	2	17	13	2	34	50	50
Planted pastures	1	1	6	28	2	38	73.6842	26.3158
Wheat	0	0	1	2	14	17	82.3529	17.6471
TOTALS	36	43	24	46	18	167		
CA%	97.2222	93.0233	70.8333	60.8696	77.7778			
EC%	2.77778	6.97674	29.1667	39.1304	22.2222			
Overall Accuracy:	80.2395							
Overall Kappa:	0.748471							
K-NN								
Class	Canola	Fallow	Lucerne medics	Planted pastures	Wheat	TOTALS	PA%	EO%
Canola	31	0	2	0	2	35	88.5714	11.4286

Fallow	0	33	3	6	1	43	76.7442	23.2558
Lucerne medics	1	2	15	14	2	34	44.1176	55.8824
Planted pastures	0	6	9	18	5	38	47.3684	52.6316
Wheat	1	2	0	2	12	17	70.5882	29.4118
TOTALS	33	43	29	40	22	167		
CA%	93.9394	76.7442	51.7241	45	54.5455			
EC%	6.06061	23.2558	48.2759	55	45.4545			
Overall Accuracy:	65.2695							
Overall Kappa:	0.559827							

DT

Class	Canola	Fallow	Lucerne medics	Planted pastures	Wheat	TOTALS	PA%	EO%
Canola	33	0	1	0	1	35	94.2857	5.71429
Fallow	0	40	1	1	1	43	93.0233	6.97674
Lucerne medics	0	0	19	12	3	34	55.8824	44.1176
Planted pastures	0	2	13	21	2	38	55.2632	44.7368
Wheat	0	1	2	4	10	17	58.8235	41.1765
TOTALS	33	43	36	38	17	167		
CA%	100	93.0233	52.7778	55.2632	58.8235			
EC%	0	6.97674	47.2222	44.7368	41.1765			
Overall Accuracy:	73.6527							
Overall Kappa:	0.664903							

RF

Class	Canola	Fallow	Lucerne medics	Planted pastures	Wheat	TOTALS	PA%	EO%
Canola	33	0	1	0	1	35	94.2857	5.71429
Fallow	0	41	0	2	0	43	95.3488	4.65116
Lucerne medics	1	3	18	12	0	34	52.9412	47.0588
Planted pastures	1	1	10	24	2	38	63.1579	36.8421
Wheat	0	0	1	3	13	17	76.4706	23.5294
TOTALS	35	45	30	41	16	167		
CA%	94.2857	91.1111	60	58.5366	81.25			

EC%	5.71429	8.88889	40	41.4634	18.75			
Overall Accuracy:	77.2455							
Overall Kappa:	0.70995							
ML								
Class	Canola	Fallow	Lucerne medics	Planted pastures	Wheat	TOTALS	PA%	EO%
Canola	35	0	0	0	0	35	100	0
Fallow	0	38	0	5	0	43	88.3721	11.6279
Lucerne medics	7	2	10	15	0	34	29.4118	70.5882
Planted pastures	7	2	4	25	0	38	65.7895	34.2105
Wheat	11	1	0	5	0	17	0	100
TOTALS	60	43	14	50	0	167		
CA%	58.3333	88.3721	71.4286	50	-1.#IND			
EC%	41.6667	11.6279	28.5714	50	-1.#IND			
Overall Accuracy:	64.6707							
Overall Kappa:	0.543081							

Table A-9 Confusion matrix for the best-performing classification results for Experiment 4 in Site B (3 April – 21 August)

SVM								
Class	Canola	Fallow	Lucerne medics	Planted pastures	Wheat	TOTALS	PA%	EO%
Canola	35	0	0	0	0	35	100	0
Fallow	0	41	1	0	1	43	95.3488	4.65116
Lucerne medics	1	1	17	14	1	34	50	50
Planted pastures	0	1	11	24	2	38	63.1579	36.8421
Wheat	0	0	0	3	14	17	82.3529	17.6471
TOTALS	36	43	29	41	18	167		
CA%	97.2222	95.3488	58.6207	58.5366	77.7778			
EC%	2.77778	4.65116	41.3793	41.4634	22.2222			
Overall Accuracy:	78.4431							
Overall Kappa:	0.725855							
K-NN								

Class	Canola	Fallow	Lucerne medics	Planted pastures	Wheat	TOTALS	PA%	EO%
Canola	33	0	0	0	2	35	94.2857	5.71429
Fallow	0	36	3	3	1	43	83.7209	16.2791
Lucerne medics	1	0	17	14	2	34	50	50
Planted pastures	1	5	8	20	4	38	52.6316	47.3684
Wheat	1	1	2	1	12	17	70.5882	29.4118
TOTALS	36	42	30	38	21	167		
CA%	91.6667	85.7143	56.6667	52.6316	57.1429			
EC%	8.33333	14.2857	43.3333	47.3684	42.8571			
Overall Accuracy:	70.6587							
Overall Kappa:	0.628079							

DT

Class	Canola	Fallow	Lucerne medics	Planted pastures	Wheat	TOTALS	PA%	EO%
Canola	34	0	1	0	0	35	97.1429	2.85714
Fallow	0	39	1	2	1	43	90.6977	9.30233
Lucerne medics	0	1	14	16	3	34	41.1765	58.8235
Planted pastures	1	0	12	23	2	38	60.5263	39.4737
Wheat	0	1	3	3	10	17	58.8235	41.1765
TOTALS	35	41	31	44	16	167		
CA%	97.1429	95.122	45.1613	52.2727	62.5			
EC%	2.85714	4.87805	54.8387	47.7273	37.5			
Overall Accuracy:	71.8563							
Overall Kappa:	0.641647							

RF

Class	Canola	Fallow	Lucerne medics	Planted pastures	Wheat	TOTALS	PA%	EO%
Canola	34	0	1	0	0	35	97.1429	2.85714
Fallow	0	40	0	3	0	43	93.0233	6.97674
Lucerne medics	0	3	19	12	0	34	55.8824	44.1176
Planted pastures	1	0	9	26	2	38	68.4211	31.5789
Wheat	1	0	2	3	11	17	64.7059	35.2941

TOTALS	36	43	31	44	13	167
CA%	94.4444	93.0233	61.2903	59.0909	84.6154	
EC%	5.55556	6.97674	38.7097	40.9091	15.3846	
Overall Accuracy:	77.8443					
Overall Kappa:	0.716988					

ML

Class	Canola	Fallow	Lucerne medics	Planted pastures	Wheat	TOTALS	PA%	EO%
Canola	34	0	0	1	0	35	97.1429	2.85714
Fallow	0	40	0	3	0	43	93.0233	6.97674
Lucerne medics	2	5	13	14	0	34	38.2353	61.7647
Planted pastures	4	3	5	26	0	38	68.4211	31.5789
Wheat	8	1	0	8	0	17	0	100
TOTALS	48	49	18	52	0	167		
CA%	70.8333	81.6327	72.2222	50	-1.#IND			
EC%	29.1667	18.3673	27.7778	50	-1.#IND			
Overall Accuracy:	67.6647							
Overall Kappa:	0.580831							

APPENDIX B

Supplementary material for Chapter 4 (Classifications confusion matrices)

Table B-1 Confusion matrix for classification results obtained with cloud-free images only (experiment 1).

SVM									
Class	Citrus fruit	Grapes	Planted pastures	Pome fruit	Stone fruit	Exotic fruit	TOTALS	PA%	EO%
Citrus fruit	39	1	4	1	1	0	46	84.7826	15.2174
Grapes	2	66	26	0	3	3	100	66	34
Planted pastures	1	7	114	0	2	0	124	91.9355	8.06452
Pome fruit	2	1	0	34	1	0	38	89.4737	10.5263
Stone fruit	1	3	5	12	24	2	47	51.0638	48.9362
Exotic fruit	0	1	0	1	4	13	19	68.4211	31.5789
TOTALS	45	79	149	48	35	18	374		
CA%	86.6667	83.5443	76.5101	70.8333	68.5714	72.2222			
EC%	13.3333	16.4557	23.4899	29.1667	31.4286	27.7778			
Overall Accuracy:	77.5401								
Overall Kappa:	0.708081								

K-NN									
Class	Citrus fruit	Grapes	Planted pastures	Pome fruit	Stone fruit	Exotic fruit	TOTALS	PA%	EO%
Citrus fruit	37	0	5	0	4	0	46	80.4348	19.5652
Grapes	4	64	26	1	4	1	100	64	36
Planted pastures	0	15	106	1	1	1	124	85.4839	14.5161
Pome fruit	2	0	0	26	5	5	38	68.4211	31.5789
Stone fruit	1	3	6	8	29	0	47	61.7021	38.2979
Exotic fruit	1	2	1	1	0	14	19	73.6842	26.3158
TOTALS	45	84	144	37	43	21	374		
CA%	82.2222	76.1905	73.6111	70.2703	67.4419	66.6667			
EC%	17.7778	23.8095	26.3889	29.7297	32.5581	33.3333			
Overall Accuracy:	73.7968								
Overall Kappa:	0.65976								

DT

Class	Citrus fruit	Grapes	Planted pastures	Pome fruit	Stone fruit	Exotic fruit	TOTALS	PA%	EO%
Citrus fruit	30	1	3	3	5	4	46	65.2174	34.7826
Grapes	2	56	26	3	12	1	100	56	44
Planted pastures	1	15	101	3	2	2	124	81.4516	18.5484
Pome fruit	5	3	2	18	7	3	38	47.3684	52.6316
Stone fruit	3	9	2	14	16	3	47	34.0426	65.9574
Exotic fruit	2	3	0	2	4	8	19	42.1053	57.8947
TOTALS	43	87	134	43	46	21	374		
CA%	69.7674	64.3678	75.3731	41.8605	34.7826	38.0952			
EC%	30.2326	35.6322	24.6269	58.1395	65.2174	61.9048			
Overall Accuracy:	61.2299								
Overall Kappa:	0.499663								

RF

Class	Citrus fruit	Grapes	Planted pastures	Pome fruit	Stone fruit	Exotic fruit	TOTALS	PA%	EO%
Citrus fruit	36	2	4	3	1	0	46	78.2609	21.7391
Grapes	2	69	25	0	1	3	100	69	31
Planted pastures	0	7	117	0	0	0	124	94.3548	5.64516
Pome fruit	2	0	0	34	2	0	38	89.4737	10.5263
Stone fruit	3	9	2	11	21	1	47	44.6809	55.3191
Exotic fruit	0	3	1	1	2	12	19	63.1579	36.8421
TOTALS	43	90	149	49	27	16	374		
CA%	83.7209	76.6667	78.5235	69.3878	77.7778	75			
EC%	16.2791	23.3333	21.4765	30.6122	22.2222	25			
Overall Accuracy:	77.2727								
Overall Kappa:	0.702861								

Table B-2 Confusion matrix for classification results obtained with all images including cloud-contaminated images (Experiment 2).

SVM

Class	Citrus fruit	Grapes	Planted pastures	Pome fruit	Stone fruit	Exotic fruit	TOTALS	PA%	EO%
Citrus fruit	38	3	3	0	2	0	46	82.6087	17.3913
Grapes	2	68	26	0	0	4	100	68	32
Planted pastures	0	0	123	0	1	0	124	99.1935	0.806452
Pome fruit	2	2	0	31	2	1	38	81.5789	18.4211
Stone fruit	0	4	4	11	28	0	47	59.5745	40.4255
Exotic fruit	0	2	0	1	1	15	19	78.9474	21.0526
TOTALS	42	79	156	43	34	20	374		
CA%	90.4762	86.0759	78.8462	72.093	82.3529	75			
EC%	9.52381	13.9241	21.1538	27.907	17.6471	25			
Overall Accuracy:	81.016								
Overall Kappa:	0.752036								

K-NN

Class	Citrus fruit	Grapes	Planted pastures	Pome fruit	Stone fruit	Exotic fruit	TOTALS	PA%	EO%
Citrus fruit	37	3	3	1	1	1	46	80.4348	19.5652
Grapes	5	56	27	4	2	6	100	56	44
Planted pastures	3	15	101	1	4	0	124	81.4516	18.5484
Pome fruit	0	1	3	25	9	0	38	65.7895	34.2105
Stone fruit	0	3	8	11	25	0	47	53.1915	46.8085
Exotic fruit	0	2	0	1	1	15	19	78.9474	21.0526
TOTALS	45	80	142	43	42	22	374		
CA%	82.2222	70	71.1268	58.1395	59.5238	68.1818			
EC%	17.7778	30	28.8732	41.8605	40.4762	31.8182			
Overall Accuracy:	69.2513								
Overall Kappa:	0.602392								

DT

Class	Citrus fruit	Grapes	Planted pastures	Pome fruit	Stone fruit	Exotic fruit	TOTALS	PA%	EO%

Citrus fruit	34	1	4	4	2	1	46	73.913	26.087
Grapes	1	61	23	3	6	6	100	61	39
Planted pastures	2	20	100	1	1	0	124	80.6452	19.3548
Pome fruit	6	4	1	16	9	2	38	42.1053	57.8947
Stone fruit	0	13	2	13	16	3	47	34.0426	65.9574
Exotic fruit	3	2	0	1	3	10	19	52.6316	47.3684
TOTALS	46	101	130	38	37	22	374		
CA%	73.913	60.396	76.9231	42.1053	43.2432	45.4545			
EC%	26.087	39.604	23.0769	57.8947	56.7568	54.5455			
Overall Accuracy:	63.369								
Overall Kappa:	0.525306								

RF

Class	Citrus fruit	Grapes	Planted pastures	Pome fruit	Stone fruit	Exotic fruit	TOTALS	PA%	EO%
Citrus fruit	35	3	4	2	2	0	46	76.087	23.913
Grapes	1	71	23	0	2	3	100	71	29
Planted pastures	0	7	117	0	0	0	124	94.3548	5.64516
Pome fruit	2	0	0	34	2	0	38	89.4737	10.5263
Stone fruit	1	11	2	15	18	0	47	38.2979	61.7021
Exotic fruit	0	2	1	2	0	14	19	73.6842	26.3158
TOTALS	39	94	147	53	24	17	374		
CA%	89.7436	75.5319	79.5918	64.1509	75	82.3529			
EC%	10.2564	24.4681	20.4082	35.8491	25	17.6471			
Overall Accuracy:	77.2727								
Overall Kappa:	0.702867								

Table B-3 Confusion matrix for classification results obtained with the MC image compositing approach (Experiment 3).

SVM

Class	Citrus fruit	Grapes	Planted pastures	Pome fruit	Stone fruit	Exotic fruit	TOTALS	PA%	EO%
Citrus fruit	38	1	4	1	2	0	46	82.6087	17.3913
Grapes	2	65	26	2	2	3	100	65	35
Planted fastures	1	3	118	1	0	1	124	95.1613	4.83871

Pome fruit	1	2	1	29	2	2	37	78.3784	21.6216
Stone fruit	1	3	5	9	28	1	47	59.5745	40.4255
Exotic fruit	0	2	0	1	1	15	19	78.9474	21.0526
TOTALS	43	76	154	43	35	22	373		
CA%	88.3721	85.5263	76.6234	67.4419	80	68.1818			
EC%	11.6279	14.4737	23.3766	32.5581	20	31.8182			
Overall Accuracy:	78.5523								
Overall Kappa:	0.720602								

K-NN

Class	Citrus fruit	Grapes	Planted pastures	Pome fruit	Stone fruit	Exotic fruit	TOTALS	PA%	EO%
Citrus fruit	35	1	3	3	2	2	46	76.087	23.913
Grapes	6	59	25	1	5	4	100	59	41
Planted pastures	2	13	108	0	0	1	124	87.0968	12.9032
Pome fruit	1	3	1	25	7	0	37	67.5676	32.4324
Stone fruit	0	6	5	7	27	2	47	57.4468	42.5532
Exotic fruit	0	2	1	0	1	15	19	78.9474	21.0526
TOTALS	44	84	143	36	42	24	373		
CA%	79.5455	70.2381	75.5245	69.4444	64.2857	62.5			
EC%	20.4545	29.7619	24.4755	30.5556	35.7143	37.5			
Overall Accuracy:	72.118								
Overall Kappa:	0.638171								

DT

Class	Citrus fruit	Grapes	Planted pastures	Pome fruit	Stone fruit	Exotic fruit	TOTALS	PA%	EO%
Citrus fruit	35	2	3	2	3	1	46	76.087	23.913
Grapes	7	55	21	8	9	0	100	55	45
Planted pastures	3	18	98	2	2	1	124	79.0323	20.9677
Pome fruit	6	2	0	22	5	2	37	59.4595	40.5405
Stone fruit	5	12	3	10	15	2	47	31.9149	68.0851
Exotic fruit	4	1	1	1	3	9	19	47.3684	52.6316
TOTALS	60	90	126	45	37	15	373		

CA%	58.3333	61.1111	77.7778	48.8889	40.5405	60
EC%	41.6667	38.8889	22.2222	51.1111	59.4595	40
Overall Accuracy:	62.7346					
Overall Kappa:	0.520184					

RF

Class	Citrus fruit	Grapes	Planted pastures	Pome fruit	Stone fruit	Exotic fruit	TOTALS	PA%	EO%
Citrus fruit	34	3	4	1	3	1	46	73.913	26.087
Grapes	1	71	24	0	2	2	100	71	29
Planted pastures	0	9	115	0	0	0	124	92.7419	7.25806
Pome fruit	2	1	0	30	2	2	37	81.0811	18.9189
Stone fruit	1	11	3	12	20	0	47	42.5532	57.4468
Exotic fruit	1	2	1	2	0	13	19	68.4211	31.5789
TOTALS	39	97	147	45	27	18	373		
CA%	87.1795	73.1959	78.2313	66.6667	74.0741	72.2222			
EC%	12.8205	26.8041	21.7687	33.3333	25.9259	27.7778			
Overall Accuracy:	75.8713								
Overall Kappa:	0.683693								

Table B-4 Confusion matrix for classification results obtained with the MEDOID image compositing approach (Experiment 4).

SVM

Class	Citrus fruit	Grapes	Planted pastures	Pome fruit	Stone fruit	Exotic fruit	TOTALS	PA%	EO%
Citrus fruit	39	1	2	0	2	2	46	84.7826	15.2174
Grapes	1	65	22	3	4	5	100	65	35
Planted pastures	2	9	113	0	0	0	124	91.129	8.87097
Pome fruit	2	1	0	29	4	1	37	78.3784	21.6216
Stone fruit	0	7	5	5	29	1	47	61.7021	38.2979
Exotic fruit	0	3	0	1	2	13	19	68.4211	31.5789
TOTALS	44	86	142	38	41	22	373		
CA%	88.6364	75.5814	79.5775	76.3158	70.7317	59.0909			
EC%	11.3636	24.4186	20.4225	23.6842	29.2683	40.9091			
Overall Accuracy:	77.2118								

Overall Kappa:	0.704095								
K-NN									
Class	Citrus fruit	Grapes	Planted pastures	Pome fruit	Stone fruit	Exotic fruit	TOTALS	PA%	EO%
Citrus fruit	35	1	5	1	2	2	46	76.087	23.913
Grapes	2	56	32	2	4	4	100	56	44
Planted pastures	2	19	100	0	3	0	124	80.6452	19.3548
Pome fruit	2	4	0	23	8	0	37	62.1622	37.8378
Stone fruit	0	7	5	8	23	4	47	48.9362	51.0638
Exotic fruit	1	1	1	1	1	14	19	73.6842	26.3158
TOTALS	42	88	143	35	41	24	373		
CA%	83.3333	63.6364	69.9301	65.7143	56.0976	58.3333			
EC%	16.6667	36.3636	30.0699	34.2857	43.9024	41.6667			
Overall Accuracy:	67.2922								
Overall Kappa:	0.574659								
DT									
Class	Citrus fruit	Grapes	Planted pastures	Pome fruit	Stone fruit	Exotic fruit	TOTALS	PA%	EO%
Citrus fruit	30	1	5	4	2	4	46	65.2174	34.7826
Grapes	4	53	27	4	9	3	100	53	47
Planted pastures	3	23	97	0	1	0	124	78.2258	21.7742
Pome fruit	5	1	0	22	8	1	37	59.4595	40.5405
Stone fruit	9	7	4	11	16	0	47	34.0426	65.9574
Exotic fruit	0	3	1	1	4	10	19	52.6316	47.3684
TOTALS	51	88	134	42	40	18	373		
CA%	58.8235	60.2273	72.3881	52.381	40	55.5556			
EC%	41.1765	39.7727	27.6119	47.619	60	44.4444			
Overall Accuracy:	61.126								
Overall Kappa:	0.497309								
RF									
Class	Citrus fruit	Grapes	Planted pastures	Pome fruit	Stone fruit	Exotic fruit	TOTALS	PA%	EO%
Citrus fruit	34	0	6	3	2	1	46	73.913	26.087

Grapes	1	68	27	0	3	1	100	68	32
Planted pastures	0	4	120	0	0	0	124	96.7742	3.22581
Pome fruit	2	1	0	28	5	1	37	75.6757	24.3243
Stone fruit	5	10	3	9	20	0	47	42.5532	57.4468
Exotic fruit	0	3	1	1	1	13	19	68.4211	31.5789
TOTALS	42	86	157	41	31	16	373		
CA%	80.9524	79.0698	76.4331	68.2927	64.5161	81.25			
EC%	19.0476	20.9302	23.5669	31.7073	35.4839	18.75			
Overall Accuracy:	75.8713								
Overall Kappa:	0.682856								

Table B-5 Confusion matrix for classification results obtained with the MaxNDVI image compositing approach (Experiment 5).

SVM									
Class	Citrus fruit	Grapes	Planted pastures	Pome fruit	Stone fruit	Exotic fruit	TOTALS	PA%	EO%
Citrus fruit	37	1	5	0	1	2	46	80.4348	19.5652
Grapes	1	72	21	2	1	3	100	72	28
Planted pastures	2	9	113	0	0	0	124	91.129	8.87097
Pome fruit	2	0	0	25	7	4	38	65.7895	34.2105
Stone fruit	1	9	6	6	25	0	47	53.1915	46.8085
Exotic fruit	0	2	0	1	1	15	19	78.9474	21.0526
TOTALS	43	93	145	34	35	24	374		
CA%	86.0465	77.4194	77.931	73.5294	71.4286	62.5			
EC%	13.9535	22.5806	22.069	26.4706	28.5714	37.5			
Overall Accuracy:	76.738								
Overall Kappa:	0.696545								
K-NN									
Class	Citrus fruit	Grapes	Planted pastures	Pome fruit	Stone fruit	Exotic fruit	TOTALS	PA%	EO%
Citrus fruit	37	1	4	2	2	0	46	80.4348	19.5652
Grapes	2	57	33	1	7	0	100	57	43
Planted pastures	1	19	102	2	0	0	124	82.2581	17.7419
Pome fruit	3	2	1	23	6	3	38	60.5263	39.4737

Stone fruit	3	8	5	12	17	2	47	36.1702	63.8298
Exotic fruit	0	1	1	2	0	15	19	78.9474	21.0526
TOTALS	46	88	146	42	32	20	374		
CA%	80.4348	64.7727	69.863	54.7619	53.125	75			
EC%	19.5652	35.2273	30.137	45.2381	46.875	25			
Overall Accuracy:	67.1123								
Overall Kappa:	0.57158								

DT

Class	Citrus fruit	Grapes	Planted pastures	Pome fruit	Stone fruit	Exotic fruit	TOTALS	PA%	EO%
Citrus fruit	35	2	4	3	1	1	46	76.087	23.913
Grapes	4	58	20	6	9	3	100	58	42
Planted pastures	2	18	97	4	3	0	124	78.2258	21.7742
Pome fruit	5	1	0	18	8	6	38	47.3684	52.6316
Stone fruit	4	9	4	11	16	3	47	34.0426	65.9574
Exotic fruit	0	0	1	3	3	12	19	63.1579	36.8421
TOTALS	50	88	126	45	40	25	374		
CA%	70	65.9091	76.9841	40	40	48			
EC%	30	34.0909	23.0159	60	60	52			
Overall Accuracy:	63.1016								
Overall Kappa:	0.526873								

RF

Class	Citrus fruit	Grapes	Planted pastures	Pome fruit	Stone fruit	Exotic fruit	TOTALS	PA%	EO%
Citrus fruit	34	2	4	1	4	1	46	73.913	26.087
Grapes	2	73	21	0	2	2	100	73	27
Planted pastures	0	8	116	0	0	0	124	93.5484	6.45161
Pome fruit	2	2	0	33	1	0	38	86.8421	13.1579
Stone fruit	0	12	1	11	23	0	47	48.9362	51.0638
Exotic fruit	0	2	1	1	2	13	19	68.4211	31.5789
TOTALS	38	99	143	46	32	16	374		
CA%	89.4737	73.7374	81.1189	71.7391	71.875	81.25			

EC%	10.5263	26.2626	18.8811	28.2609	28.125	18.75
Overall Accuracy:	78.0749					
Overall Kappa:	0.713222					

Table B-6 Confusion matrix for classification results obtained with the MinRed image compositing approach (Experiment 6).

SVM

Class	Citrus fruit	Grapes	Planted pastures	Pome fruit	Stone fruit	Exotic fruit	TOTALS	PA%	EO%
Citrus fruit	37	1	5	0	3	0	46	80.4348	19.5652
Grapes	2	69	22	1	1	5	100	69	31
Planted pastures	3	5	114	0	2	0	124	91.9355	8.06452
Pome fruit	1	1	0	27	9	0	38	71.0526	28.9474
Stone fruit	1	5	5	7	29	0	47	61.7021	38.2979
Exotic fruit	0	2	0	1	1	15	19	78.9474	21.0526
TOTALS	44	83	146	36	45	20	374		
CA%	84.0909	83.1325	78.0822	75	64.4444	75			
EC%	15.9091	16.8675	21.9178	25	35.5556	25			

Overall Accuracy: 77.8075

Overall Kappa: 0.711465

K-NN

Class	Citrus fruit	Grapes	Planted pastures	Pome fruit	Stone fruit	Exotic fruit	TOTALS	PA%	EO%
Citrus fruit	38	1	4	2	1	0	46	82.6087	17.3913
Grapes	1	54	27	6	9	3	100	54	46
Planted pastures	0	21	99	1	2	1	124	79.8387	20.1613
Pome fruit	3	0	0	26	6	3	38	68.4211	31.5789
Stone fruit	2	3	11	9	21	1	47	44.6809	55.3191
Exotic fruit	0	0	3	1	0	15	19	78.9474	21.0526
TOTALS	44	79	144	45	39	23	374		
CA%	86.3636	68.3544	68.75	57.7778	53.8462	65.2174			
EC%	13.6364	31.6456	31.25	42.2222	46.1538	34.7826			
Overall Accuracy:	67.6471								
Overall Kappa:	0.581431								

DT

Class	Citrus fruit	Grapes	Planted pastures	Pome fruit	Stone fruit	Exotic fruit	TOTALS	PA%	EO%
Citrus fruit	29	5	4	3	3	2	46	63.0435	36.9565
Grapes	5	59	22	3	6	5	100	59	41
Planted pastures	2	16	101	1	2	2	124	81.4516	18.5484
Pome fruit	2	2	0	27	6	1	38	71.0526	28.9474
Stone fruit	5	6	5	12	19	0	47	40.4255	59.5745
Exotic fruit	0	4	2	1	1	11	19	57.8947	42.1053
TOTALS	43	92	134	47	37	21	374		
CA%	67.4419	64.1304	75.3731	57.4468	51.3514	52.381			
EC%	32.5581	35.8696	24.6269	42.5532	48.6486	47.619			
Overall Accuracy:	65.7754								
Overall Kappa:	0.557388								

RF

Class	Citrus fruit	Grapes	Planted pastures	Pome fruit	Stone fruit	Exotic fruit	TOTALS	PA%	EO%
Citrus fruit	35	1	5	1	3	1	46	76.087	23.913
Grapes	1	69	28	0	1	1	100	69	31
Planted pastures	0	10	113	0	1	0	124	91.129	8.87097
Pome fruit	2	2	0	29	5	0	38	76.3158	23.6842
Stone fruit	2	10	5	14	16	0	47	34.0426	65.9574
Exotic fruit	1	1	2	1	2	12	19	63.1579	36.8421
TOTALS	41	93	153	45	28	14	374		
CA%	85.3659	74.1935	73.8562	64.4444	57.1429	85.7143			
EC%	14.6341	25.8065	26.1438	35.5556	42.8571	14.2857			
Overall Accuracy:	73.262								
Overall Kappa:	0.648582								